THERAPEUTIC EFFICACY OF INTRATHECAL ADMINISTRATION OF AAVRH10-MHEXA VECTOR IN A MOUSE MODEL OF TAY-SACHS DISEASE

A Thesis Submitted to
the Graduate School of
İzmir Institute of Technology
in Partial Fulfillment of the Requirements for the Degree of

DOCTOR OF PHILOSOPHY

in Molecular Biology and Genetics

by
Melike CAN ÖZGÜR

May 2025
İZMİR

We approve the thesis of **Melike CAN ÖZGÜR**

Examining Committee Members:

Prof. Dr. Volkan SEYRANTEPE
Department of Molecular Biology and Genetics, Izmir Institute of Technology

Prof. Dr. Güneş ÖZHAN
Department of Molecular Biology and Genetics, Izmir Institute of Technology

Prof. Dr. Engin ÖZÇİVİCİ
Department of Bioengineering, Izmir Institute of Technology

Assoc. Prof. Dr. Kemal Uğur TÜFEKÇİ
Vocational School of Health Services, Izmir Democracy University

Asst. Prof. Yavuz OKTAY
Department of Basic Medical Sciences, Dokuz Eylül University

15 May 2025

Prof. Dr. Volkan SEYRANTEPE
Supervisor, Department of Molecular Biology and Genetics
Izmir Institute of Technology

Prof. Dr. Güneş ÖZHAN
Head of Department of Molecular Biology and Genetics

Prof. Dr. Mehtap EANES
Dean of Graduate School

ACKNOWLEDGMENTS

First of all, I would like to express my deepest regards and gratitude to my supervisor Prof. Dr. Volkan SEYRANTEPE for his guidance, motivation, support, extensive knowledge in my research and thesis studies.

I would like to express special thanks to Prof. Dr. Güneş ÖZHAN, Prof. Dr. Engin ÖZÇİVİCİ, Assoc. Prof. Dr. Kemal Uğur TÜFEKÇİ, and Asst. Prof. Yavuz OKTAY for being my thesis committee members as well as their suggestions and contributions.

I would like to thank The Scientific and Technological Research Council of Turkey (TUBITAK) - Bosphorus (120N552) for financial support of the project and for providing me the scholarship.

I am also grateful to my co-workers Selin ATEŞ, Orhan Kerim İNCİ, Selman YANBUL, and TUFAN UTKU ÇALIŞKAN for their support and kindness during my thesis work.

I am grateful to my supportive friends, Hatice Hande BASIRLI, Tuğçe ŞENGÜL TURAN, Deniz AK, Ebru ADA, and Beyza KAYA for their help, assistance, support, and kindness during my research and thesis work. I especially thank Seçil AKYILDIZ DEMİR for her assistance and help during my graduate studies. I am also thankful to undergraduate members of the Seyrantepe Laboratory for their sincere help and kindness.

At last but not least, I thank to my family, my father Adnan CAN, my mother Nilgün CAN, and my brother Cemal Anıl CAN for their sincere love, motivation, belief and support throughout all my life and education. I am also grateful to my husband Güven ÖZGÜR for his love, understanding, motivation and endless support.

ABSTRACT

THERAPEUTIC EFFICACY OF INTRATHECAL ADMINISTRATION OF AAVRH10-MHEXA VECTOR IN A MOUSE MODEL OF TAY-SACHS DISEASE

Tay-Sachs disease, a lysosomal storage disorder, is caused by mutations in *HEXA* gene, which encodes α-subunit of β-hexosaminidase A, an enzyme responsible for degrading GM2 ganglioside. Recently, Tay-Sachs disease mouse model (DKO mice) with combined *Hexa* and *Neu3* gene deficiencies exhibited severe neuropathological symptoms and neuroinflammation, surviving up to 20 weeks. Although therapeutic strategies have been evaluated for several lysosomal storage disorders, effective treatments for Tay-Sachs disease have not yet been developed. Here, we aimed to investigate therapeutic efficacy of intrathecal administration of AAVrh10-mHexa (AAV), expressing mouse Hexa, in DKO mice. Additionally, we assessed combined treatment of AAV-based gene therapy and istradefylline treatment, anti-inflammatory agent, for its potential to alleviate neuroinflammation in DKO mice. Molecular biological, immunohistochemical, and behavioral analyses were conducted. We demonstrated that life span of DKO mice extended up to 30 weeks following administration of AAV alone and in combination with istradefylline. Molecular biological analyses revealed elevated mouse Hexa activity and reduced expression levels of lysosomal marker, and pro-inflammatory cytokines, Ccl2 and Ccl3, in cortex, cerebellum, and organs including kidney, liver and spleen of DKO mice administered with AAV alone and in combination with istradefylline. Immunohistochemistry data showed clearance of GM2 accumulation, reduced lysosome numbers, lower levels of active astrocytes, and improvements in neurons and oligodendrocytes in brain of DKO mice administered with AAV and AAV combined with istradefylline. Motor activity also improved in these mice. Our data suggest that AAVrh10-based intrathecal administration, alone or combined with istradefylline, is a promising therapeutic approach for treating Tay-Sachs disease.

ÖZET

TAY-SACHS HASTALIĞI FARE MODELİNDE AAVRH10-MHEXA VEKTÖRÜNÜN INTRATEKAL UYGULAMASININ TERAPÖTİK ETKİSİ

Tay-Sachs hastalığı, bir lizozomal depolama hastalığıdır ve *HEXA* genindeki mutasyonlar sonucu oluşmaktadrr. *HEXA* geni, GM2 gangliosidini parçalamaktan sorumlu β-hekzosaminidaz A enziminin α-alt birimini kodlar. Son zamanlarda, *Hexa* ve *Neu3* genlerinin birleşik eksikliklerine sahip Tay-Sachs hastalığı fare modeli (DKO fareleri), şiddetli nöropatolojik semptomlar ve nöroinflamasyon sergileyerek 20 haftaya kadar hayatta kalmıştır. Birçok lizozomal depolama hastalığı için tedavi stratejileri değerlendirilmiş olsa da, Tay-Sachs hastalığı için etkin tedaviler henüz geliştirilememiştir. Bu çalışmada, AAVrh10-mHexa (AAV) vektörünün intratekal uygulanmasının DKO farelerinde terapötik etkinliğini araştırmayı amaçladık. Ayrıca, AAV ilişkili gen tedavisi ile bir anti-inflamatuar ajanı olan istradefylline tedavisinin, DKO farelerinde nöroinflamasyonu hafifletme potansiyelini değerlendirdik. Moleküler biyolojik, immünohistokimyasal ve davranışsal analizler yapıldı. AAV tek başına ve istradefylline ile kombinasyon halinde uygulandıktan sonra DKO farelerinin yaşam süresinin 30 haftaya kadar uzadığını gösterdik. Moleküler biyolojik analizler, AAV tedavisi uygulanan ve istradefylline ile kombinasyon halinde tedavi edilen DKO farelerinin korteks, beyincik ve böbrek, karaciğer ve dalak gibi organlarında Hexa aktivitesinin arttığını ve lizozomal markerlar ile pro-inflamatuar sitokinler olan Ccl2 ve Ccl3 seviyelerinin azaldığını ortaya koydu. İmmünohistokimyasal veriler, AAV ve AAV-istradefylline kombinasyonu ile tedavi edilen farelerin beyinlerinde GM2 birikintisinin temizlendiğini, lizozom sayılarının azaldığını, aktif astrosit düzeylerinin düştüğünü ve nöronlar ile oligodendrositlerde iyileşmeler olduğunu gösterdi. Ayrıca, bu farelerde motor aktivitesi de iyileşti. Bu sonuçlar, AAVrh10 ilişkili intratekal uygulamanın, tek başına veya istradefylline ile kombinasyon halinde, Tay-Sachs hastalığını tedavi etmek için umut verici bir terapötik yaklaşım olduğunu göstermektedir.

Dedicated to my precious family…

TABLE OF CONTENTS

LIST OF FIGURES

Figure **Page**

LIST OF TABLES

CHAPTER 1

INTRODUCTION

1.1. Gangliosides

Sphingolipids are glycolipids including the sphingosine backbone and an unsaturated hydrophobic part (Carter and Haines, 1947). Sphingolipids have functional roles in the cell membrane and cellular processes such as cell growth, apoptosis, cellular communication, signaling pathways, and immune responses (Borodzicz et al., 2015).

Glycosphingolipids are a class of sphingolipids that include sugar attachment to the ceramide (Malhotra, 2012). Glycosphingolipids are essential components of the cell membrane, particulary in neurons, where they contribute to the cell membrane stability, neural development, cellular communication, cell recognition, and signal transduction within cells (Coet et al., 1998). Ganglio-, lacto/neolacto-, globo-, and asialo- series are classes of glycosphingolipids based on their carbohydrate moiety (Coet et al., 1998).

Gangliosides are a subclass of glycosphingolipids. Gangliosides, which are acidic or sialylated glycosphingolipids, include a sialic acid residue known as N-acetylneuraminic acid (NANA) (Olsen and Færgeman, 2017). Approximately, 20% of lipids are gangliosides and these are amphipathic molecules, consisting of a hydrophobic tail and a hydrophilic, carbohydrate, head group (Sandhoff and Harzer, 2013). Gangliosides are structural components of the cell membrane and interact with other components of the cell membrane such as cholesterol and glycosphingolipids (K. Sandhoff and Harzer, 2013). In addition to cell membranes, the central nervous system is enriched with gangliosides, which are localized in the membranes of neurons and glial cells (Yao et al., 2014). Like glycosphingolipids, gangliosides play a role in the signal transduction, cellular interactions, neuron development, cell adhesion, and recognition (Yao et al., 2014).

Endoplasmic Reticulum (ER) is the starting region of ganglioside biosynthesis, and further processing with the addition of carbohydrate residues occurs in the Golgi apparatus (Inci et al., 2024). First, ceramide is synthesized de novo in ER, then the produced ceramide is transferred to Golgi apparatus to produce complex gangliosides.

Glucosylceramide (GluCer) is produced first from ceramide, followed by Lactosylceramide (LacCer), which is synthesized by the addition of galactose to GluCer. LacCer is an intermediate for producing 0-, a-, b-, and c- series gangliosides (Figure 1.1). These different series of gangliosides are categorized based on the number of sialic acid residues. 0-series gangliosides do not contain any sialic acid, while one sialic acid is located on a- series gangliosides, two sialic acid in b- series, and three sialic acid residues in c-series gangliosides (Inci et al., 2024). GM3 synthase is an enzyme to synthase GM3 ganglioside which is precursor for the complex a- series gangliosides consisting of GM2, GM1, GD1a, GT1a. Moreover, GD3 synthase is another enzyme to produce GD3 ganglioside from the GM3 ganglioside, and it is known as a precursor for the b- series gangliosides such as GD2, GD1b, GT1b, GQ1b. The addition of sialic acid to GD3 ganglioside produces GT3 ganglioside, which is the precursor to produce c- series gangliosides (GT2, GT1c, GQ1c, GP1c), and this process is performed by GT3S enzyme (Kolter, 2012). B4GALNT1 (Galgt) enzyme is responsible for the production of complex 0- a-, b-, and c- series gangliosides from the simple LacCer, GM3, GD3, and GT3 ganglisoides in sequence (Inci et al., 2024)

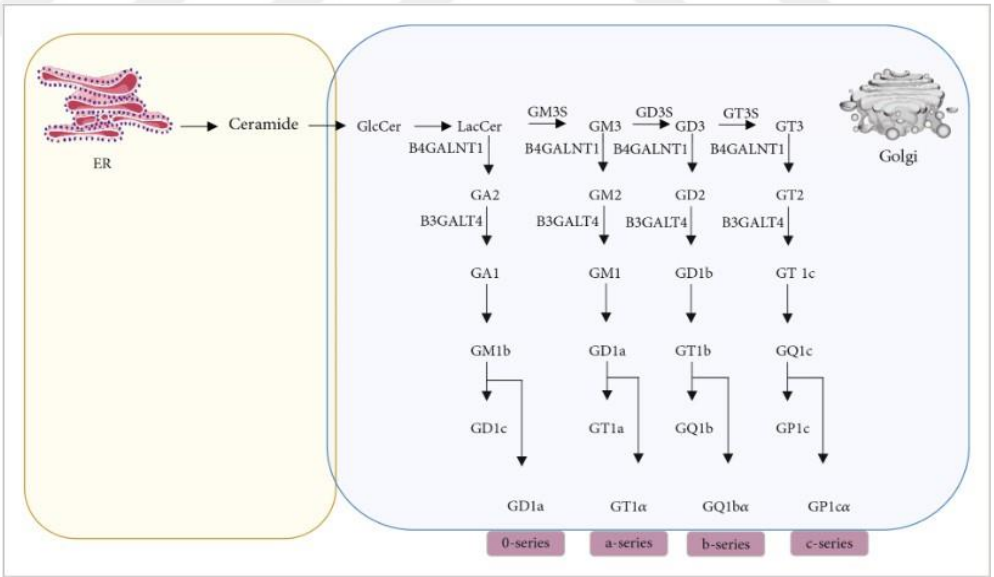

Figure 1.1. The ganglioside biosynthesis pathway. Gangliosides are demonstrated based on Svennerholm's nomenclature system (by courtesy of Inci et al., 2024).

The degradation of gangliosides takes place in lysosomes; therefore the produced complex gangliosides are transferred to lysosomes (Kolter, 2012).Lysosomes are acidic

organelles containing acid hydrolyses and enzymes for the degradation of metabolites, substances, and molecules which are directed to lysosomes. Gangliosides are also degraded by lysosomal enzymes. Lysosomal exo-hydrolases and proteins remove the sialic acids and carbohydrate parts of gangliosides (Kolter, 2012). Sialidases including Neu1, Neu2, Neu3, and Neu4 mainly catalyze and remove the sialic acid residues on glycoconjugates and gangliosides (Miyagi and Yamaguchi, 2012). Other enzymes, including β-Galactosidase (β-Gal) for galactose residues, β-Glucosidase (GCase) for glucose residues, and β-Hexosaminidase a and b (Hexa, Hexb) for N-acetylgalactoseamine, are available in lysosomes for the degradation of gangliosides (Xu et al., 2010).

Specific enzymes are present for the synthesis and degradation of gangliosides. In general, enzymes responsible to produce gangliosides are mainly found as membrane–bound, whereas catabolism of gangliosides is maintained by the soluble lysosomal enzymes. Activator proteins are also soluble and assist in the degradation of gangliosides (Xu et al., 2010)

1.2. Lysosomal Storage Disorders

Lysosomal storage disorders (LSDs) are inherited metabolic diseases caused by mutations or defects in single genes (Platt et al., 2018). Approximately 70% of lysosomal storage disorders are due to defects in lysosomal enzymes, while deficiencies in the enzyme activator protein or enzyme-associated proteins are responsible for several groups of lysosomal storage disorders (Platt et al., 2018). Mutation in genes or specific regions in chromosomes impairs the production of functional enzymes. Moreover, gene mutations can lead to the production of non-functional activator proteins, which are essential for enzyme functionality (Platt et al., 2018). Most lysosomal storage disorders are associated with mutations in genes encoding lysosomal enzymes. Lysosomes contain many hydrolases, each encoded by distinct genes. Nonsense or missense mutations can impair enzyme function, and these mutations may be inherited within families, making genetic testing crucial for the diagnosis of disease before birth (Ysselstein et al., 2019). On the other hand, environmental reasons or epigenetic factors have an impact on disease pathology (Ysselstein et al., 2019).

The mode of inheritance of lysosomal storage disorders is generally autosomal recessive. However, X-linked inheritance is observed in several lysosomal storage disorders, including Fabry disease, Hunter disease, and Danon disease. The classification of LSDs into sphingolipidosis, oligosaccharidosis, mucopolysaccharidosis, sialic acid disorders, mucolipidosis, neuronal ceroid lipofuscinosis, miscellaneous, is based on the accumulating metabolites. In the group of sphingolipidosis, complex phospholipids including the sphingosine backbone accumulate due to mutant enzyme. GM2 gangliosidoses (Tay-Sachs disease, Sandhoff disease, and GM2 activator deficiency), Niemann Pick disease, Gaucher disease, GM1 gangliosidosis, Fabry disease, Krabbe disease and Metachromatic leukodystrophy are examples of sphingolipidosis lysosomal storage disorders. In oligosaccharidosis, the accumulation of glycoproteins is observed in alpha mannosidosis, fucosidosis, and Schindler disease (A. Sun, 2018). On the other hand, mucopolysaccharides accumulate in mucopolysaccharidosis including Hurler syndrome, Hunter syndrome, and San Filippo syndrome. Galactosialidosis and infantile sialic acid storage disease are related to the accumulation of sialic acid in the group of sialic acid disorders (A. Sun, 2018).

The progressive accumulation of metabolites and non-metabolized substrates determines the disease severity. The accumulation and storage of metabolites affect multiple organs, including nervous system, reticuloendothelial system, muscles, eye, and etc. (Boustany, 2013). The central nervous system is the most affected region in lysosomal storage disorders. The symptoms seen in patients can be heterogeneous, and the symptoms can be seen early after birth, or during childhood or adulthood (Stirnemann et al., 2017). The symptoms in infants are more devastating than those in adulthood. Moreover, the presence of residual enzyme activity in patients delays the onset of symptoms.

Several genetic techniques are used to diagnose lysosomal storage disorders, such as restriction fragment length polymorphism by polymerase chain reaction and amplification refractory mutation system to detect missense, nonsense insertion, and deletions in genes (Mokhtariye et al., 2019). DNA sequencing, next-generation sequencing, and multiplex-PCR are other methods to identify mutations in genes. (Filocamo and Morrone, 2011). Furthermore, the accumulation of substrates on urine, and enzyme activity assays are also used in the diagnosis of several lysosomal storage disorders (Cesani et al., 2016).

1.3. GM2 Gangliosidoses

Lysosomal storage disorders are categorized based on the accumulating substances. GM2 gangliosidoses, a group of lysosomal storage disorders, are characterized by the accumulation of GM2 ganglioside due to mutations and deficiencies in genes such as *HEXA* (15^{th} chromosome), *HEXB* (5^{th} chromosome), and *GM2AP* (5^{th} chromosome). GM2 gangliosidoses include three well-known diseases: Tay-Sachs disease, Sandhoff disease, and GM2AP deficiency. The deficiency of the HEXA gene results in Tay-Sachs disease, while a deficiency in the HEXB gene leads to Sandhoff disease. Additionally, mutations in GM2AP (GM2 activator protein) are associated with GM2AP deficiency, another lysosomal storage disorder (Yamanaka et al., 1994; Sango et al., 1995).

β-Hexosaminidase A (HEXA) enzyme is a heterodimer consisting of α- and β-subunits, while β-Hexosaminidase A (HEXB) enzyme is a homodimer composed of β-subunits (Figure 1.2). The HEXA enzyme forms an enzyme complex with GM2AP to degrade GM2 and GA2 gangliosides with the removal of N-acetylgalactosamine (K. Sandhoff and Harzer, 2013). Furthermore, Hexosaminidase S (HEXS) is a homodimer composed of two α- subunits. The *HEXA* gene is responsible for the encoding of α-subunit of β-hexosaminidase A and Hexosaminidase S enzymes, while the HEXB gene encodes the β-subunits of β-hexosaminidase A and β-hexosaminidase B enzymes (Yamanaka et al., 1994; Sango et al., 1995).

All three GM2 gangliosidoses, Tay-Sachs disease, Sandhoff disease, and *GM2AP* deficiency, present similar symptoms in patients due to GM2 ganglioside accumulation (Solovyeva et al., 2018). Tay-Sachs disease is caused by *HEXA* gene deficiency, leading to non-functional HEXA enzymes because of the absence of the α-subunit of β-hexosaminidase A enzyme. HEXS enzyme is also deficient in Tay-Sachs patients (Lawson and Martin, 2016). *HEXB* gene mutations result in Sandhoff disease, with both HEXA and HEXB enzyme activities being deficient in affected individuals (K. Sandhoff and Harzer, 2013).

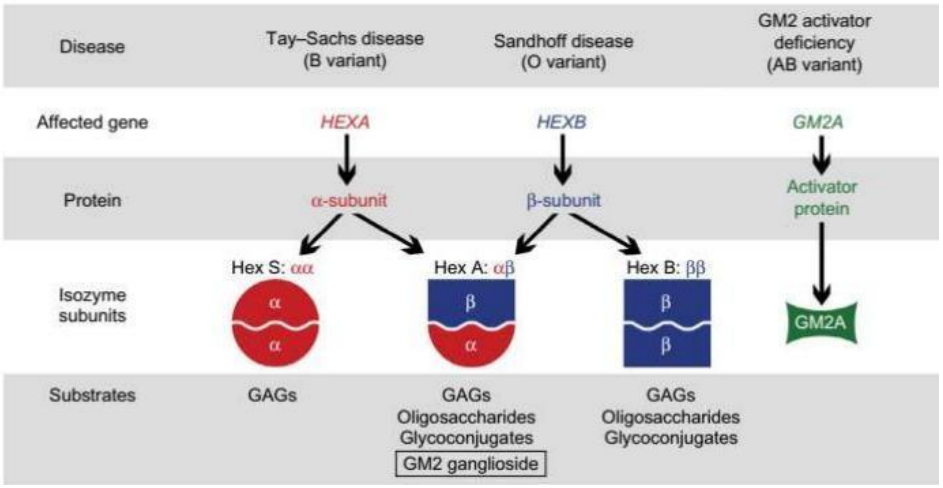

Figure 1.2. Schematic illustration of Hex isozymes in GM2 gangliosidoses diseases (by courtesy of Lawson and Martin, 2016).

GM2 ganglioside is an a- series ganglioside, produced from GM3 ganglioside by the B4GALNT1 enzyme. GM2 ganglioside is an intermediate to produce complex a-series including GM1, GD1a, GD1b, and GT1b. These complex gangliosides are primarily localized in the central nervous system and the cell membranes of neurons (K Sandhoff and Kolter, 1998).

In cases of gene deficiencies affecting ganglioside synthesis and degradation, symptoms such as neurodegeneration, impairments in neural development, axonal problems, demyelination, and behavioral abnormalities are commonly observed. GM2 gangliosides have effective roles in neuron function and development such as differentiation and growth of neurons. Additionally, it contributes to synaptogenesis, neurotransmission, cell proliferation, cell-to-cell communication, and synaptic transmission (Palmano et al., 2015). The critical role of GM2 ganglioside in the brain explains why the central nervous system (CNS) is the most affected region in patients with GM2 gangliosidoses (Konrad Sandhoff, 2016).

1.3.1. Tay-Sachs Disease

Tay-Sach disease (TSD) is a GM2 gangliosidosis, categorized as a lysosomal storage disorder. It follows an autosomal-recessive inheritance pattern and is driven by the mutations in the *HEXA* gene (Yamanaka et al., 1994).The HEXA gene encodes the α-subunit of β-hexosaminidase A (HEXA) enzyme, and its deficiency leads to impairments in the functionality of this enzyme. As a result, GM2 ganglioside cannot be degraded into GM3 ganglioside because of the impaired HEXA enzyme, leading to the progressive accumulation of GM2 ganglioside in Tay-Sachs disease patients.

Tay-Sachs disease occurs in approximately 1 in 100,000 live births, and all cases are associated with mutations in the *HEXA* gene, such as deletions, mutations in the splicing process, missense, and nonsense mutations. Up to the present, over 130 distinct mutations have been identified in the *HEXA* gene, all of which lead to GM2 ganglioside accumulation. These mutations affect various aspects of the HEXA enzyme, including transcription, translation, dimerization and folding, which are critical for the normal function of HEXA enzyme.

GM2 ganglioside accumulates progressively in Tay-Sachs disease patients, but the severity of this accumulation is affected by the residual activity of HEXA enzyme. The presence of 10-15% HEXA enzyme activity is sufficient to prevent severe GM2 ganglioside accumulation (Solovyeva et al., 2018) GM2 ganglioside is localized in the membranous cytoplasmic bodies known as MCBs, which appear as concentric ring-like structures. However, in Tay-Sachs patients, impairments in the cellular structures are evident, with balloon-shaped membranous cytoplasmic bodies (MCBs) observed, causing structural distortion (Yamanaka et al., 1994).

Three distinct clinical forms of Tay-Sachs disease are present depending on the age of onset and the severity of symptoms (Patterson, 2013). In the infantile form of Tay-Sachs disease, the symptoms typically begin to appear within the first few months of life, and the diagnosis is made by around 6 months of age. In the infantile form, HEXA enzyme activity is less than 0.5%, which results in severe neurological impairments, including mental retardation and muscle weakness, and motor function difficulties (K. Sandhoff and Christomanou, 1979). Additional neurodegenerative symptoms include abnormal eye movements, spasms, impairments in sitting, defects in holding the head steady, hypotension, and hypomyelination (Jarnes Utz et al., 2017). Children with the infantile

form of Tay-Sachs disease have a life expectancy no longer than 4 years (Bley et al., 2011). Juvenile form of Tay-Sachs disease is less severe than infantile form, with symptoms typically appearing between the ages of 2 – 10 years. The life span of children with juvenile form is around 15 years. Ataxia, hypotension, muscle spasm, and dysarthria are common symptoms seen in children suffering from the juvenile form of Tay-Sachs disease (Nestrasil et al., 2018). Later-onset form of Tay-Sachs disease is less severe than other, infantile and juvenile forms of Tay-Sachs disease, due to the presence of residual HEXA enzyme activity, around 5-20%. The symptoms are observed in early adulthood and sometimes appear between the ages of 20 and 30 years (K. Sandhoff and Christomanou, 1979). The residual enzyme activity prevents severe neurodegeneration, so delaying the progression of cerebral and motor impairments.

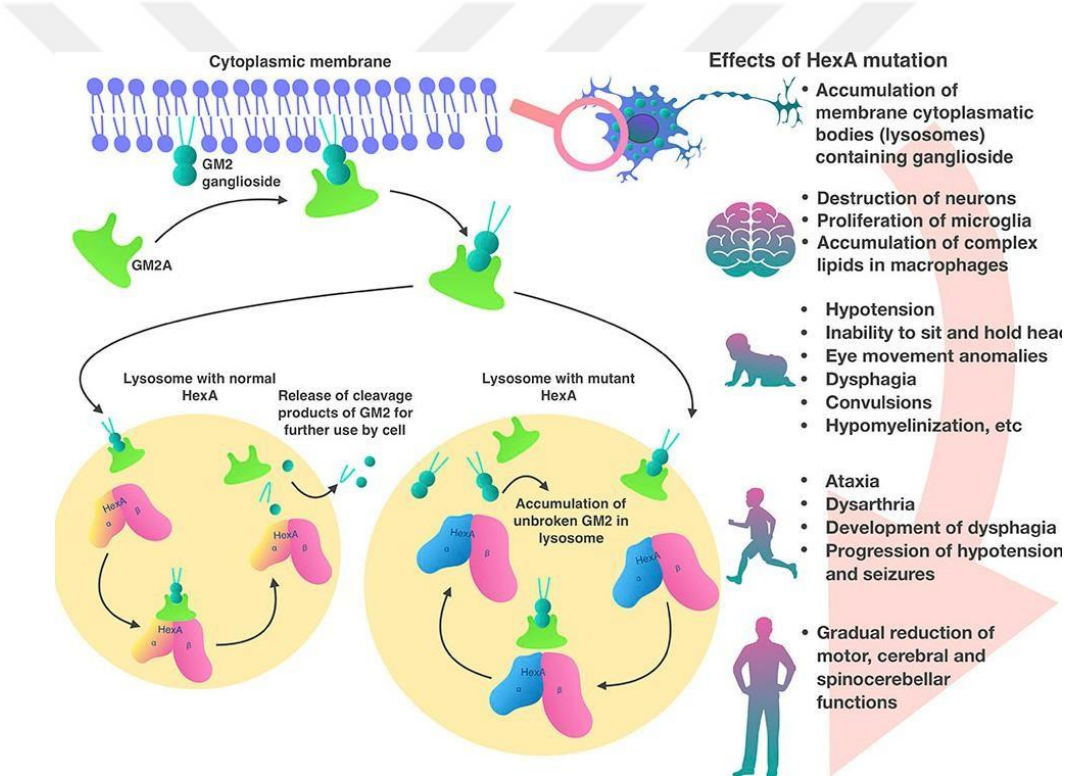

Figure 1.3. Tay-Sach disease pathophysiology (by courtesy of Solovyeva et al., 2018).

1.3.2. Tay-Sachs Disease Mouse Model

The knock-out of *Hexa* gene in mice (*Hexa-/-*) was the first mouse model to create a mouse model of Tay-Sachs disease. As expected, *Hexa-/-* mice showed no Hexa enzyme activity. However, there was no significant GM2 ganglioside accumulation, and membranous cytoplasmic body formation was not observed in the brain of *Hexa-/-* mice. Surprisingly, *Hexa-/-* mice lived without any severe symptoms until approximately one year of age (Taniike et al., 1995). Further studies also demonstrated that *Hexa-/-* mice did not exhibit neurological symptoms and dysfunction (Sango et al., 1995). These findings indicated the presence of differences between human and mouse ganglioside biosynthesis and degradation pathways. The limited GM2 ganglioside accumulation in *Hexa-/-* mice was attributed to the role of sialidases, which cleave the sialic acid residue from GM2 ganglioside, allowing further degradation by HexB activity in these mice (Seyrantepe et al., 2018).

Although *Hexa-/-* mice did not mimic the symptoms observed in Tay-Sachs disease patients, *Hexb-/-* mice showed abnormalities including central nervous system degeneration, muscle weakness, ataxia, and spasticity seen in patients with Sandhoff disease. As a result, *Hexb-/-* mice are used as a valuable model for studying Sandhoff disease (Phaneuf et al., 1996).

To investigate the potential role of Neu3 mammalian sialidase in mouse ganglioside metabolism, a mouse model with the combined deficiency of *Hexa* and *Neu3* genes was created. In this *Hexa-/-Neu3-/-* double knock-out mice model, progressively severe GM2 ganglioside accumulation, high levels of membranous cytoplasmic bodies, bone abnormalities, neuronal death, and neurological abnormalities such as slow movement, ataxia, and tremor were observed, followed by sudden death at 4.5 months (Seyrantepe et al., 2018). These results revealed the existence of a metabolic bypass mechanism in *Hexa-/-* mice, allowing the degradation of GM2 ganglioside to GA2 ganglioside by removing sialic acid residues and converting GA2 into LacCer via *HEXB* activity (Figure 1.4). In recent studies, the altered lipid metabolism (Can et al., 2022), including changes in phosphatidylethanolamine (PE), phosphatidylinositol (PI), phosphatidylcholine (PC), and sphingomyelin (SM), and impaired autophagic flux (Sengul et al., 2023) were indicated in the brain of *Hexa-/-Neu3-/-* mice. Moreover, the modulation of autophagic flux in cells of Tay-Sachs disease including neuroglia of

neonatal *Hexa-/-Neu3-/-* mice, neuroglia and fibroblasts of 5-month-old *Hexa-/-Neu3-/-* mice, and neuroglia of Tay-Sachs disease patients, was shown with autophagy inducer, lithium treatment (Basirli et al., 2024).

The *Hexa-/-Neu3-/-* mice mimic the symptoms of patients with early-onset Tay-Sachs disease, making them a valuable model for developing therapies (Seyrantepe et al., 2018).

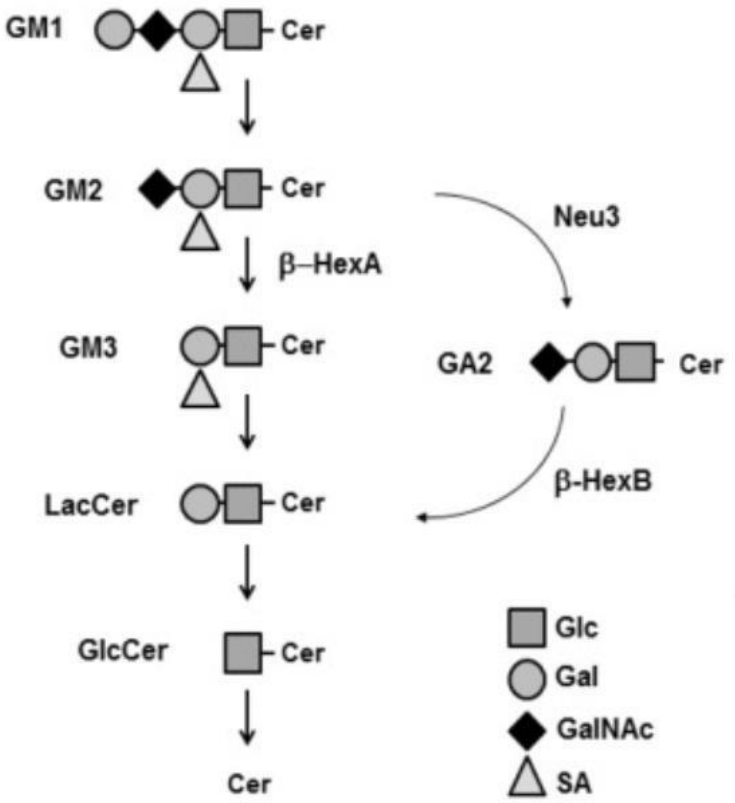

Figure 1.4. Schematic illustration of the degradation pathway of gangliosides. *NEU3* gene has a role in the metabolic bypass in *Hexa-/-* mice (by courtesy of Seyrantepe et al., 2018).

1.4. Therapeutic Approaches in Lysosomal Storage Disorders

There are different therapeutic strategies for lysosomal storage disorders such as enzyme replacement therapy, substrate reduction therapy, pharmacological chaperone therapy, hematopoietic stem cell transplantation therapy and gene therapy (Fernández-Pereira et al., 2021).

1.4.1. Enzyme Replacement Therapy

Enzyme replacement therapy (ERT) is a widely used therapeutic strategy for lysosomal storage disorders. Depending on the specific mutation causing the lysosomal storage disorder, the recombinant enzymes are produced and administered to patients. These recombinant enzymes function to compensate for the deficiency of the impaired enzyme (Fernández-Pereira et al., 2021). The recombinant enzyme produced exhibits the same structure and function as their naturally occurring counterparts. Chinese Ovary Hamster (CHO) cells and human fibroblasts are commonly used cell lines for recombinant enzyme production (Tian et al., 2019). In addition, yeasts and vegetable cells are used for recombinant enzyme production due to advantages such as low costs (Chiba and Akeboshi, 2009). Mannose-6-phospohate (M6P) groups are conjugated to recombinant enzymes, enabling recognition by M6P receptors on the cell surface, allowing the enzymes to be taken up by cells and transported to lysosomes to show their activities.

The major challenge in the enzyme replacement therapy is delivering the recombinant enzyme to the central nervous system (CNS), since these enzymes cannot pass through the blood-brain barrier (BBB). Therefore, enzyme replacement therapy is insufficient for treating the central nervous system (CNS) related manifestations of lysosomal storage disorders (Jakóbkiewicz-Banecka et al., 2007). Furthermore, recombinant enzymes are metabolized in tissues, requiring continuous administration of recombinant enzymes for patients (Sorrentino et al., 2013). Intravenous administration is commonly used for enzyme replacement therapy. Some patients may also develop immune responses to the recombinant enzymes, which can reduce therapeutic efficacy.

Despite these limitations, ERT has been successful in slowing the progression of some lysosomal storage disorders, improving the quality of life for patients. Commercially available enzyme therapies exist for some lysosomal storage disorders such as Gaucher disease, Fabry disease, mucopolysaccharidosis I (MPS) I, MPS II, MPS VI, and MPSVII (Fernández-Pereira et al., 2021). Additionally, in Gaucher disease (Connock et al., 2006), Fabry disease (Eng et al., 2001), Pompe disease (Klinge et al., 2005), MPS I and MPS II (J Muenzer et al., 2002) enzyme replacement therapy is approved clinically.

The enzyme replacement therapy for Tay-Sachs disease has some additional challenges due to the presence of two subunits, α and β, of the Hexa enzyme. To produce the Hexa enzyme, both *HEXA* and *HEXB* genes are expressed in Methylotrophic yeast, *Ogataea minuta*, and the enzyme is then purified and modified with mannose-6-phosphate residues for cellular recognition (Tsuji et al., 2011). The recombinant Hexa enzyme has shown therapeutic effects, including motor function, neurological improvements, and extended lifespan in Sandhoff disease mouse model (*Hexb-/-* mice) (Tropak et al., 2016). In other studies, the recombinant Hexb enzyme has been taken up by the fibroblasts derived from Tay-Sachs disease patients, leading to GM2 ganglioside degradation. Additionally, the intracerebroventricular administration of recombinant Hexb has been shown to improve Hex activity and reduce GM2 ganglioside accumulation in the brains of *Hexb-/-* mice, a Sandhoff disease mouse model (Matsuoka et al., 2011).

1.4.2. Substrate Reduction Therapy

Substrate reduction therapy (SRT) is a therapeutic strategy for the treatment of lysosomal storage disorders. The main goal of substrate reduction therapy is to prevent and reduce the accumulation of metabolites caused by deficient or mutant lysosomal enzymes (Fernández-Pereira et al., 2021). In lysosomal storage disorders, excessive accumulation of metabolites and substances occurs due to the inability of lysosomal enzymes to degrade these substances properly. SRT mainly goals to supply the balance between the synthesis and degradation of these accumulating substances, primarily by reducing the synthesis of substrates or enhancing their degradation (Fernández-Pereira et al., 2021).

Small molecules used in substrate reduction therapy can often pass through the blood-brain barrier (BBB), making this therapy for treating central nervous system–related lysosomal storage disorders. Compared to enzyme replacement therapy, non-invasive treatment options including oral administration, are available in substrate reduction therapy. On the other hand, substrate reduction therapy has its limitations, such as incomplete substrate reduction and side effects like diaerrhea and gastrointestinal disturbances (Ha et al., 2017).

The miglustat (N-butyldeoxynojirimycin, NB-DNJ) has been used in a mouse model of Tay-Sachs disease, *Hexa-/-* mice. The main advantage of miglustat is its abitility

to cross the blood-brain barrier, allowing it to act in the central nervous system (CNS). Miglustat is a small molecule that inhibits glucosylceramide synthase, the enzyme responsible for the first step in glycosphingolipid synthesis, thereby preventing GM2 ganglioside production. In *Hexa-/-* mice, the administration of miglustat via their food demonstrated its effectiveness in reducing GM2 ganglioside levels in the central nervous system (CNS) (Platt et al., 1997). In patients with infantile Tay-Sachs disease, miglustat did not fully correct neurological impairments, but it prevented macrocephaly Additionally, the therapeutic efficacy of miglustat has been shown in both Niemann-Pick type C disease (NPC) mouse models and patients (Patterson et al., 2007). Miglustat is also approved for the treatment of symptomatic patients with type I Gaucher disease (Ficicioglu, 2008).

1.4.3. Hematopoietic Stem Cell Transplantation

Hematopoietic cell transplantation (HSCT) is another therapeutic strategy for lysosomal storage disorders (Kato et al., 2016). Hematopoietic stem cells are transplanted from a healthy donor to patients to supply the expression of mutated enzymes. The replacement of the hematopoietic system in patients restores enzyme activity. This method provides continuous enzyme production by donor myeloid cells, and which are taken by enzyme-deficient patients (Tan et al., 2019). There are no limitations for these donor-derived stem cells in crossing the blood-brain barrier. Therefore, they reach the central nervous system and differentiate into macrophages that secrete the deficient enzymes. This secretion leads to improvements in neurocognitive function (Fratantoni et al., 1968). Hematopoietic stem cell transplantation is applied in mucupolysachharidoses (MPS) type I, a lysosomal storage disorder. Patients younger than 2 years of age treated with hematopoietic stem cell transplantation experience alleviation of symptoms, although this method carries risks for central nervous system function (J. Muenzer et al., 2009).

1.4.4. Pharmacological Chaperone Therapy

Pharmacological chaperone therapy (PCT) is used to treat lysosomal storage disorders (LSDs). Pharmacological chaperones are small molecules that act as chaperones, targeting the misfolded or unfolded enzymes to ensure the proper folding of mutant enzymes and maintain the stability of these mutated enzymes. These pharmacological chaperons provide a less invasive treatment option, as these molecules can be administered to patients orally. However, these chaperones are effective only for specific mutations and enzyme defects, therefore this therapy cannot be used to treat all lysosomal storage disorders (Parenti, 2009)

The pharmacological chaperone therapy has been used to treat Gaucher disease (Z. Yu et al., 2007), Fabry disease (Fan et al., 1999), GM1 gangliosidoses (Matsuda et al., 2003), and Pompe disease (Okumiya et al., 2007), GM2 gangliosidoses (Maegawa et al., 2007), mucopolysahharidoses type IIIB (Ficko-Blean et al., 2008). In Fabry disease, 1–deoxy–galactonojirimycin (DGJ) was used as a pharmacological chaperone to facilitate the correct conformation of the mutant enzyme in mouse model of Fabry disease. Oral administration of this chaperone supplies enzyme activity in the visceral organs (Fan et al., 1999). The chaperones 1-deoxynojirimycin (DNJ) and *N*-butyl- deoxynojirimycin (NB-DNJ) were used in patient fibroblasts of Gaucher disease (Z. Yu et al., 2007) and Pompe disease (Okumiya et al., 2007). The oral administration of *N*-octyl-4-epi-β-valienamine (NOEV), a chemical chaperone therapy, in a mouse model of GM1 gangliosidosis, promoted the expression of the mutant enzyme in brain and visceral organs (Matsuda et al., 2003). The pharmacological chaperone pyrimethamine (PYR, 2,4-diamino-5-(4-chlorophenyl)-6-ethylpyrimidine) was administered to patients with late-onset Sandhoff disease and Tay-Sachs disease. Elevated Hexa enzyme activity exhibited the therapeutic efficacy of PYR pharmacological chaperone in treating late-onset GM2 gangliosidosis (Maegawa et al., 2007).

1.4.5. Gene Therapy

Gene therapy is a therapeutic approach for lysosomal storage disorders (LSDs) and genetic diseases. In gene replacement therapy, a functional form of defective gene is administered to patients to improve gene expression and restore the normal function (Maheshri et al., 2006). On the other hand, gene silencing therapy goals to silence the target gene using RNA interference. Viral-mediated transfer provides the long-term expression of target gene, with lentiviral gene therapy and Adeno-Associated Virus (AAV) based gene therapy being commonly used for lysosomal storage disorders (Kido et al., 2023).

1.5. Adeno-Associated Virus (AAV) Based Gene Therapy

Recombinant adeno-associated virus (AAV) vectors are an effective and promising gene transfer route for diseases such as those related to central nervous system. AAV-based gene therapy is used for gene replacement, gene addition, and gene editing (D. Wang et al., 2019).

The wild-type AAV genome has both plus and minus polarity including approximately 4.8 kb size, and consists of single stranded DNA. The ends of AAV contain 145 bp of inverted terminal repeats (ITRs), 125 bases of which are multi-palindromic. This multi-palindromic feature of ITRs leads to a T-shaped hairpin structure. The 3' hydroxyl group in this hairpin structure becomes available, playing a role in the priming of the replication (Issa et al., 2023a). Therefore, the inverted terminal repeats (ITRs) are essential for priming of viral DNA replication, and can be considered as the viral origin of replication as well as the packaging signal. The AAV genome is a single stranded DNA (ssDNA) including two open reading frames (Rep and Cap), flanked by inverted terminal repeats (ITRs). The Rep genes encode replication-related proteins, consisting of Rep 78, Rep 52, Rep 68, and Rep 40, while the cap genes encode the capsid protein that determine the tropism including VP1, VP2, and VP3 (Issa et al., 2023).

The distinct properties of AAV make it an effective candidate for designing viral vectors used in gene therapy to provide new cures, and therapeutic agents for several diseases. The coated virus becomes uncoated when it enters the cell nucleus. This is

advantageous for AAV since it is protected from degradation in the cell cytoplasm by the presence of lysosomal enzymes (Lebkowski et al., 1988). If there is no helper virus, such as adenovirus, is present, AAV in lysogenic cycle integrates into the host genome at AAVS1 on human chromosome 19, a preferred site because of the presence of Rep binding sequence. However, when adenovirus acts as a helper, AAV in lytic cycle does not integrate into chromosome 19 and remains as a circular episome (Wang et al., 2019).

Compared to other viral-mediated gene transfer systems, including lentivirus, lack of integration of AVV into the genome is important to prevent the induction of neighboring genes, such as oncogenes. Additionally, AAV vectors can infect all cell types, including dividing, non-dividing, and quiescent cells, allowing for the delivery of genetic material to a wide range of cell types. Notably, neurons and muscle cells, non-dividing cells, are transduced efficiently with AAVs. Other viral vectors, such as lentivirus and adenovirus, infect a more limited range of cell types. Compared to other viral vectors, AAV vectors provide less immune response and are non-pathogenic. The stable and long-term expression of the gene of interest is also a significant (Bartlett et al., 2000).

On the other hand, the packaging DNA size is a disadvantage for AAV vectors compared to other viral vectors, such as lentivirus and adenovirus. Limitations in the packaging capacity prevent the design of vectors that include larger inserts. To exceed the limitations in the packaging capacity of AAV, multiple vectors are used, including helper plasmid, AAV transfer plasmid, and packaging plasmid. This method, currently used for recombinant AAV production, is known as the 3-plasmid co-transfection method (Figure 1.5). The advantage of this 3-plasmid co-transfection method is that it prevents contamination during recombinant AAV production, and results in pure recombinant AAV. Additionally, the insert size, such as transgene, can be increased by administering cis-acting elements, including Rep and Cap sites, in another plasmid (Wu et al., 2010). The efficiently transduced cell types with the AAV are transformed cell lines (HeLa, HEK293T), leukemia cell, or human colon cancer lines (LIM or HT29). The most commonly used cell line is the HEK293 cells for the recombinant AAV generation because they provide adenovirus helper genes including E1a and E1b55k (Wu et al., 2010).

Single-stranded AAV (ssAAV) and self-complementary AAV (scAAV) vectors are both available. To express recombinant AAV vectors, single-stranded DNA must be

converted to double-stranded DNA via activity of host DNA ploymerease. ssAAV vectors have a 4.8 kb packaging capacity, while scAAV vectors, a mutated form of ssAA, have a 2.4 kb capacity (Nathwani et al., 2006). Although the packaging capacity of scAAV is lower than that of ssAAV, scAAV is faster because scAAV does not need to usage of host DNA polymerase for the synthesis of complementary DNA (Nathwani et al., 2006).

Several changes and modifications to recombinant AAV vectors can be applied by scientists to make them more effective. One of the modifications is capsid modification, which modifies the tropism for several tissue types. There are several serotypes of AAV, with recent studies demonstrating the presence of 12 natural serotypes and over 100 variants (Li and Samulski, 2020). Mutants of these serotypes have also been produced to optimize their use in gene delivery. Serotypes of AAV range from AAV1 to AAV12. Commonly used serotypes for gene therapy in several diseases are AAV1, AAV2, AAV5, AAV6, AAV8, AAV9, and AAVrh10 (rh due to isolation from rhesus monkeys) (Li and Samulski, 2020). The origin of isolation of each AAV serotype shows variation and differences. AAV1, AAV4, AAV7, AAV8, AAV10 and AAV11 were purified from the monkey samples (Parks et al., 1970). AAV2, AAV3 and AAV5 serotypes are human origin because they showed affinity to antibodies of human populations (W. Xiao et al., 2002). The origin of AAV9 and AAV12 was demonstrated to be human. Additionally, it was clarified that the AAV6 serotype is a hybrid, recombinant of AAV1 and AAV2, as its p5 promoter and ITRs are like AAV2, while other regions are identical to AAV1 (W. Xiao et al., 2002)

All serotypes share a common genome structure; however, they differ depending on their capsid proteins. The capsid proteins supply the recognition of cell receptors, so changes in these capsid proteins lead to distinct serotypes. The most used serotype for vector production is AAV2, which targets the brain, kidney, retina, central nervous system (Issa et al., 2023). AAV1 and AAV7 exhibit a tropism for skeletal muscle and central nervous system, while AAV4 and AAV5 show recognition for the central nervous system and eye. Additionally, AAV8 has strong tropism for heart, liver and pancreas, and AAV9 has efficient recognition across various tissues (Issa et al., 2023).

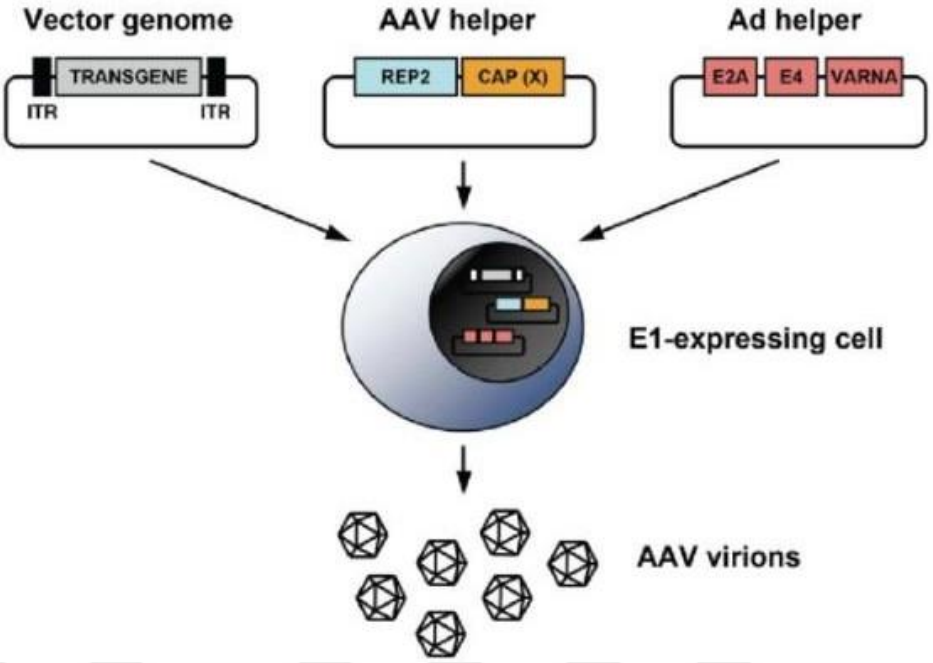

Figure 1.5. The triple transfection in E1- expressing cells, commonly used HEK293T cells to produce AAV virus particles. Vector genome include the gene of interest, flanked by inverted terminal repeats (ITRs) (generally used serotype 2). AAV helper plasmid includes Rep and Cp genes to determine the tropisim of AAV. The third plasmid is AD helper including adenovirus gene for the production of infectious AAV virus particles (by courtesy of Ayuso et al., 2010).

1.5.1. AAV-Based Gene Therapy in Lysosomal Storage Disorders

Adone-Associated virus (AAV) based gene therapy is a commonly used gene therapy strategy to correct the deficient gene in lysosomal storage disorders.

In Fabry disease, a lysosomal storage disorder caused by a mutation in the α-galactosidase A (*GLA*), resulting in the excessive accumulation of Gb3 glycosphingolipids, administration of recombinant (AAV) vector encoding human *GLA* showed improvements in the GLA expression with a decrease Glb3 glycosphingolipid in the plasma of *Gla-/-* mice. Additionally, the long-term stable expression of GLA has been demonstrated in patients following intravenous administration of AAV-encoding *GLA* (Hughes et al., 2020).

The mutations in glucocerebrosidase (*GBA*) cause Gaucher disease, which shows the accumulation of glucosylceramide in lysosomes. Gene therapy has been also explored for this disease. The intracisternal administration of an AAV9 vector expressing GBA

gene was tested in Gaucher disease type II patients, demonstrating both safety and efficacy (Kido et al., 2023).

Mucopolysaccharidoses (MPSs), a lysosomal storage disorder, are characterized by the accumulation of complex sugars (glycosaminoglycans) in tissues such as skin, vascular tissue, and visceral organs, including liver and spleen (Coutinho et al., 2012). Intracerebral injection of an AAV2/5 expressing the human *NAGLU* gene was performed in four children suffering from MPS IIIB. This treatment resulted in improvements in neurological function, increased enzyme activity, and no adverse effects in these children (Tardieu et al., 2017). In a mouse model of MPS IIIB, AAV9 vectors expressing the murine *NAGLU* gene, controlled by a strong promoter (chicken β- actin/cytomegalovirus (CMV), were administered to cisternal magna. In the brains of the mice, restoration of enzyme activity, reduced glycosaminoglycans levels, and alleviated inflammation were observed (Ribera et al., 2015). Furthermore, improvements in lysosome function, reduced neuroinflammation, and extended life span were shown in a mouse model of MPS IIID (*Gns-/-*) after the cisterna magna injection of $5x10^{10}$ vg (vector genome) of AAV9 vector encoding *Gns* (Roca et al., 2017). AAV-based gene therapy has been also determined in a mouse model of MPS IVA. An AAV8 vector encoding human *GALNS*, controlled by a liver-specific promoter, was intravenously administered to 1- month-old MPS IVA mice, restoring GALNS enzyme activity in treated mice (Sawamoto et al., 2020).

The therapeutic efficacy of AAV9/3 encoding the *NPC1* gene (Kurokawa et al., 2021) and AAV2/8 encoding the CTSA gene (Hu et al., 2021) was indicated in mice models of Niemann-Pick C disease (*Npc1-/-*), and Galactosialidosis (*Ctsa-/-*), respectively.

1.5.2. AAV-Based Gene Therapy in Tay-Sachs Disease

Tay-Sachs disease mice model (*Hexa-/-*) has been used to develop therapeutic strategies for patients. First, recombinant adenovirus encoding *HEXA* and *HEXB* genes was intravenously injected to *Hexa-/-* mice. In these mice, the restoration of Hexa enzyme activity was observed in serum and peripheral tissues, especially in liver cells (Guidotti et al., 1999).

In another GM2 gangliosidoses, Sandhoff disease, it has been indicated that the intracranial administration of recombinant AAV 2/1 expressing *HEXA* and *HEXB* supply the increasing level of Hexa activity in the brain along with an extended survival rate (Cachón-González et al., 2014). Intravenous administration of scAAV9.47 encoding *HEXM,* which encodes the α subunit, and stabilize β subunit interface, reduced the GM2 accumulation and extended the life-span (2.5 fold) of neonatal *Hexb-/-* mice (Osmon et al., 2016).

The degradation of GM2 ganglioside in the brain of *Hexa-/-* mice was also demonstrated after the intracranial administration of scAAV9.47 expressing *HEXM,* which encodes α subunit site, and stabilize the β subunit interface (Tropak et al., 2016). Additionally, intravenous administration of scAAV9.47 encoding *HEXM* to neonatal *Hexa-/-* mice resulted in long-term degradation of GM2 ganglioside in the central nervous system (Osmon et al., 2016).

A mix of AAVrh8 encoding *HEXA* and AAVrh8 encoding *HEXB* (total dose of $1x10^{14}$ vg) vectors was administered intrathecally in two infantile TSD patients. Depending on AAV vectors, there were no side effects, and elevated Hexa activity was shown in cerebrospinal fluid in patients. This study represents a unique approach for the treatment of Tay-Sachs disease using AAV-based gene therapy (Flotte et al., 2022). Moreover, the efficacy and safety were also determined in Tay-Sachs patients who were intrathecally administrated AAV9 vector expressing *HEXA* and *HEXB* cDNA (Flotte et al., 2022).

1.5.3. AAVrh10 Gene Therapy in Lysosomal Storage Disorders

There are several stereotypes of AAV, each showing specific tropism for different tissues depending on the type of capsid proteins. While some serotypes show the tropism for the central nervous system and neurons, the novel identified AAVrh10 serotype, isolated from Rhesus Macaques, is neurotropic and specifically transduces the neurons. AAVrh10 not only transduces neurons but also has capacity to transduce astrocytes and oligodendrocytes, which is why it is known as neurotropic. Additionally, like other AAV serotypes such as AAV1, AAV2, and AAV5, AAVrh10 helps to prevent immune responses (Park et al., 2017).

Although several AAV serotypes, including AAV2, AAV5, AAV6, AAV8 and AAV9, AAVrh10 has shown higher transduction efficacy for neurons in the spinal cord and dorsal root of immune-deficient mice after intrathecal injection, compared to these other AAV serotypes (Park et al., 2017). Additionally, AAVrh10 shows efficient tropism for sensory neurons in the bone marrow, sensory nerve fibers, and myelinated sensory neurons (Park et al., 2017). These findings demonstrated that AAVrh10 is an ideal gene delivery vector for central nervous system–affected diseases.

The therapeutic efficacy of AAVrh10 in some lysosomal storage disorders has been shown in previous studies. In mouse models of diseases such as Krabbe disease (Rafi et al., 2012), neuronal ceroid lipofuscinosis (Sondhi et al., 2007), metachromatic leukodystrophy (Piguet et al., 2012), diabetic neuropathy (Homs et al., 2014), and amyotrophic lateral sclerosis (H. Wang et al., 2014), AAVrh10 gene therapy has been tested through intracranial and intrathecal administration. These studies have shown that AAVrh10-associated gene therapy effectively targets neurons and oligodendrocytes, leading to reductions in disease-associated findings in the central nervous system.

Krabbe disease is a lysosomal storage disorder due to GLD deficiency. Intracerebroventricular and intravenous injection of AAVrh10 expressing GALC was performed in the neonatal mouse model of Krabbe disease. Elevated levels of GALC activity were indicated in the brains of treated mice. Moreover, treated mice survive without exhibiting any symptoms and weight loss (Rafi et al., 2012). Late infantile neuronal ceroid lipofuscinosis (LINCL) is another lysosomal storage disorder caused by a deficiency in CLN2 gene. Recently, it has been shown that higher TPP-I activity, clearance of storage granules in the central nervous system, and improvements in neurological symptoms following the striatal injection of AAVrh10 expressing CLN2 gene in *CLN2-/-* mice (Sondhi et al., 2007). In mice model of Metachromatic Leukodystrophy (a lysosomal storage disorder), AAVrh10 encoding human ARSA gene, controlled by cytomegalovirus/β-actin hybrid (CAG/cu) promoter, was injected intrastriatally. This resulted in a restoration of oligodendrocyte density (Piguet et al., 2012). GM1 gangliosidosis, caused by mutations in the GLB1 gene, is a lysosomal storage disorder. AAVrh10 encoding human GLB1 cDNA was injected into intra-cisternal magna of nonhuman primates, leading to widespread distribution of enzyme activity in these primates (Hocquemiller et al., 2022). In a mouse model of lysosomal storage disease mucopolysaccharidosis (MPS) type IIIA, the AAVrh10 vector encoding the lysosomal enzyme sulfatides (SGSH) was injected into the caudate/putamen and thalamus brain

regions at varying dosages (8.6E+08, 4.1E+10, and 9.0E+10 vector genomes [vg]/animal). Dose-dependent improvements were observed, including reductions in accumulated heparan sulfate, lysosomal enlargement, and neuroinflammation (Hocquemiller et al., 2020). These studies highlight the therapeutic effects of AAVrh10 gene therapy in treating central nervous system-related diseases.

1.6. Neuroinflammation

Inflammation is activated as a response of the immune system to protect the body against damage caused by mechanical injury or bacterial or viral invasion (Lyman et al., 2014). The inflammatory response initiated by the central nervous system (CNS), including the brain and spinal cord, is known as neuroinflammation (Ransohoff et al., 2015). Peripheral inflammation, neurodegenerative diseases, autoimmune disorders, aging, injury in brain or spinal cord are common causes of neuroinflammation (Lyman et al., 2014). Trauma or infectious diseases affecting the CNS can result in acute neuroinflammation, and neuroprotection is mediated by the release of cytokines such as Il1 and Il4 (Y. Sun et al., 2022). However, neurodegenerative diseases, severe injury, and aging can cause elevated levels of neuroinflammation, known as chronic neuroinflammation (Bosch and Kielian, 2015). Impairments in the integrity of blood-brain barrier (BBB), infiltration of peripheral immune cells, and the release of high- levels of cytokines and chemokines are observed in case of chronic neuroinflammation (Bosch and Kielian, 2015).

The blood-brain barrier (BBB) is a key cellular component of neuroinflammation, controlling how peripheral inflammation leads to neuroinflammation. This endothelial layer typically does not permit the passage of large and complex molecules, but a prolonged peripheral inflammatory response causes the passage of inflammatory cytokines including TNF and IL, via distinct active transport mechanisms (Gutierrez, Banks et al., 1993). The passage of cytokines across BBB disrupts its tight junctions, increasing permeability. Moreover, several chemokines, consisting of CCL19 and CCL21, play a role in the migration of T-cells throughout the BBB.

Microglia cells, the immune cells and resident of macrophages of the central nervous system (CNS), are another key cellular component of neuroinflammation (Lyman et al., 2014). These cells are mainly located in the brain and spinal cord and are activated

in response to injury or the presence of damaged neurons (Lyman et al., 2014). The release of cytokines during acute inflammation triggers macrophages to transition from their inactive to active, phagocytic state. Once these cells are activated, they migrate to the site of injury and perform phagocytosis to clear damaged cells (B. Liu and Hong, 2003). Prolonged inflammation or chronic neuroinflammation causes extended activity of macrophages. Microglial activation occurs through two different pathways: M1 and M2 activation (B. Liu and Hong, 2003). M1 activation, or classical activation, is related to aggressive inflammation and is driven by interferon (IFN)-ϒ and tumor necrosis factor (TNF). In contrast, alternatively activated from microglia, M2 activation, is stimulated by IL1 and IL-4, and is related to anti-inflammatory responses, wound repair, and axonal regeneration (Liu and Hong, 2003).

Astrocytes are neuroglia cells found in CNS that serve several important functions. Astrocytes regulate microglial cells, maintain blood-brain barrier (BBB) homeostasis, and support the energy metabolism of neurons (Valles et al., 2023). Astrocytes exhibit distinct phenotypes in response to injury or disease, and these reactive astrocytes are categorized as A1 and A2 (Khodadadei et al., 2022). A1 astrocytes are known as neurotoxic and primarily activated by inflammation-related cytokines consisting of TNF-α (Khodadadei et al., 2022). A1 astrocytes release neuroinflammatory factors that damage or kill oligodendrocytes and neurons, leading to neurodegeneration (Ding et al., 2021). A1 astrocytes are activated in several neurodegenerative disorders, including Alzheimer's disease, multiple sclerosis (MS), and Parkinson's disease (Chen et al., 2020). Their activation contributes to chronic inflammation. In contrast, A2 astrocytes, also known as neuroprotective astrocytes, are primarily activated by IL-6 in response to acute injury. Unlike A1 astrocytes, A2 astrocytes protect the neurons and promote their survival. The degree of neuroinflammation and neurodegeneration is influenced by the expression of A1 and A2 astrocytes (Chen et al., 2020).

Cytokines and chemokines are also components of the neuroinflammatory process. Pro-inflammatory cytokines initiate and maintain the inflammation in the CNS, while anti-inflammatory cytokines prevent the inflammation by promoting the healing process. Tumor necrosis factor – alpha (TNFα), interleukin-1 beta (IL-1β), Interleukin-6 (IL-6) and IL-17 are the primary pro-inflammatory cytokines, each playing a crucial role in the maintenance of neuroinflammation. The key mediator of inflammation is TNF-α contributing the blood-brain barrier (BBB) permeability disruption, inducing cell death, and triggering inflammatory responses. It is mainly produced by neurons and neuroglia

cells such as microglia and astrocytes (Clark and Vissel, 2018). IL-1β promotes the production of pro-inflammation-related mediators and induces an inflammatory response in astrocytes (Thornton et al., 2008). IL-17 is involved in activating neuroinflammation, whereas IL-6 exhibits both pro-inflammatory and anti-inflammatory properties (Hammacher et al., 1994). On the other hand, IL-10, IL11, and transforming growth factor – beta (TGF-β) are anti-inflammatory cytokines, and they have action in the suppression of pro-inflammatory cytokines and promoting wound and tissue healing processes (Rauf et al., 2022).

Chemokines are small molecules that regulate the migration of immune cells to damaged regions (Walz et al., 1987). Especially, they are responsible for the recruitment of immune cells, such as macrophages and T-cells, to the injured region of the brain by crossing the blood-brain barrier (BBB). CCL2, CCL3, CCL4, and CXCL10 are chemokines that are crucial in neuroinflammation (Ramesh et al., 2013). CCL2 (monocyte chemoattractant protein-1) facilitates the migration of immune cells across the BBB to the brain. CCL3 (macrophage inflammatory protein-1α) binds to CCR1 and CCR5 receptors, and like CCL2, it recruits macrophages, T-cells, and monocytes (Ramesh et al., 2013). CCL4 (macrophage inflammatory protein-1β) works with CCL3 to activate T-cells, macrophages, and monocytes. CXCL10 binds to CXCR3 receptor and recruits immune cells, including T-cells, natural killer (NK) cells, and monocytes (Ramesh et al., 2013).

1.6.1. Neuroinflammation in Lysosomal Storage Disorders

Lysosomal storage disorders (LSDs) are metabolic diseases caused by gene mutations affecting lysosomal enzymes. The deficiency of these enzymes results in the accumulation of specific substrates in lysosomes, leading to cellular dysfunction and damage (Platt et al., 2018). In all lysosomal storage disorders identified so far, the genes encoding lysosomal enzymes are deficient or dysfunctional, which impairs the synthesis or degradation of metabolites, subsequently leading to the accumulation of molecules in the intra-lysosomal regions (Futerman and van Meer, 2004).

Gaucher disease (GD) is a lysosomal storage disorder caused by the absence of the glucocerebrosidase (GBA) enzyme, resulting in excessive accumulation of glucocerebroside in macrophages (Farfel-Becker et al., 2014). Neuroinflammation has

been shown with the activation of microglia in response to the accumulation of glucocerebrosidase in macrophages and is associated with the release of pro-inflammatory cytokines, including TNF-α, IL-1β, and IL-6 in the mouse model of Gaucher disease and in blood sample of patients suffering from Gaucher disease type II and type III (Wong et al., 2004). The elevated levels of CCL2, CCL3 and CXCL10 chemokines were detected in the brain of Gaucher disease mouse model (Pandey et al., 2017).

Niemann Pick disease type C is a lysosomal storage disorder resulting from mutations in NPC1/NPC2 genes (Vruchte et al., 2004). The problems in lipid transport cause the accumulation of cholesterol and other lipids in the brain and other visceral organs, including the liver and spleen. Microglia activation and neuronal degeneration were observed in a mouse model of Niemann Pick disease type C. The accumulation of pro-inflammatory cytokines, such as TNF-α and IL-1β, was detected in the brain of Niemann Pick disease type C mouse model (Vruchte et al., 2004)

Sialidosis is an autosomal recessive inherited lysosomal storage disorder. Sialidase Neu1 (Neuraminidase 1) is found in lysosomes and acts on sialic acid residues on sialylated glycoconjugates (D'Azzo et al., 2015). *Neu1-/-* mice mimic symptoms observed in severe, Type II, form of sialidosis in patients. In 5-month- old *Neu1-/-* mice, high activation of microglia and macrophages in brain's dendrite gyrus and parenchyma were observed (D'Azzo et al., 2015).

The deficiency of β-Galactosidase encoded by Glb1 gene causes GM1 gangliosidosis, a lysosomal storage disorder, with high accumulation of GM1 ganglioside in the central nervous system. The severe accumulation of GM1 ganglioside leads to excessive secretion of pro-inflammatory cytokines, including TNF-α, IL-1β and IL-6, with high activation of macrophages and microglia in both the mouse model and patients of GM1 gangliosidosis (Jeyakumar, 2003)

GM2 gangliosidoses are a group of lysosomal storage disorders, that lead to severe accumulation of GM2 ganglioside in neurons. Tay-Sachs disease and Sandhoff disease are types of GM2 gangliosidoses. The mutations in HEXB gene, encoding β-hexosaminidase A and B enzymes, cause Sandhoff disease. *Hexb-/-* mice, which mimic symptoms of Sandhoff disease, and Sandhoff patients demonstrated activation of microglia and astrocytes, and significant expression of pro-inflammatory markers such as TNF-α, IL1β, and TGFβ1 in the central nervous system (Wada et al., 2000). In Tay-Sachs disease patients, the elevated level of TNF-α in the cerebrospinal fluid was detected,

although no expression of pro-inflammatory cytokines (TNFα, IL1β, and TGFβ1) was noted in the *Hexa-/-* mouse model (Wada et al., 2000). In the early- onset Tay-Sachs disease mouse model (*Hexa-/-Neu3-/-*), GM2 accumulation results in the activation of macrophages and microglia in the brain, elevated levels of pro-inflammatory chemokines including Ccl2, Ccl3, Ccl4, and Cxcl10, and reduced levels of anti- inflammatory cytokines IL10, IL13, IL11, and IL24 in cortex and cerebellum of the brain (Demir et al., 2020). The release of cytokines and chemokines negatively affects neurons and oligodendrocytes, resulting in the loss of neurons and oligodendrocytes in the brain of *Hexa-/-Neu3-/-* mice. IL11 chemokine, a cytokine responsible for the myelination process, showed reduced expression in the cortex and cerebellum of *Hexa-/-Neu3-/-* mice. Furthermore, peripheral blood mononuclear cell (PBMC) infiltration and astrogliosis were observed in the brain of *Hexa-/-Neu3-/-* mice (Bosch and Kielian, 2015). These findings suggest that modulating neuroinflammation in Tay-Sachs disease can reduce the patient's symptoms.

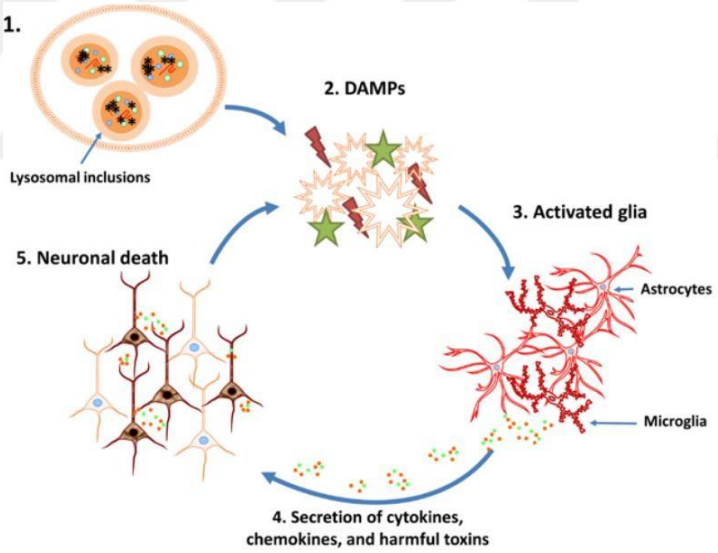

Figure 1.6. The neuroinflammation in Lysosomal Storage Disorders (by courtesy of (Bosch and Kielian, 2015).

1.7. Istradefylline as Anti-Inflammatory Agent

Istradefylline is a chemical approved by U.S. Food and Drug Administration (FDA) for treatment of Parkinson' disease, a neurodegenerative disorder (Hatano et al.,

2023). Istradefylline is an antagonist of the adenosine A_{2A} receptor, and it inhibits the activity of this receptor. This receptor is primarily localized in the striatum and regulates the indirect pathway that affects voluntary movement. In Parkinson's disease patients, there is excessive activation of the indirect pathway (Müller, 2023). Istradefylline inhibits adenosine A_{2A} receptor, leading to the suppression of the hyperactivated indirect pathway. This compound pass through the blood-brain barrier (BBB) (Müller, 2023). The therapeutic efficiency of istradefylline in enhancing motor function has been confirmed in primate and mice models of Parkinson's disease (Uchida et al., 2014). Improvements in life quality and movement were demonstrated in Parkinson' disease patients treated with istradefylline (Iijima et al., 2019).

Anti-inflammatory effect of istradefylline has been shown in mouse model of Sandhoff disease (*Hexb-/-*). The expression of Adenosine A_{2A} receptor was indicated in the cortical astrocytes of 3.5-month-old *Hexb-/-* mice. The expression of A_{2A} receptor in astrocytes of *Hexb-/-* mice was associated with cortical inflammation between 4 to 10 weeks (Ogawa et al., 2018). Moreover, the high activation of A_{2A} receptor induced the expression of neuroinflammation related-markers, including Ccl2, in astrocyte cultures derived from the *Hexb-/-* mice. An A_{2A} receptor agonist also caused an elevated expression of Ccl2, a neuroinflammatory marker. On the other hand, istradefylline was administered to 2.5-month-old *Hexb-/-* mice via intraperitoneal administration for 21 days (Ogawa et al., 2018). Improvements in motor activity, a reduced number of Iba1+ cells (a microglia marker), and a reduced expression of inflammation-related chemokines (Ccl2, Cxcl10) and cytokines (Il1a and Ilib) were observed in cortices of istradefylline administered *Hexb-/-* mice at 4 months of age (Ogawa et al., 2018).

1.8. Aim of the Study

Tay-Sachs disease, a lysosomal storage disorder, is caused by mutations in the *HEXA* gene, which encodes the α-subunit of β-hexosaminidase A, an enzyme responsible for degrading GM2 ganglioside in the brain. Tay-Sachs disease mouse model with a combined deficiency of *Hexa* and *Neu3* (*Hexa-/-Neu3-/-*), exhibited severe neuropathological symptoms and neuroinflammation, surviving up to 20 weeks. While various therapeutic strategies such as enzyme replacement therapy, substrate reduction therapy, hematopoietic stem cell transplantation, pharmacological chaperone therapy, and

gene therapy have been evaluated for several lysosomal storage disorders, effective treatment for Tay-Sachs disease has not yet been developed due to the lack of a suitable mouse model. In this thesis study, we aimed to understand the therapeutic efficacy of the AAVrh10-expressing mouse Hexa gene (AAVrh10-mHexa) in the early-onset Tay-Sachs disease mouse model. Additionally, we evaluated the combined treatment of AAV-based gene therapy and istradefylline, an anti-inflammatory agent, for its potential to enhance GM2 ganglioside degradation and reduce neuroinflammation in this mouse model. To achieve this goal, we conducted molecular biological, immunohistochemical, and behavioral analyses. These analyses enable us to understand whether AAVrh10-based intrathecal administration is a promising therapeutic strategy for the treatment of Tay-Sachs disease.

CHAPTER 2

MATERIALS AND METHODS

2.1 The Production of AAVrh10-mHexa Virus Particles

2.1.1. Vectors

The mammalian expression vector encoding mouse Hexa (pAAV-[Exp]-CMV-mHexa-3xGGGGs-mCherry-oPRE) was designed and purchased from Vector Builder. The CMV (cytomegalovirus) promoter was used as a strong promoter for the expression of the mouse Hexa (mHexa) gene. mCherry was cloned into a mammalian expression vector as a reporter gene, while the ampicillin antibiotic resistance (Amp^R) gene was also used as a marker of antibiotic resistance gene. Hexa and mCherry were fused using a linker to produce a fusion protein (Figure 2.1).

To produce infectious virus particles, pAAV2/rh10 as a packaging vector (Rep/Cap) that shows the tropism for the central nervous system (CNS) and pAdDeltaF6, a helper vector that expresses the genes of adenovirus, were purchased from Addgene. The ampicillin antibiotic resistance (Amp^R) gene was also used as a marker of the antibiotic resistance gene for both vectors.

2.1.2. Confirmation of Vectors

The mammalian expression vector encoding mouse *Hexa*, pAAV2/rh10, and pAdDeltaF6 vectors were in *E.coli* stocks, and each was confirmed after isolation by using restriction enzyme reactions. Firstly, each vector, stored in glycerol stock, was seeded onto LB agar plates (LB with agar, Fisher Scientific) containing ampicillin (Sigma-Aldrich) at 100 mg/ml concentration and incubated overnight at 37 ºC. The next day, single colonies for each vector were observed and seeded into LB broth (Fisher Scientific) consisting of ampicillin (Sigma-Aldrich), followed by incubation overnight in

a shaking incubator at 37 ºC. Then, vectors were isolated using the Alkaline Lysis Purification method.

In the alkaline lysis purification method, 3 ml of grown *E.coli* including vectors was centrifuged at 12000 xg for 30 seconds at 4 ºC, and the supernatants were discarded. 200 µl of resuspension solution, ALS-I, (50 mM Glucose, 25 mMTris-HCI pH 8, 10 mM EDTA pH 8, distilled water) was added to the pellet, and the mixture was vortexed to resuspend the pellets. 200 µl of lysis solution, ALS-II, (0.4N NaOH, 10% SDS, distilled water) was added, followed by the addition of 150 µl of precipitation solution, ALS-III (5M potassium acetate, Glacial acetic acid, distilled water). The samples were vortexed and incubated on ice for 5 minutes, then centrifuged at 12000 xg for 5 minutes at 4 ºC. After the centrifugation, 2 volumes of %100 ethanol were added to the supernatant, vortexed, and incubated for 2 minutes at room temperature. The samples were centrifuged at 12000 xg for 5 minutes at 4 ºC. The pellet part was rinsed using 70% ethanol after the removal of supernatant parts. Samples were centrifuged at 1200 xg for 5 minutes at 4 ºC, followed by air-drying of the pellets containing vectors. The isolated vectors were dissolved in 100 µl of DNase-free distilled water, and the concentration of samples was determined by using a NanoDrop Spectrophotometer (ND-1000).

To confirm the vectors, specific restriction enzymes were used for each vector. For the mammalian expression vector, EcoRI, KpnI, and PstI enzymes were selected (Figure 2.1). BamHI restriction enzyme was used to confirm the packaging vector, pAAV2/rh10, and helper vector, pAdDeltaF6 (Figure 2.2). A reaction mixture was prepared for each restriction enzyme, and each mixture included 1 µl of Biolab NE buffer (10X), 1 µl of specific restriction enzyme; EcoRI, KpnI, PstI, and BamHI (10 units/µl, Biolab NE), and 6000 ng of isolated plasmid, with the total volume being 20 µl, filled with distilled water. The prepared mixtures were incubated at 37 ºC for 2 hours. The expected bands were visualized using agarose gel electrophoresis after the restriction enzyme reactions.

To obtain higher quantities of each vector, the MegaPrep Kit isolation protocol was applied to the vectors. After the confirmation of all vectors, the bacteria inside the LB broth (Fisher Scientific) were transferred to 3ml of Terrific Medium (Fisher Scientific), which contains high growth factors, and incubated overnight in a shaking incubator at 37 ºC. Then, vectors were isolated with MegaPrep Kit (QIAGEN). First, the bacteria were collected by centrifuging at 6000 xg for 15 minutes at 4 ºC. 50 ml of collected bacteria were resuspended and lysed using 50 ml of Buffer P1 and Buffer P2,

respectively. Then, 50 ml prechilled Buffer P3 was added to samples, which were incubated on ice for 30 minutes and then centrifuged at 30000 xg for 45 minutes at 4 ^{o}C. The supernatant containing the DNA of the vector was added to columns that had been equilibrated with 35 ml of Buffer QBT. The columns were washed using 200 ml of Buffer QC, and vectors were eluted using Buffer QF. The eluted vector DNAs were precipitated with 24 ml of isopropanol. After the centrifugation of samples at 15000 xg for 30 minutes at 4 ^{o}C, the samples were washed using 70% ethanol. Samples were centrifuged at 15000 xg for 10 minutes and supernatants were removed followed by air-drying of pellets. The samples were dissolved in TE buffer and the concentrations were determined using a NanoDrop Spectrophotometer (ND-1000). After performing restriction enzyme reactions using 600 ng of DNA, each vector was confirmed and expected band sizes were visualized by using agarose gel electrophoresis.

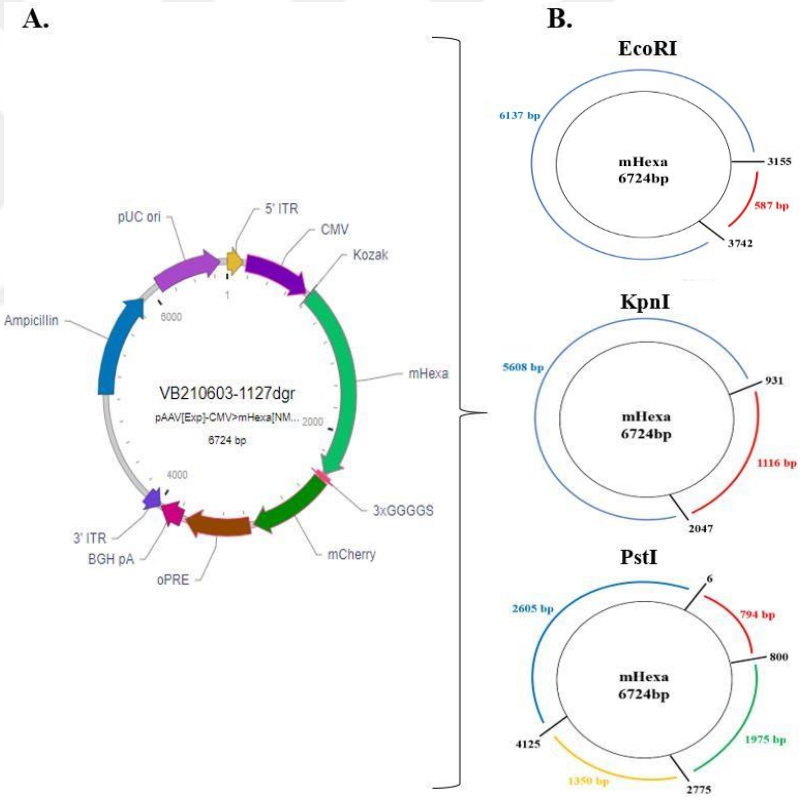

Figure 2.1. (A) A mammalian expression vector encoding mHexa (pAAV-[Exp]-CMV-mHexa-3xGGGGs-mCherry-oPRE) purchased from Vector Builder. (B) The restriction sites and expected band sizes after restriction enzyme reaction using EcoRI, KpnI, and PstI enzymes for mammalian expression vector.

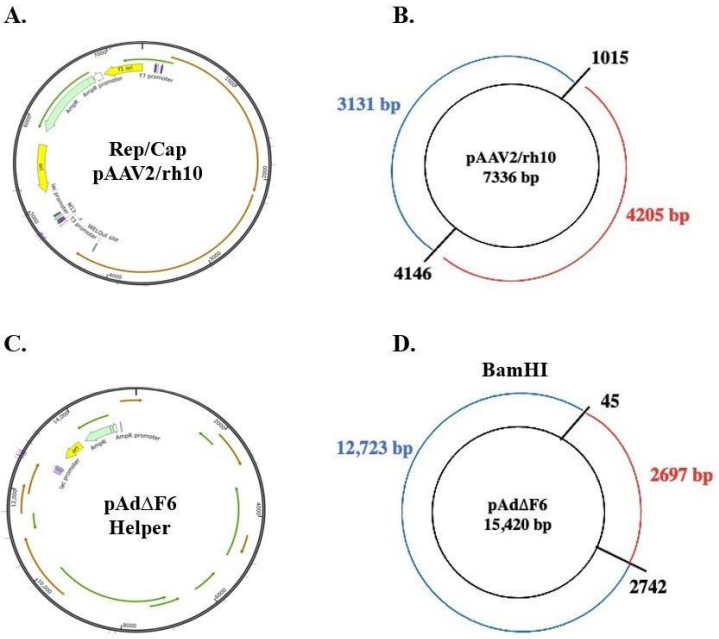

Figure 2.2. (A) AAV2/rh10 and (C) pAdDeltaF6 vectors purchased from Addgene. The restriction sites and expected band sizes after restriction enzyme reaction using BamHI for (B) AAV2/rh10 and (D) pAdDeltaF6 vectors.

2.1.3. Single and Triple Transfection for Confirmation of Vectors

Human embryonic kidney (HEK293T) cells were grown in an incubator under the conditions of 37 ºC, 5% CO_2, and 75% humidity.

To confirm the expression of the mammalian expression vector encoding mHexa, the single transfection of the mammalian expression vector was applied, and the mCherry signal was checked. HEK293T cells were seeded in 6-well cell culture plates (greiner bio-one), cultured in full DMEM (Gibco) containing 10% FBS (Fetal Bovine Serum, Gibco) and 100U/ml of penicillin and 100 µg/ml streptomycin (Gibco) under cell culture conditions. Cells at 70 - 80% confluency were used for the single transfection. Firstly, DMEM was removed, and cells were rinsed with PBS, after which 0.5 ml of serum-free DMEM was added, and cells were incubated for 30 minutes in the incubator under the conditions of 37 ºC, 5% CO_2, and 75% humidity. In this process, two different mixtures were prepared for each well. In the first mixture, 40 µl of NaCI (150 mM) and 3 µl of polyethyleneimine, PEI, (1mg/ml, Thermo Fisher Scientific) were mixed, while the second mixture included the 40 µl of NaCI (150 mM) and 1000 ng of a mammalian expression vector encoding mHexa, isolated by the MegaPrep method. Both two mixtures

were incubated for 10 minutes at room temperature, then mixed and again incubated for 10 minutes. Next, combined mixture was added to each well, and incubated for 3.5 hours under the condition of 37 ºC, 5% CO_2, and 75% humidity. After the incubation process, 2 ml of full DMEM was added to cells and incubated for 16 hours under the same conditions. The next day, all DMEM was removed, and 2 ml of fresh,full DMEM was added and incubated for additional 72 hours at 37 ºC, 5% CO_2, and 75% humidity (Figure 2.3 A). To check the mCherry signal, images were taken at 20X magnification using the fluorescent microscope (Olympus BX53).

The triple transfection of the mammalian expression vector, pAAV2/rh10, and pAdDeltaF6 was also performed, and the mCherry signal was confirmed. Cells at 70 - 80% confluency in cell culture plates (100 mm in diameter, greiner bio-one) were used for the triple transfection. Firstly, DMEM was removed, and cells were rinsed with PBS, after which 5 ml of serum-free DMEM was added, and cells were incubated for 30 minutes in the incubator under the conditions of 37 ºC, 5% CO_2, and 75% humidity. In this process, two different mixtures were prepared. In the first mixture, 350 µl of NaCI (150 mM) and 49 µl of polyethyleneimine, PEI, (1mg/ml, Thermo Fisher Scientific) were mixed, while the second mixture included the 350 µl of NaCI (150 mM) and DNA of vectors including 3500 ng of mammalian expression vector encoding mHexa, 3500 ng of pAAV2/rh10 and 7000 ng of pAdDeltaF6 isolated by the MegaPrep method. Both two mixtures were incubated for 10 minutes at room temperature, then mixed and again incubated for 10 minutes. Next, the combined mixture was added to cells, and incubated for 3.5 hours under the condition of 37 ºC, 5% CO_2, and 75% humidity. After the incubation process, 7 ml of full DMEM was added to cells and incubated for 16 hours under the same conditions. The next day, DMEM was replaced with 20 ml of fresh, full DMEM, and cells were incubated for additional 72 hours at 37 ºC, 5% CO_2, and 75% humidity (Figure 2.3 B) To check the mCherry signal, images were taken at 20X magnification using the fluorescent microscope (Olympus BX53).

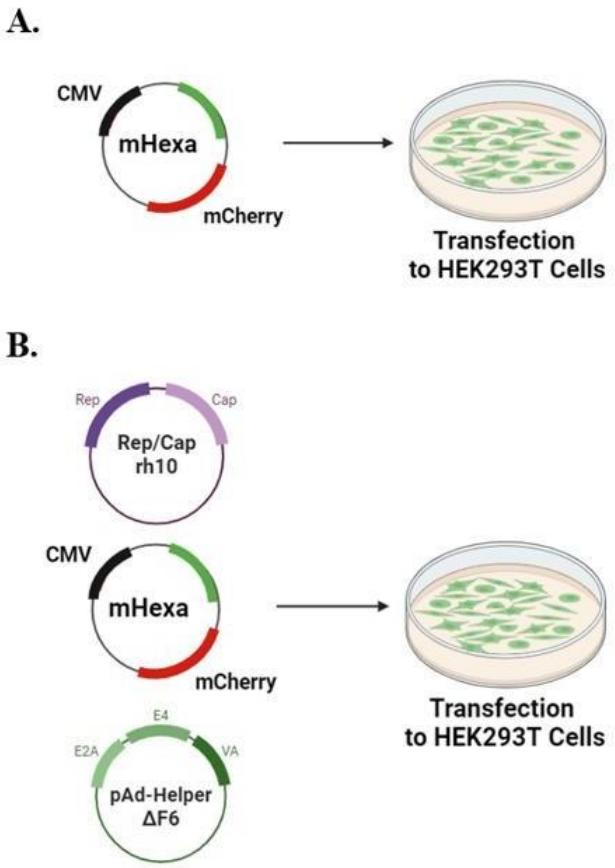

Figure 2.3. (A) Single transfection of a mammalian expression vector encoding mHexa to HEK293Tcells. (B) Triple transfection of AAV2/rh10, mammalian expression vector encoding mHexa, and and pAdΔF6 plasmids to HEK293T cells.

2.1.4. Triple Transfection for Production of AAVrh10-mHexa Virus

Triple transfection of mammalian expression vector, pAAV2/rh10 and pAdDeltaF6 were performed in HEK293T cells to produce the infectious virus particles. To achieve a higher yield of virus particles. 50 cell culture plates (150 mm in diameter, greiner bio-one) were used. When the HEK293T cells reached 70-80% confluency, the full DMEM was removed and 10 ml of serum-free DMEM was added to cells, followed by incubation for 30 minutes under the conditions of 37 ^{o}C, 5% CO_2, and 75% humidity. For each plate, two different mixtures were made. In the first preparation, 1428 µl of NaCI (150 mM) was mixed with 200 µl of polyethyleneimine, PEI, (1mg/ml, Thermo Fisher Scientific) were done. The second preparation consisted of 1428 µl of NaCI and combined with three different plasmids: 10000 ng of mammalian expression vector, and

pAAV2/rh10, and 20000 ng of pAdDeltaF6. Both preparations were incubated seperately for 10 minutes at room temperature, mixed, and incubated for an additional 20 minutes at room temperture. Then, the final mixture was added to cell culture plates and the cells were incubated for 4 hours under the conditions of 37 ^{o}C, 5% CO_2, and 75% humidity. When the incubation process was completed, the 10 ml full DMEM was added to cells and incubated for 16 hours under the same conditions. The next day, DMEM was replaced with 20 ml of fresh, full DMEM, and cells were incubated for an additional 72 hours at 37 ^{o}C, 5% CO_2, and 75% humidity (Figure 2.3 B). At 72 hours post-transfection, the mCherry signal was checked under the fluorescent microscope (Olympus BX53). Cells were detached from the plates using a scraper and centrifuged at 500 xg for 5 minutes at 4 ^{o}C. Supernatants for each transfected plate were removed, and cell pellets were stored at -80 ^{o}C until further processing by the Freeze-Thaw process.

2.1.5. Iodixanol Gradient for Purification of AAVrh10-mHexa Virus

To purify the AAV-rh10mHexa virus particles, collected cells were subjected to freeze and thaw cycles. Firstly, the cell lysis buffer (Table 2.1) was added to collected cells, and samples were incubated alternately at -80 ^{o}C, and 37 ^{o}C for 5 minutes each, repeated three times. The lysed cells were centrifugated at 1,167 xg for 15 minutes at 4 ^{o}C, and the supernatant was transferred into the new tube. To degrade the genomic DNA and any single vector in the supernatant, 16.67 units of Benzonase Nuclease (250 units/µl , Sigma-Aldrich) were added for each transfected cell plate and incubated for 30 minutes at 37 ^{o}C. The samples were mixed for 10 minutes during the incubation process. Afterward, the samples were centrifuged at 13,490 xg for 20 minutes at 4 ^{o}C. The samples were filtered using a 0.45 µm filter (GVS Filtration), and crude lysate was ready for the iodixanol purification method.

OptiPrep Density Gradient medium (Sigma-Aldrich) was utilized to prepare iodixanol solutions with different concentrations (Table 2.1), including 15%. 25%, 40%, and 60%. Each solution was carefully in the layers to Quick Seal centrifuge tubes (Beckman Coulter) to form a gradient. The crude lysate was then added to top layer of the iodixanol gradient (Figure 2.4 A). The prepared Quick Seal centrifuge tubes were centrifugated using a ultracentrifuge (Beckman Coulter) at 200.000 xg at 12 ^{o}C for 2 hours. During the centrifugation, the cell components moved through the gradient based

on their densities, and virus particles (virions) appeared as aqueous, colorless parts within the layer of 40% iodixanol (Figure 2.4 B). The virus particles were collected using a syringe (Figure 2.4 C).

Table 2.1. Solutions used in Iodixanol Gradient Purification Method.

Solutions	**Ingredients**
Cell Lysis Buffer	15 ml 5M NaCl 25 ml 1M Tris –HCL Fill up with ultra-pure water to reach a total volume of 500 ml
10X PBS solution	40 grams NaCl 1-gram KCl 7,2 grams Na_2HPO_4 1,2 grams KH_2PO_4 Fill up with ultra-pure water to reach a total volume of 500 ml
1M $MgCl_2$ solution	20.33 grams $MgCl_2$-$6H_2O$ Fill up with ultra-pure water to reach a total volume of 100 ml
1M KCl solution	7.45 g KCl Fill up with ultra-pure water to reach a total volume of 100 ml
5X PBS – Magnesium Potassium Solution	250 mL 10X PBS 2.5 mL 1 M $MgCl_2$ 6.25 mL 1 M KCl Fill up with ultra-pure water to reach a total volume of 500 ml
%15 Iodixanol	12.5 mL OptiPrep Density Gradient Medium (Sigma-Aldrich) 10 mL 5 M NaCl 10 mL 5x PBS-MK 17.5 mL ultra-pure water
%25 Iodixanol	20.8 mL OptiPrep Density Gradient Medium (Sigma-Aldrich) 10 mL 5x PBS-MK Fill up with ultra-pure water to reach a total volume 19.2 mL Phenol Red (Sigma-Aldrich)

(cont. on next page)

Table 2.1 (cont.)

%40 Iodixanol	33.3 mL of OptiPrep Density Gradient Medium (Sigma-Aldrich) 10 mL 5x PBS-MK 6.7 mL ultra-pure water
%60 Iodixanol	50 mL of OptiPrep Density Gradient Medium (Sigma-Aldrich) Phenol Red (Sigma-Aldrich)

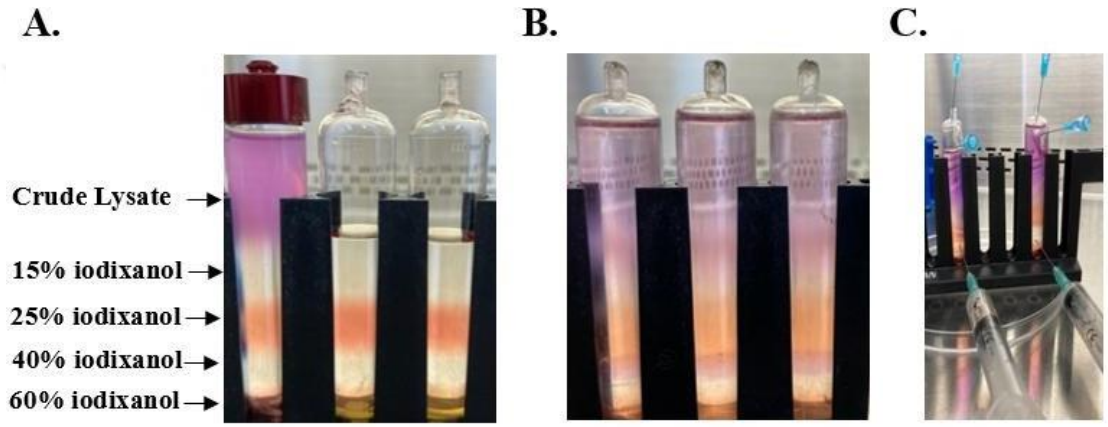

Figure 2.4. Purification of AAVrh10-mHexa virus particles. (A) Preparation of iodixanol gradient using 60%, 40%, 25%, and 15% iodixanol solutions. (B) Iodixanol gradient followed by ultracentrifugation at 200.000 xg for 2 hours. (C) Collection of purified AAVrh10-mHexa virions.

2.1.6. Concentration of AAVrh10-mHexa Virus Particles

To concentrate virus particles, 100 kDa centrifuge filter (Millipore) was used. This filter allowed for the removal of iodixanol solutions smaller than 100 kDa. The filter was rinsed with 1X PBS-MK (Table 2.1) and centrifuged at 4000 xg for 5 minutes. Then, 5 ml of 1X PBS-MK was added to virus particles, and mixture was applied to the filter. The filter was centrifuged at 4000 xg until the final volume was 1ml. Next, 13 ml of 1X PBS-MK was added to the filter and centrifuged three times at 4000 xg for 5 minutes. A non-ionic detergent, 0.01% Pluronic F68, was prepared in 13 ml of 1X PBS and added to filter. The filter was centrifugated at 4000 xg until the final volume was 300 µl. The concentrated virus particles were stored at -20 ^{o}C.

2.1.7. Quantification of AAVrh10-mHexa Virus Particles

The purified and concentrated AAVrh10-mHexa virus particles were quantified using RT-PCR analyses. To quantify the virus titer, DNase treatment was applied to degrade any residual DNA, and vector fragments by adding of 0.5 µl of DNase (1 unit/µl, Themo Scientific), 3 µl of DNase Buffer (10X, Thermo Scientific), and 24,5 µl of distilled water to 2 µl of concentrated virus particles. The samples were incubated for 30 minutes at 37 ^{o}C. To stop the DNase activity, 6 µl of EDTA (25mM, Thermo Scientific) was added to the samples and they were incubated 10 minutes at 65 ^{o}C. After the incubation, 4 µl of Proteinase K Buffer (10X, EcoTech) and 1 µl of Proteinase K (EcoTech) was added to the samples to degrade the protein coat of virus particles and incubated at 50 ^{o}C for 1 hour, followed by incubation at 95 ^{o}C for 20 minutes in order.

To quantify the virus titer, the mammalian expression vector controlled by CMV promoter with different concentrations at 10^{10} vg/µl (viral genome per µl), 10^{9}vg/µl, 10^{8} vg/µl, 10^{7} vg/µl and 10^{6} vg/µl were used as standards (Table 2.2). The purified and concentrated virus particles, and the standards were used for RT-PCR.

Table 2.2. The formulas use to calculate the virus titer.

Formula 1	Vector Molecular Weight [g/mol] = vector size [bp] x 650 [Da/bp] 6724 bp x 650 Da/bp = 4370600 Da
Formula 2	Mole of vector = vector concentration [g/µL] / vector molecular weight [g/mole] $516x10^{-9}$ g/µl / 4370600 g/mol = 11806 x 10^{-17}
Formula 3	The molecule number for vector in µl = mole of vector in µl [mol/µl] x avogadro Number [molecule/mol] 11806 x 10^{-17} mol/µl x $6,022x10^{23}$ = $7,1x10^{10}$ molecule/µL
Formula 4	Vector Stock (100µl) = (required concentration [molecule/µL] x Fill up with ultra-pure water to reach 100 µl) / vector molecule [molecule/µl] ($1x10^{9}$ molecule/µl x100µl) / $7,1x10^{10}$ molecule/µl =1,408 µl (100 µl) 1.4 µL + 98.6 µl dH_2O =$1x10^{9}$ vg/ µL = 4,48 ng/ µl 10 µl from $1x10^{9}$ vg/ µl + 90 µl dH_2O = $1x10^{8}$ vg/ µl = 7,405 ng/µl

(cont. on next page)

Table 2.2 (cont.)

	10 µl from $1x10^8$ vg/ µl + 90 µl dH_2O = $1x10^7$ vg/ µl = 10,93 ng/ µl 10 µl from $1x10^7$ vg/ µl + 90 µl dH_2O = $1x10^6$ vg/ µl = 14,405 ng/ µl
Formula 5	Standard graph equation y = -1,405ln(x) + 32,578
Formula 6	Titer = $e^{(Ct-b)/a}$ x 2 (for scAAV vector)

The reaction mixture for CMV consisting of 1X Roche LightCycler 480 SYBR Green I Master Mix, and 0.4 µM of CMV forward primer, 5'-TCATATGCCAAGTACGCCCC-3', and CMV reverse primer, 5'-CCCGTGAGTCAAACCGCTAT-3', was prepared for each standard and purified virus particle. RT-PCR protocol was applied with the Roche LightCycler® 96 System. Reaction conditions were as follows: 10 minutes at 95˚C; 20 seconds at 95˚C (45 cycles), 15 seconds at 50˚C, and 22 seconds at 72˚C. Then, virus titer (vg/µl) was calculated based on the expression of CMV (Table 2.2), and its concentration was found as $2x10^9$ vg/ µl.

A.

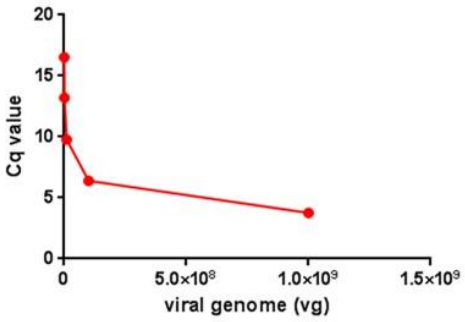

B.

Cq of sample	5,715
Equation **y=-1,405ln(x)+32, 578**	$1x10^8$
vg/µl	$2x10^9$
50 µl injection	**$1x10^{11}$**

Figure 2.5. AAVrh10-mHexa titration by RT-PCR using CMV specific primers. (A) Standard graphic using mammalian expression vector encoding mHexa. x axis refers to viral genome (vg), y axis refers to Cq; quantification cycle. (B) Quantification of AAVrh10-mHexa virions.

2.2. Transduction Test for AAVrh10-mHexa Virus Particles

The effectiveness of the AAVrh10-mHexa virus particles was evaluated using a transduction test on HEK293T cells and neuroglia cells isolated from the 20-weeks of age *Hexa-/-Neu3-/-* mice. Neuroglia cells were isolated from the 20-weeks of age *Hexa-/-Neu3-/-* mice using the Adult Brain Dissociation Kit (MACS Miltenyi Biotec/130-107-677) following the manufacturer's instructions. Both HEK293T cells and neuroglia cells of *Hexa-/-Neu3-/-* mice were cultured in complete DMEM (Gibco) containing 10% FBS (Fetal Bovine Serum, Gibco) and 100U/ml of penicillin and 100 µg/ml streptomycin (Gibco) at 37 ºC with 5% CO_2, and 75% humidity.

For the transduction of HEK293T cells, 100,000 cells were seeded in a 24-well plate (greiner bio-one). The volume of virus particles was calculated to achieve the multiplicity of infection (MOI) as 10,000 using the equation: AAV genome copy particles = MOI x number of cells to be infected. For the injection of 100,000 HEK293T cells, 10^9 genome copy was needed for transduction. Therefore, 0.5 µl of the original viral stock ($2x10^9$) was used for the transduction test. When the HEK293T cells reached 70-80% confluency, the full DMEM was removed from the cells, and the cells were washed with 1X PBS. Then, 0.5 µl of original virus added to 500 µl of DMEM containing 2% FBS, 100U/ml of penicillin and 100 µg/ml streptomycin. This preparation was added to cells and incubated for 20 hours at 37 ºC, 5% CO_2, and 75% humidity. After the incubation, 500 µl of full DMEM was added to cells, which were cultured for 7 days. To check the mCherry signal, images were captured at 20X magnification using the fluorescent microscope (Olympus BX53).

The transduction test was also performed on neuroglia cells from *Hexa-/-Neu3-/-* mice. For this, 10,000 cells were used, and MOI was set to 500,000 due to the lower transduction efficacy of neuroglia cells compared to HEK293T cells. The volume of virus particles was calculated to achieve a MOI of 500,000 using the same equation. For the injection of 10,000 neuroglia cells, $5x10^9$ genome copies were needed for transduction. Therefore, 2.5 µl of original viral stock ($2x10^9$) was used for the transduction test. The same protocol applied to HEK293T cells was also applied to neuroglia cells. mCherry signal was visualized under the fluorescent microscope (Olympus BX53) at 20x.

2.3. Anti-GM2 Staining for Transduced Neuroglia Cells

To evaluate the effect of AAVrh10-mHexa virus particles encoding mHexa on the GM2 ganglioside levels, anti-GM2 staining was performed on transduced neuroglia cells from 20-weeks of age *Hexa-/-Neu3-/-* mice. Cells were rinsed with 1X PBS, and fixed using 4% paraformaldehyde prepared in 1X PBS solution for 30 minutes at room temperature. After the washing of the cells three times with 1X PBS for 3 minutes each, cells were incubated in 0.5% Triton-X100 prepared in 1X PBS at room temperature for 30 minutes followed by incubation in blocking solution (0.3M Glycine, %4 BSA, %0.3 Triton X-100 %10 Goat serum in 1X PBS) for 1 hour. Cells were incubated overnight at 4^{o}C. with the anti-KM966 primary antibody, diluted 1:200 in blocking solution The following day, cells were washed three times with 1X PBS for 5 minutes each, and incubated for 1 hour with Themo Goat anti-Human Cross secondary antibody – SA5-10118 (ThermoScientific), diluted 1:250 in the blocking solution. The cells were then washed three times with 1X PBS for 5 minutes, and cell nuclei were stained with the flouroshield mounting medium (Abcam), DAPI. The fluorescent microscope (Olympus BX53) was used to visualize GM2 ganglioside. The level of GM2 ganglioside was determined with NIH ImageJ (1.48v). The statistical analysis was carried out using One-Way ANOVA in GraphPad Prism 7 (v.7.0a, GraphPad Software, Inc).

2.4. Animals

Hexa-/- and *Neu3-/-* mice were present in the laboratory of Prof. Dr. Volkan Seyrantepe. A mouse model with a combined deficiency of *Hexa* and *Neu3* genes was generated as previously described. All mice housed at the Izmir Institute of Technology Animal Research Center in cages with a maximum of five, maintained at a constant temperature and humidity under a 12-hour light/dark cycle. Food and water were provided *ad libitum*. The use of all animals was approved by the Institutional Animal Care and Use Committee of Izmir Institute of Technology and conducted in accordance with the guidelines set by the Turkish Institute of Animal Health for the use of laboratory animals.

The double knockout mice (*Hexa-/-Neu3-/-*), deficient in both *Hexa* and *Neu3* genes, were sterile and unable to produce offspring. Therefore, double knockout mice

(*Hexa-/-Neu3-/-*) for both genes were produced with the crossing of *Hexa+/-Neu3-/-* females and *Hexa+/-Neu3-/-* males or *Hexa+/-Neu3-/-* males and *Hexa+/-Neu3-/-* females. The produced DKO mice (*Hexa-/-Neu3-/-)* were used in biochemical and immunohistochemistry analyses. *Wild-type (WT*) mice were used as control groups and were produced by crossing *Hexa+/+Neu3+/+* females and *Hexa+/+Neu3+/+* males.

2.5. Mouse Genotyping

Mice were weaned by their parents when they were 4 weeks of age. After weaning, DNA isolation was performed from the tails of mice. 500 µl of lysis buffer consisting of 10% 1M Tris pH 7.6, 2.5% 0.2M EDTA, 20% SDS, 4% 5M NaCl, and 12 µl of Proteinase K (25µg/µl, Sigma- Aldrich) were added to the tails, and incubated overnight at 55ºC using shaking incubator to lyse the tails. The next day, lysed samples were centrifuged for 10 minutes at 14000 rpm, and then supernatants (250 µl) containing DNA were transferred to a new and clean tube followed by the addition of 250 µl of isopropanol for the precipitation of DNAs. Samples were centrifuged at 14000 rpm for 1 minute, and supernatants were discarded. The purification was performed by adding 250 µl of 70% ethanol to pellets. Then, samples were centrifuged for 1 minute at 13000 rpm, and supernatants were discarded. After the air-drying of samples, they were dissolved in 100 µl of distilled water at 55ºC for 1 hour.

Polymerase Chain Reaction (PCR) was used to genotype the mouse for *Hexa* and *Neu3* genes using specific primers (Table 2.3) that recognize the *WT* and KO (knock-out) allele for *Hexa* and *Neu3* genes independently. In reaction tubes, a 50 µl PCR reaction mixture was prepared for *Hexa* gene, consisting of 0.2 µM of HexaF as forward primer, HexaR and PGKR as reverse primers, 0.4 mM of each dNTPs, 10X reaction buffer with $MgCl_2$, 2.5 units of Taq polymerase (GeneDireX) and 100 ng of DNA per sample. The PCR conditions for the *Hexa* gene were set as follows: 95˚C for 3 minutes (initial denaturation); followed by 35 cycles of 94˚C for 45 seconds, 60˚C for 45 seconds, and 72˚C for 1 minute, with a final extension at 72˚C for 5 minutes. *Neu3* gene was also genotyped by preparing a 50 µl of PCR reaction mixture including 0.2 µM of Neu3F as forward primer, Neu3R and NeoR as reverse primers, o.4 mM of each dNTP, 10X reaction buffer with $MgCl_2$, 2.5 units of Taq polymerase (GeneDireX) and 100 ng of DNA per sample. The PCR conditions for the *Neu3* gene were set as follows: 94˚C for 3 minutes

(initial denaturation); followed by 35 cycles of 94˚C for 50 seconds, 58˚C for 45 seconds, and 72˚C for 2 minutes, with a final extension at 72˚C for 10 minutes. Agarose gel electrophoresis was performed to observe the WT and KO alleles for both *Hexa* and *Neu3* genes.

Table 2.3. Primer sequences and product sizes used for genotyping of *Hexa* and *Neu3*.

Gene	Primer	Primer Sequence	Product Size
Hexa	HexaF	5'-GGCCAGATACAATCATACAG-3'	WT Allele: 425 bp KO Allele: 216 bp
	HexaR	5'-CTGTCCACATACTCTCCCCACAT-3'	
	PGKR	5'-CACCAAAGAAGGGAGCCGGT-3'	
Neu3	Neu3F	5'AAGCAGAGAACATTCTTGAGAGAGCACAGC-3'	WT Allele: 1100 bp KO Allele: 600 bp
	Neu3R	5'-TCGTGCTTTACGGTATCGCCGCTCCCGATT-3'	
	NeoR	5'-GTGAGTTCAAGAGCCATGTTGCTGATGGTG-3'	

2.6. Injections

2.6.1. Intrathecal Injection of AAVrh10-mHexa

The intrathecal injections were applied to 8- weeks of age DKO (*Hexa-/-Neu3-/-*) mice to deliver AAVrh10 virus particles encoding mouse Hexa (AAV) to the brain bypassing the blood-brain barrier. As a vehicle control, intrathecal injection of PBS (50 µl) was also applied for 8- weeks of age DKO mice to observe any side-effect of solvent (PBS) used to prepare AAV (Figure 2.6 A). DKO mice were anesthetized intraperitoneally using chemicals including xylazine and ketamine. The spine region was shaved to remove the hairs on this part and was sterilized using betaine and 70% ethanol. Next, a small incision was made using surgical scissors to expose the Lumbar 5-6 region of the spinal cord. The injection of 50 µl of AAV with a $1x10^{11}$vg/µl concentration was performed from this region using an insulin syringe (Figure 2.6 B). Then, the small incision was closed using URGO Pansement spray. Each injected mouse was housed in a

separate cage. DKO mice without any injection and those mice injected with PBS survived until 20-weeks of age, while DKO mice injected with AAV showed extended life spans up to 30-weeks of age.

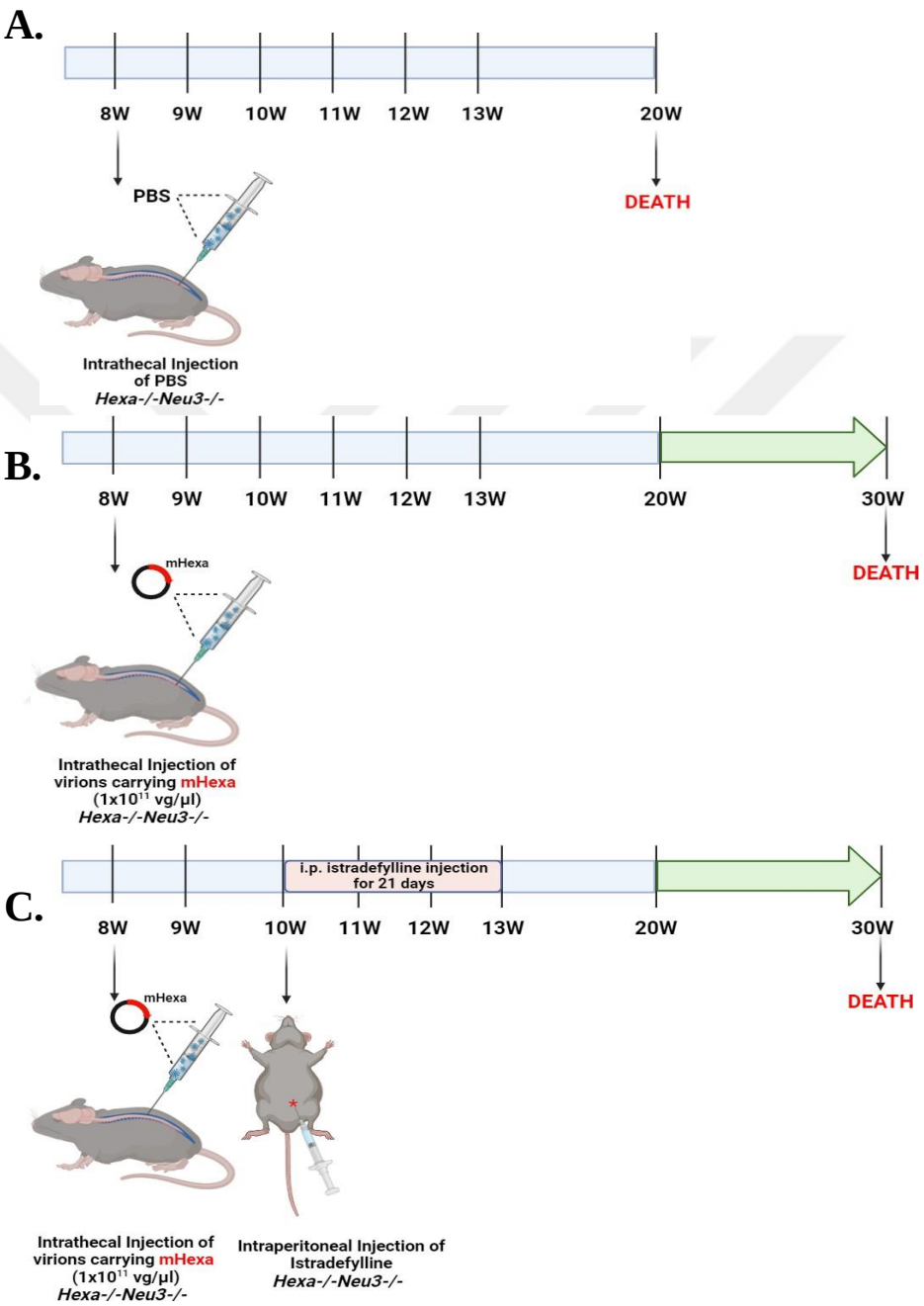

Figure 2.6. Schematic presentation of injection of PBS (A), AAV (B), and AAV with istradefylline (C) into *Hexa-/-Neu3-/-* (DKO) mice.

2.6.2. Istradefylline Infection

Istradefylline, as an anti-inflammatory agent, was injected into 10 weeks of age DKO mice administered with AAV. Istradefylline (5mg/ml, SML0422, Sigma-Aldrich) was dissolved in DMSO, and it was injected intraperitoneally every day for 21 days (Figure 2.6 C). DKO mice administered with AAV and istradefylline survived until 30-weeks of age.

2.7. Experimental Groups

For control groups, 20- and 30- weeks of age *WT* mice did not receive AAV, and istradefylline was used. Experimental groups included 20- and 30-weeks of age DKO mice administered with AAV, and 20- and 30-weeks of age DKO mice administered with AAV and istradeylline to understand the effect of AAV and AAV combined with istradefylline. Additionally, 20- weeks of age DKO mice were compared to 20- and 30-weeks of age DKO mice administered with AAV alone and with AAV combined with istradefylline.

2.8. Body Weight Measurement

The body weights of *WT*, DKO mice, DKO mice administered with AAV, and DKO mice administered with AAV and istradefylline were recorded weekly to assess the changes in body weight of each mouse depending on AAVrh10-mHexa and istradeflylline administration. Firstly, the mass of the beaker was recorded to use as blank. Then, each mouse was put into a beaker and the mass was weighed. The weight of each mouse was calculated by subtraction of the weight of the beaker. 8 different mice for *WT* and DKO mice, 6 different mice for DKO mice administered with AAV, and DKO mice administered with AAV and istradefylline were used for body weight measurements.

2.9. Tissue Handling

The brain, visceral organs (kidney, liver, spleen), and serum of 20- and 30 weeks of age *WT*, 20- weeks of age DKO mice, 20- and 30- weeks of age DKO mice administered with AAV, 20- and 30- weeks of age DKO mice administered with AAV and istradefylline were collected for biochemical and immunohistochemistry analyses.

2.9.1. Brain Dissection

Mice were sacrificed in a CO2 chamber. The brain of each mouse group was removed, and brain sections were dissected into cortex and cerebellum sections. The brain was snap-frozen using liquid nitrogen and stored in a freezer at -80^{o}C.

2.9.2 Tissue Preparation

The visceral organs including the kidney, liver, and spleen were collected following the scarification of mice in a CO2 chamber. The visceral organs were removed, snap-frozen in liquid nitrogen, and stored in a freezer at -80^{o}C.

Serum samples were collected after mice in each group were anesthetized intraperitoneally using chemicals including Xylazine and Ketamine. A small incision was made in the abdomen to access the thoracic cavity, and the heart was punctured with a needle to collect blood samples. HEPES was added to blood samples, which were then centrifugated at 1000 xg for 15 minutes at 4 ^{o}C. The serum part was collected and used in Hexa enzyme activity assay.

2.9.3. Fixation

Mice in each group were anesthetized intraperitoneally using chemicals including Xylazine and Ketamine. The thoracic cavity was opened after the small incision from the abdomen. The right atrium of the heart was cut using sharp scissors, and the needle was placed in the left ventricle of the heart. With the help of the circulation system in our

laboratory, 0.9% NaCI (10 ml), and 4% paraformaldehyde prepared in 1X PBS solution were given to mice for the fixation process. The fixed brains of mice were put into a 4% paraformaldehyde solution and incubated overnight at +4^{o}C. The next day, the sucrose gradient protocol was applied using differently concentrated sucrose solutions prepared in 1X PBS solution. Each mouse brain was put into these sucrose solutions, 10%, 20%, and 30%, in order, and incubated for 2 hours at +4^{o}C. After the sucrose gradient, each mouse brain was placed into embedded boxes filled with OCT. The embedded mice brains were frozen and stored at -80^{o}C. Leica Cryostat (CM1850-UV, Leica) was used to take the coronal sections with 10µm thick from these prepared, fixed mice brains. Each section was placed on the adhesive-coated HistoBond slides, and these prepared slides were stored in the freezer at -80^{o}C for immunohistochemistry analyses.

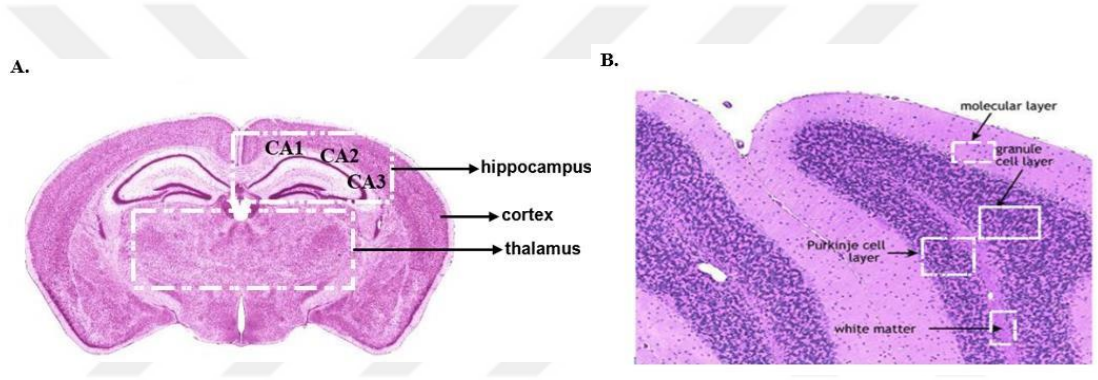

Figure 2.7. The coronal sections of mice brains demonstrate Cortex, Hippocampus, Thalamus (A), and Cerebellum (B) (courtesy of Woods et al., 2013).

2.10. Thin Layer Chromatography Analysis

To evaluate the changes in the ganglioside profile, Thin Layer Chromatography (TLC) analyses were performed for the brain of 20- and 30 weeks of age *WT*, 20- weeks of age DKO mice, 20- and 30- weeks of age DKO mice administered with AAV, 20- and 30- weeks of age DKO mice administered with AAV and istradefylline. Three different mice in each mouse group were used for each mice group.

2.10.1. Acidic Ganglioside Isolation from Brain

50 mg brain of mice brains were used for ganglioside isolation (R. Sandhoff et al., 2002). 2 ml of distilled water was added to weighed cortex sections which were put into borosilicate glass tubes, and samples were homogenized with ultra turax homogenizer (IKA T10, Sigma) at 6000 rpm for 45 seconds. Homogenized samples were sonicated three times for 1.5 minutes using a sonicator (Bandelin Sonopuls). Then, prepared samples were with N_2 flow using Reacti-Thermo Heating module (Thermo). The dried samples were used for the isolation of gangliosides. In the first step, 3 ml of acetone was added, and samples were centrifugated for 5 minutes at 2000 rpm. After centrifugation, supernatant parts were removed. This first step was repeated three times. Then, 1.5 ml of a mixture of methanol:chloroform: water (10:10:1) was put into pellet parts of samples, and samples were centrifugated for 5 minutes at 2000 rpm. Supernatant parts were collected into new and clean neutral glass tubes with a glass Pasteur pipette. This process was also repeated two times. Then, 2 ml of a mixture of methanol:chloroform: water (60:30:8) was added to pellet parts of the samples and centrifugated at 2000 rpm for 5 minutes. After the centrifugation step, supernatants were added to neutral glass tubes including previous supernatant parts. This procedure was also repeated twice, and all supernatants were collected into the same neutral glass tube. These supernatant parts include both neutral and acidic gangliosides.

The neutral and acidic gangliosides were separated using DEAE Sephadex A-25 resin. 1 gram of DAE Sephadex A-25 resin (GE Health Care) was weighed and dissolved in 5 ml of a mixture of methanol:chloroform:0.8M sodium acetate (60:30:8). The prepared DAE Sephadex A-25 resin was incubated at room temperature for 5 minutes, and the upper aqueous phase was removed. Then, 10 ml of a mixture of chloroform: methanol:0.8M sodium acetate (30:60:8) was added to resin and incubated at room temperature for 10 minutes. The upper phase was removed again, and this process was repeated 3 times. 10 ml of a mixture of chloroform: methanol:0.8M sodium acetate (30:60:8) was added to resin and incubated overnight at room temperature. To use this prepared resin, it was washed using 10 ml of a mix of methanol:chloroform:water (60:30:8). On the other hand, columns were prepared to separate neutral gangliosides. To prepare columns, glass woolen was put into glass Pasteur pipettes and an equal volume of prepared resin was added to the Pasteur pipettes including glass woolen. Then, the

solution containing isolated gangliosides and 4 ml of methanol was loaded into prepared columns in order, and the flow-through part including neutral gangliosides was discarded. 500 mM potassium acetate was prepared in methanol, and 5 ml of it was added to columns. The flow-through part including acidic gangliosides was collected into the new, clean neutral glass tubes. For the desalting process, the Superclean LC-18 column (Supelco, Sigma) was placed on a Chromabond Vacuum system (Macherey-Nagel) and 5 Hg stable pressure was set in this system. The equilibration step was done by adding 2 ml of methanol and 500 mM potassium acetate prepared in methanol to Superclean LC-18 columns. Then, the columns were washed using 10 ml of distilled water, and the elution step was performed using 4 ml of methanol and 4 ml of a mix of methanol:chloroform (1:1). In the elution step, the collected flow-through part including acidic gangliosides were evaporated using N_2, and stored at +4^{o}C.

2.10.2. Thin Layer Chromatography

The acidic gangliosides were loaded onto silica plates (Merck, New Jersey, USA), and separated depending on weights. During the loading process, silica plates were heated at 100°C for 30 minutes. Then, 100 µl of a mix of methanol:chloroform:water (10:10:1) was added to solve the acidic gangliosides. 45 µl of dissolved acidic gangliosides were loaded onto silica plates with Linomat 5 equipment (Camag, Muttenz, Switzerland). The prepared silica plate was placed into a TLC tank including running solution (chloroform:methanol:0.2% $CaCl_2$ (30:65:8) after the incubation of the tank for 1 hour 45 minutes. The running process was performed for 1 hour.

2.10.3. Orcinol Staining of Plates and Visualization

The visualization of acidic gangliosides was done using an orcinal solution. The orcinal solution was prepared using 0.05 grams of orcinol, 10 ml of acetone, and 0.5 ml of sulfuric acid, and then the silica plate was stained using this prepared orcinol solution. The stained silica plates were heated by using a TLC plate heater (Camag, Muttenz) at 120°C until the gangliosides were visible. The silica plates were scanned with an HP scanner, and band intensities were determined using NIH ImageJ (1.48v). The statistical

analysis was done using One-Way ANOVA on GraphPad Prism 7 (v.7.0a, GraphPad Software, Inc).

2.11. Enzyme Activity Assay

The Hexa enzyme activity was evaluated using a substrate specific for the Hexa enzyme in the brain (cortex and cerebellum), visceral organs (kidney, liver, spleen) and serum of 20- and 30 weeks of age *WT* mice, 20- weeks of age DKO mice, 20- and 30-weeks of age DKO mice administered with AAV, 20- and 30- weeks of age DKO mice administered with AAV and istradefylline.

For tissue samples (excluding serum) 50 mg of each sample was weighed, and 150 µl of distilled water was added to the samples followed by homogenization with ultra turax homogenizer (IKA T10, Sigma). The homogenized samples were then sonicated twice for 5 seconds using a sonicator (Bandelin Sonopuls). For serum samples, 20 µl of serum was used directly without any homogenization and sonication process. 50 µl of Hexa substrate (4-Methylumbelliferyl 6-Sulfo-2-acetamido-2-deoxy-β-D-glucopyranoside Potassium Salt, sc-223640A), and 40 µl of 0.1M sodium acetate (pH 4.5) were put onto completely homogenized samples and incubated in the water bath at 37 for 30 minutes at 37ºC. A blank control included 50 µl of Hexa substrate, and 40 µl of 0.1M sodium acetate (pH 4.5) without any sample. To stop the enzyme reaction, 3.9 ml of 0.4 M glycine buffer (pH 10.4) was added to the samples. Absorbance was detected using a spectrophotometer (RF-5301). The specific enzyme activity levels were calculated based on absorbance values and the protein content in each sample. Bradford assay was performed to calculate the concentration of proteins. 10 µl of 1:10 diluted protein samples loaded to a 96-well plate, followed by the addition of 200 µl of Bradford reagent (SERVA Electrophoresis GmbH) to each well. The 96-well plate was incubated at room temperature for 10 minutes in the dark. The absorbance of all samples was measured at 595 nm in an i-Mark Microplate Absorbance Reader (Bio-Rad Laboratories). The specific enzyme activity was expressed in µmol/mg of protein. The statistical analysis was done using One-Way ANOVA on GraphPad Prism 7 (v.7.0a, GraphPad Software, Inc).

2.12. Real-Time PCR

The gene expression analyses were performed using Real-Time PCR (RT-PCR). The brain (cortex and cerebellum) and visceral organs (kidney, liver, spleen) of 20- and 30 weeks of age *WT*, 20- weeks of age DKO mice, 20- and 30- weeks of age DKO mice administered with AAV, 20- and 30- weeks of age DKO mice administered with AAV and istradefylline were used for RNA isolation, cDNA synthesis, and Real-Time PCR protocols. Three different mice in each mouse group were used for Real-Time PCR analyses.

2.12.1. RNA Isolation

The brain and visceral organs were used for RNA isolation protocol. 50 mg of brain and visceral organs were weighed and 1 ml of Trizol reagent (ABP Biosciences) was added to the samples. Each sample was lysed using a homogenizator (Retsch MM100), and incubated at room temperature for 5 minutes. The samples were centrifugated for 5 minutes at 12000 xg at 4^{o}C, and the supernatants were taken to Eppendorf tubes. For phase separation, 200 µl of chloroform was added and mixed roughly for 10 seconds. After the incubation of samples at room temperature for 2 – 3 minutes, samples were centrifugated for 15 minutes at 12000 xg at 4^{o}C. The upper aqueous phases were transferred to the new Eppendorf tube, and 500 µl of isopropanol was added to the sample for the precipitation of RNA. The samples were incubated at room temperature for 10 minutes, and then centrifugated for 10 minutes at 12000 xg at 4^{o}C. The supernatants were discarded, and 1 ml of 75% ethanol was added to pellet parts including RNA. The samples were centrifugated for 5 minutes at 7500 xg at 4^{o}C. Supernatant parts were removed, and RNA pellets were incubated at 55 ^{o}C to dry. The dried RNA samples were dissolved in RNase-free water and incubated at 55 ^{o}C in the water bath for 10 minutes. The concentration of RNA samples was determined by using a NanoDrop Spectrophotometer (ND-1000).

2.12.2. cDNA Synthesis

The isolated RNA samples were converted to cDNA using an iScript cDNA synthesis Kit (BioRad). A total of 500 ng of RNA was synthesized into cDNA in a 10 µl reaction by adding 2 µl of iScript mix (5X), 0.5 µl of reverse transcriptase, 500 ng of RNA, and nuclease-free water to reach the final volume. The conditions for cDNA synthesis were as follows: 5 minutes at 25˚C; 20 minutes at 46˚C, and 1 minute at 95˚C.

PCR was applied to confirm that all RNA samples are converted to cDNA using specific primers for a housekeeping gene, GAPDH. In reaction tubes, a 25 µl PCR mix was prepared, consisting of 0.8 mM of forward and reverse GAPDH primers, 10 mM dNTPs, 1X reaction buffer with $MgCl_2$, 1.5 unit of Taq polymerase (GeneDireX) and 50 ng of cDNA per sample. The PCR conditions were set as follows: 95˚C for 3 minutes (initial denaturation); followed by 30 cycles of 95˚C for 20 seconds, 65˚C for 15 seconds, and 72˚C for 20 seconds, with a final extension at 72˚C for 3 minutes. The PCR product was visualized using agarose gel electrophoresis.

2.12.3. Real-Time PCR (RT-PCR)

To understand the effect of administration of AAV encoding mHexa, the expression level of mouse Hexa (mHexa) was analyzed among mice groups with RT-PCR. In the brain sections (cortex and cerebellum) of each mice group, the gene expression ratios of neuroinflammatory-related markers such as CCL2, CCL3, CCL5, Cxcl10, IL1-β, Iba1, and GFAP were determined. Additionally, the gene expression levels of inflammation-related and lysosome-related markers were also determined. The expression levels of inflammatory-related markers including CCL2, CCL3, CCL5, Cxcl10, and IL1-β were evaluated for visceral organs, kidney, liver, and spleen. Furthermore, the expression level of the lysosome-related marker, Lamp-1, was also analyzed for both the brain and visceral organs of each mouse group.

Table 2.4. Forward and reverse primer sequences in RT-PCR.

Gene	Primer Sequences
mHexa	F: 5'- CACCAGGGCTGGCTTCC -3' R: 5'- CATGAAACGCCAGGGGCT -3'
CCL2	F:5'-ATGCAGTTAATGCCCCACTC -3' R:5'-TTCCTTATTGGGGTCAGCAC -3'
CCL3	F:5'-TCTGTACCATGACACTCTGC- 3' R:5'- AATTGGCGTGGAATCTTCCG-3'
CCL5	F:5'-AGTGCTCCAATCTTGCAGTC-3' R:5'-AGCTCATCTCCAAATAGTTG-3'
Cxcl10	F:5'-CACCATGAACCCAAGTGCTGCCGT-3' R:5'-AGGAGCCCTTTTAGACCTTTTTTG-3'
IL1-β	F:5'-TGAGTCACAGAGGATGGGCTC-3' R:5'-CCTTCCAGGATGAGGACATGA-3'
Iba1	F: 5'-TCTGCCGTCCAAACTTGAAGCC-3' R: 5'-CTCTTCAGCTCTAGGTGGGTCT-3'
GFAP	F:5'-AGTAACATGCAAGAGACAGAG - 3' R:5'- TAGTCGTTAGCTTCGTGCTTG-3'
Lamp1	F:5'- CCAGGCTTTCAAGGTGGACAGT-3' R:5'- GGTAGGCAATGAGGACGATGAG-3'
GAPDH	F: 5'-CCCCTTCATTGACCTCAACTAC-3' R: 5'-ATGCATTGCTGACAATCTTGAG-3'

The reaction mixture for each analyzed gene consisting of 50 ng of cDNA, 1X Roche LightCycler 480 SYBR Green I Master Mix, and 0.4 μM forward and reverse primer (Table 2.4) was prepared. RT-PCR protocol was applied with the Roche LightCycler® 96 System. Reaction conditions were as follows: 10 minutes at 95˚C; 20 seconds at 95˚C (45 cycles), 15 seconds at 60˚C, and 22 seconds at 72˚C. The gene expression ratio of the housekeeping gene GAPDH was analyzed and used as an internal control for the normalization of other analyzed genes. The statistical analysis was carried out using One-Way ANOVA in GraphPad Prism 7 (v.7.0a, GraphPad Software, Inc).

2.13. Western Blot

Western Blot analyses were performed to understand the gene expression levels of IL-1β, NF-κB, and IκB-α on the protein level. The brain (cortex and cerebellum) and

visceral organs (kidney, liver, spleen) of 20- and 30 weeks of age *WT*, 20- weeks of age DKO mice, 20- and 30- weeks of age DKO mice administered with AAV, 20- and 30-weeks of age DKO mice administered with AAV and istradefylline were used for protein isolation and SDS-PAGE gel electrophoresis. Three different mice in each mouse group were used for Western Blot analyses.

2.13.1. Protein Isolation

Protein isolation was performed on the brain and visceral organs of each mouse group. Lysis buffer was prepared by the addition of 50 mM HEPES, 150 mM NaCI, 1% TritonX100, 50 mM Tris-Base, and 10% Glycerol. To prevent the degradation of proteins, protease inhibitors such as PMSF and protease inhibitor cocktail (PI) were added to the lysis buffer at a 1% concentration. A total of 20 mg of brain and visceral organs were lysed in 1 ml of lysis buffer containing protease inhibitors. The brain and visceral organs were homogenized using a mini homogenizer. Samples were then incubated on ice, and vortexed for every 10 minutes for 1 hour. The homogenized samples were centrifugated at 14000 rpm, for 10 minutes at 4 ^{o}C. The supernatant parts were collected as protein stock, while the pellet parts were discarded.

2.13.2. Bradford Assay and Protein Preparation

The protein concentration of each sample was determined using the Bradford reagent. Isolated proteins and lysis buffer were diluted 1:10 using distilled water. Bovine Serum Albumin – BSA (Sigma-Aldrich) standards were prepared at concentrations of 0.1 mg/ml, 0.2 mg/ml, 0,4 mg/ml, 0.8 mg/ml, and 1mg/ml in distilled water. These concentrated BSA solutions were used to draw a standard curve. A total of 10 µl of BSA standards, diluted protein samples, and lysis buffer were loaded to a 96-well plate, followed by the addition of 200 µl of Bradford reagent (SERVA Electrophoresis GmbH) to each well. The 96-well plate was incubated at room temperature for 10 minutes in the dark. The absorbance of all samples was measured at 595 nm in an i-Mark Microplate Absorbance Reader (Bio-Rad Laboratories). A standard curve was plotted using the BSA absorbance values, and the equation derived from the standard curve was used to calculate the protein concentrations of the samples. Protein samples were adjusted to a

concentration of 20 µg by combining protein water. The Loading dye was prepared by using 8%SDS, 40% Glycerol, 240 mM Tris-HCl, 0.04%Bromophenol Blue, and 5% β-mercaptoethanol, with the pH adjusted to 6.8. The loading dye was mixed with prepared proteins in a 4:1 ratio. The samples were heated at 95^0C for 10 minutes and subsequently used for SDS-PAGE gel electrophoresis.

2.13.3. SDS-PAGE Gel Electrophoresis

In SDS-PAGE electrophoresis, proteins were separated based on their molecular weights. The resolving and stacking gels were prepared using ingredients shown in Table.2.5.

Table 2.5. Ingredients of stacking and resolving gels used in SDS gel electrophoresis.

Stacking Gel (5%)	**Resolving Gel (10%)**
1.5 ml Upper Buffer (1M Tris-HCI)	3 ml Lower Buffer (1.5M Tris-HCI)
1 ml 30% Acrylamide	4 mL 30% Acrylamide
3.5 ml distilled water	5 ml distilled water
60 µl 10% SDS	60 µl 10% SDS
60 µl 10% APS	60 µl 10% APS
6 µl TEMED	6 µl TEMED

After pouring and polymerizing the resolving gel, the stacking gel was poured, and the comb was placed into this gel. The comb was then removed, and prepared gels inside the glass were placed in a cell buffer dam. The running buffer, consisting of 0.25M Tris-Base, 1.92M Glycine, 1%SDS, was poured into the cell buffer dam. The protein ladder (GeneDireX), and prepared protein samples were loaded into the wells. The voltage of the system was set to 80V until the proteins reached the resolving gel, after which the proteins were run on the resolving gel at 120V for 1 hour. Next, the separated proteins were transferred to a nitrocellulose membrane (Bio-Rad) using the sandwich method with transfer cassettes in a transfer buffer (48mM Tris-Base, 39mM Glycine, 20%Methanol, pH 9.2) at a constant current of 25mA for 1 hour 15 minutes. To prevent the nonspecific binding of primary antibodies, blots were incubated in the blocking

solution (5% BSA in PBS-Tween) for 1 hour at room temperature. After blocking, the blots were washed using PBS-Tween 3 times for 5 minutes at room temperature. To visualize the specific proteins on the blots, the primary antibodies including IL-1β (Cell Signalling Technology), NF-κB (abcam), and IκB-α (abcam) were diluted at 1:1000 ratio in the red solution containing 0.02 % NaAzide, Pheno Red, 5%BSA in PBS-Tween, pH 7.5). As a housekeeping gene, β-actin was diluted in the red solution at a 1:1000 ratio. The blots were incubated with primary antibodies overnight at 4^{o}C, followed by washing with PBS-Tween 3 times for 5 minutes each. HRP-conjugated secondary antibody (Jackson ImmunoResearch Lab) was added to blots and incubated for 1 hour at room temperature. Before visualizing the blots, they were washed using PBS-Tween 3 times for 5 minutes. Proteins were detected with the LuminataTM Forte Western HRP Substrate (Millipore) on imaging system (BioRad). Band intensities were determined using NIH ImageJ (1.48v). The statistical analysis was carried out using One-Way ANOVA on GraphPad Prism 7 (v.7.0a, GraphPad Software, Inc).

2.14. Immunohistochemistry Analyses

The cortex, hippocampus, thalamus, and cerebellum parts of 20- and 30 weeks of age *WT*, 20- weeks of age DKO mice, 20- and 30- weeks of age DKO mice administered with AAV, 20- and 30- weeks of age DKO mice administered with AAV and istradefylline were analyzed in immunohistochemistry. GM2, Lamp1, NeuN, CNPase, and GFAP staining were performed for immunohistochemistry analyses. Three different mice in each mouse group were used for immunohistochemistry analyses.

2.14.1. Anti-GM2 Staining

Anti-GM2 staining was performed to evaluate the changes in accumulating GM2 ganglioside in DKO mice with the administration of AAV alone and together with istradefylline. The GM2 ganglioside level was determined in the brain section of each mouse group. KM966 primary antibody that recognizes the GM2 ganglioside was utilized for this staining.

Previously prepared slides were placed in a humidified chamber and incubated for 10 minutes on ice and then incubator at 55^{o}C for 10 minutes. Then, the slides were washed with 1X PBS for 10 minutes at room temperature. Cold acetone was added to slides and incubated for 10 minutes at room temperature to permeabilize the brain sections. Slides were washed with 3 times 1X PBS for 5 minutes each and followed by the determination of the edges of brains using a PAP pen (Sigma-Aldrich). The blocking solution (0.3M Glycine, %4 BSA, %0.3 Triton X-100 %10 Goat serum in 1X PBS) was added to slides and incubated for 1 hour at room temperature. After blocking, the anti- KM966 primary antibody was diluted 1:250 in blocking solution, and the prepared antibody was added to each brain on the slide. Then, slides were put into humidified chambers and incubated overnight at 4^{o}C. The next day, slides were washed three times with 1X PBS for 5 minutes each. Themo Goat anti-Human Cross secondary antibody – SA5-10118 (ThermoScientific) was used as a secondary antibody, and it was diluted in the blocking solution in a ratio of 1:250. The secondary antibody was added to slides and incubated for 1 hour at room temperature in the dark. Then, slides were washed three times with 1X PBS for 5 minutes. The flouroshield mounting medium (Abcam), DAPI, was added to slides to stain the cell nuclei. Slides were covered using coverslips. The fluorescent microscope (Olympus BX53) was used to visualize GM2 ganglioside. The level of GM2 ganglioside was determined with NIH ImageJ (1.48v). The statistical analysis was carried out using One-Way ANOVA in GraphPad Prism 7 (v.7.0a, GraphPad Software, Inc).

2.14.2. Anti-Lamp1 Staining

The level of lysosomes was detected using anti-Lamp1 staining for each mouse group. An anti-Lamp1 primary antibody was used to recognize the lysosomes.

Previously prepared and stored slides were placed in a humidified chamber and incubated for 10 minutes on ice and then incubator at 55^{o}C for 10 minutes. The slides were washed with 1X PBS for 10 minutes, followed by incubation with cold methanol for 10 minutes at room temperature. To remove the methanol on brain samples, slides were washed with 1X PBS for 5 minutes at room temperature. The edges of each brain on the slide were outlined using a PAP pen (Sigma-Aldrich). To prevent the nonspecific binding, a blocking solution consisting of 0.3M Glycine, %4 BSA, %0.3 Triton X-100

%10 Goat serum in 1X PBS, was prepared and added to slides. The slides were incubated for 1 hour at room temperature. Next, the primary antibody, anti-Lamp1 (Cell Signalling Technology), was diluted 1:250 in the blocking solution and added to the slides. The slides were incubated overnight at 4°C with an anti-Lamp1 primary antibody. After primary antibody incubation, the slides were washed 3 times with 1X PBS for 5 minutes each. Anti-rabbit Alexa Fluor®-488 (Abcam) as a secondary antibody was diluted 1:500 in the blocking solution. The slides were incubated with secondary antibody for 1 hour at room temperature in the dark. The slides were then washed three times with 1 X PBS for 5 minutes each. Flouroshield mounting medium, DAPI (Abcam), was used to stain the cell nuclei, and slides were covered with coverslips. The images were captured using a fluorescent microscope (Olympus BX53) to visualize the lysosomes. Image analysis, including intensity and colocalization, was performed with NIH ImageJ (1.48v). The statistical analysis was carried out using One-Way ANOVA in GraphPad Prism 7 (v.7.0a, GraphPad Software, Inc).

2.14.3. Anti-NeuN Staining

Anti-NeuN staining was done to determine the neuron intensity in the brain section of each mouse group. Anti-NeuN primary antibody that recognizes the neurons was utilized for this staining.

Previously prepared and stored slides were placed in a humidified chamber and incubated for 10 minutes on ice and then incubator at 55^{o}C for 10 minutes. Next, a washing process was applied for each slide using 1X PBS for 10 minutes at room temperature. Cold acetone was added to slides and incubated for 10 minutes at room temperature for permeabilization of brain sections. Slides were washed with 3 times 1X PBS for 5 minutes each and followed by incubation in 100% cold methanol for 10 minutes at room temperature. The slides were also washed with 1X PBS and the edges of each brain on the slide were outlined using a PAP pen (Sigma-Aldrich). To prevent the nonspecific signal, blocking solution (0.3M Glycine, %4 BSA, %0.3 Triton X-100 %10 Goat serum in 1X PBS) was added to slides and incubated for 1 hour at room temperature. Following the 1-hour incubation, the anti-NeuN primary antibody (Cell Signaling Technology) was diluted 1:50 in blocking solution, and the prepared antibody was added to each brain on the slide. Then, slides were put into humidified chambers and incubated

overnight at 4^{o}C. The next day, slides were washed three times with 1X PBS for 5 minutes each. Anti-rabbit Alexa Fluor®-488 (Abcam) was used as a secondary antibody, and it was diluted in the blocking solution in a ratio of 1:500. The secondary antibody was added to slides and incubated for 1 hour at room temperature in the dark. After incubation of the secondary antibody, slides were washed three times with 1X PBS for 5 minutes. DAPI, known as flouroshield mounting medium (Abcam) was added to slides for the determination of the nucleus. Slides were covered using coverslips. The fluorescent microscope (Olympus BX53) was used to visualize the neurons. The neuron intensity analysis was performed with NIH ImageJ (1.48v). The statistical analysis was carried out using One-Way ANOVA in GraphPad Prism 7 (v.7.0a, GraphPad Software, Inc).

2.14.4. Anti- CNPase Staining

The intensity of oligodendrocytes and demyelination process was determined using anti-CNPase staining for each mouse group. Anti-CNPase primary antibody was used to recognize the oligodendrocytes.

Previously prepared and stored slides were placed in a humidified chamber and incubated for 10 minutes on ice and then incubator at 55^{o}C for 10 minutes. Next, slides were washed three times in 1X PBS for 5 minutes each. 100% cold methanol was added to slides and incubated for 10 minutes at room temperature. The slides were also washed with 1X PBS and the edges of each brain on the slide were outlined using a PAP pen (Sigma-Aldrich). To prevent the nonspecific binding, a blocking solution (0.3M Glycine, %4 BSA, %0.3 Triton X-100 %10 Goat serum in 1X PBS) was added to slides and incubated for 1 hour at room temperature. After blocking, the primary antibody, anti-CNPase (Cell Signaling Technology), was diluted 1:100 in the blocking solution and added to the slides. The slides were incubated overnight at 4°C with the primary antibody. On the following day, the primary antibody was removed from slides and the slides were washed 3 times with 1X PBS for 5 minutes each. Anti-rabbit Alexa Fluor®-488 (Abcam) was used as a secondary antibody, diluted 1:500 in the blocking solution. The slides were incubated with secondary antibody for 1 hour at room temperature in the dark. Afterward, the slides were washed three times with 1 X PBS for 5 minutes each. Flouroshield mounting medium, DAPI (Abcam), was used to stain the cell nuclei, and slides were covered using coverslips. The images were captured using a fluorescent microscope

(Olympus BX53) to visualize the oligodendrocytes. Image analysis, including intensity and colocalization, was performed with NIH ImageJ (1.48v). The statistical analysis was carried out using One-Way ANOVA in GraphPad Prism 7 (v.7.0a, GraphPad Software, Inc).

2.14.5. Anti-GFAP Staining

The presence of astrocytes was determined using anti-GFAP staining for each mouse group. An anti-GFAP primary antibody was used to recognize the astrocytes.

Previously prepared and stored slides were placed in a humidified chamber and incubated for 10 minutes on ice and then incubator at 55^{o}C for 10 minutes. Next, slides were washed three times in 1X PBS for 5 minutes each. The edges of each brain on the slide were outlined using a PAP pen (Sigma-Aldrich). To prevent the nonspecific binding, a blocking solution consisting of 0.3M Glycine, %4 BSA, %0.3 Triton X-100 %10 Goat serum in 1X PBS, was prepared and added to slides. The slides were incubated for 1 hour at room temperature. Next, the primary antibody, anti-GFAP (Sigma-Aldrich), was diluted 1:200 in the blocking solution and added to the slides. The slides were incubated overnight at 4°C with an anti-GFAP primary antibody. After primary antibody incubation, the slides were washed 3 times with 1X PBS for 5 minutes each. Anti-rabbit Alexa Fluor®-488 (Abcam) as a secondary antibody was diluted 1:500 in the blocking solution. The slides were incubated with secondary antibody for 1 hour at room temperature in the dark. Afterward, the slides were washed three times with 1 X PBS for 5 minutes each. Flouroshield mounting medium, DAPI (Abcam), was used to stain the cell nuclei, and slides were covered using coverslips. The images were captured using a fluorescent microscope (Olympus BX53) to visualize the active astrocytes. Image analysis, including intensity and colocalization, was performed with NIH ImageJ (1.48v). The statistical analysis was carried out using One-Way ANOVA in GraphPad Prism 7 (v.7.0a, GraphPad Software, Inc).

2.15. Behavioral Test

Behavioral tests such as rotarod and footprint were performed to evaluate the changes in the behaviors in mice groups. Six different mice in each mouse group were used for behavioral analyses.

2.15.1. Rotarod Test

The motor coordination and balance were assessed using the rotarod test (Seyrantepe et al., 2018). Each mouse was put on a rotating rod and trained to walk. After the training session, each mouse was placed on the accelerating rotating rod Pan-Lab Harvard Apparatus), and the latency time to fall was recorded with Sedacom version 2.0 (Harvard Apparatus). The speed of the rotating rod started at 4 rpm and accelerated to 40 rpm over 3 minutes. The experiment was repeated three times for each mouse. The mice were given a 15-minute resting period between trials. The statistical analysis was carried out using One-Way ANOVA in GraphPad Prism 7 (v.7.0a, GraphPad Software, Inc).

2.15.2. Footprint Test

The walking pattern of mice was determined using the Footprint test. Nontoxic ink was used to paint both the fore and hind paws of each mouse. The mice were then given the opportunity to walk along the runway on white paper in a closed box. The paper was scanned using an HP scanner and the stride, sway, and stance lengths were calculated. The statistical analysis was carried out using One-Way ANOVA in GraphPad Prism 7 (v.7.0a, GraphPad Software, Inc).

CHAPTER 3

RESULTS

3.1. The Production of AAVrh10-mHexa Virus Particles

3.1.1. Confirmation of Vectors

The mammalian expression vector encoding mHexa (pAAV-[Exp]-CMV-mHexa-3xGGGGs-mCherry-oPRE), packaging vector, AAV2/rh10, and helper vector, pAdDeltaF6, were confirmed with the restriction enzyme reactions after the isolation using Alkaline Lysis Purification, and Mega Kit isolation protocols.

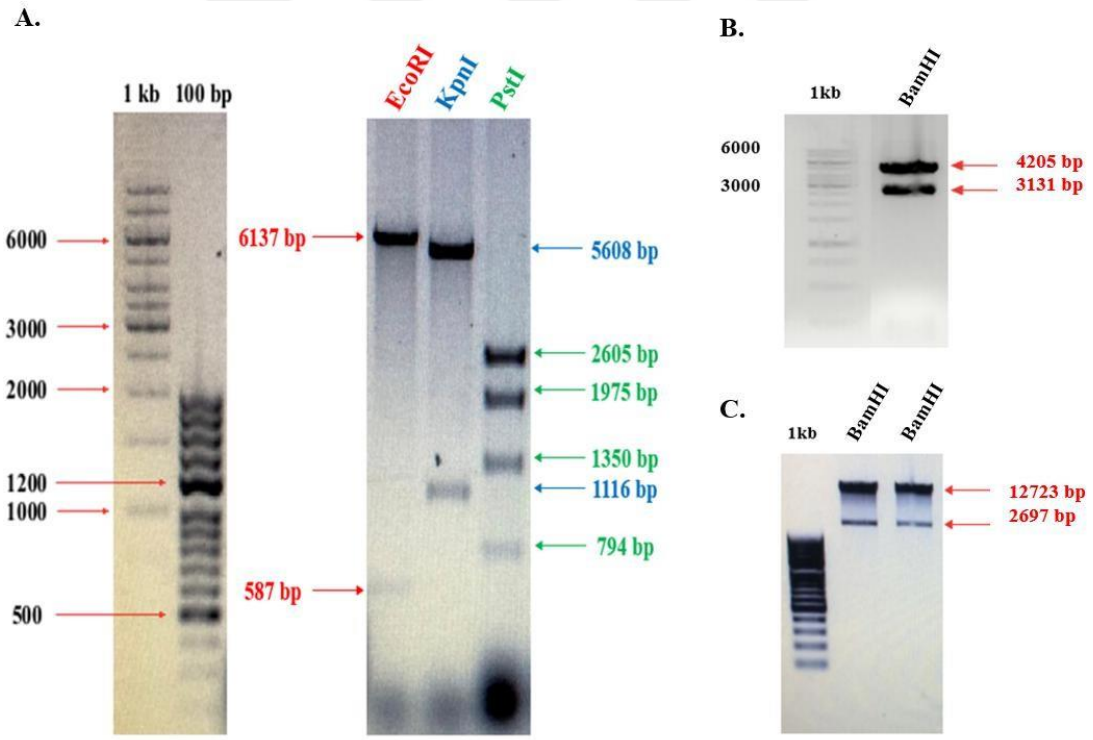

Figure 3.1. Agarose gel electrophoresis results showing restriction enzyme digestions: (A) EcoRI, KpnI, and PstI digestion of the mammalian expression vector encoding mHexa (pAAV-[Exp]-CMV-mHexa-3xGGGGs-mCherry-oPRE); (B) BamHI digestion of the AAV2/rh10 (Rep/Cap) vector; and (C) the pAdDeltaF6 vector after isolation using the Megaprep kit.

The expected band sizes for each vector were determined based on the restriction enzyme sites. The mammalian expression vector had a size of 6724 bp, with EcoRI cutting at 3155 bp, and 3741 bp, producing fragments of 587 bp and 6137. KpnI restriction enzyme cut this vector at 931 bp and 2047 bp, resulting in fragments of 1116 bp and 5608 bp. For PstI, the restriction sites were located at 6 bp, 800 bp, 2775 bp and 4125 bp, generating fragments of 794 bp, 1975 bp, 1350 bp and 2605 bp, as demonstrated in Figure 3.1 A. All expected bands were visualized on the agarose gel after the restriction enzyme reactions of EcoRI , KpnI, and PstI.

BamHI restriction enzyme was used to digest both the AAV2/rh10 vector and the pAdDeltaF6 vector. AAV2/rh10 vector was cut at 1015 bp and 4146 bp, producing fragments of 3131 bp and 4205 bp. In the case of the pAdDeltaF6 vector, BamHI cut at 45 bp and 2742 bp, resulting in fragments of 2697 bp and 12723 bp. Based on the restriction sites, the expected bands were observed on agarose gel for both AAV2/rh10 (Figure 3.1 B) and pAdDeltaF6 (Figure 3.1 C) vectors.

3.1.2. Single and Triple Transfection for Confirmation of Vectors

To confirm the expression of the mammalian expression vector encoding mHexa, both single and triple transfections were performed in HEK293T cells. The single transfection included the mammalian expression vector, while triple transfection involved the mammalian expression vector, packaging vector (AAV2/rh10) and helper vector, (pAdDeltaF6). The efficiency of transfection was controlled by mCherry signal, which produced a red fluorescence under the fluorescent microscope (Figure 3.2).

The observation of mCherry signal in both single and transfections demonstrated the successful transfection of mammalian expression vector into HEK293T cells (Figure 3.2). The presence of mCherry signal also confirmed the expression of mHexa, because these genes were linked by a fusion linker within the vector.

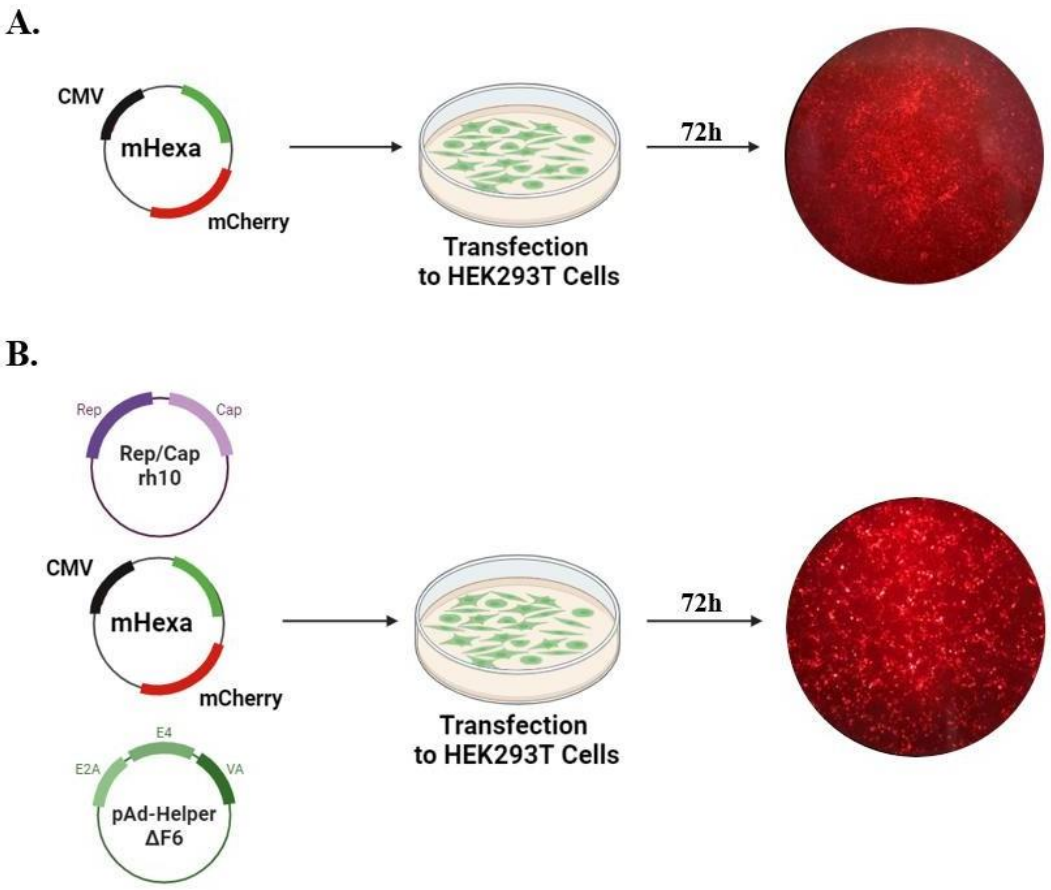

Figure 3.2. (A) Single transfection of mammalian expression vector encoding mHexa to HEK293Tcells. (B) Triple transfection of AAV2/rh10, mammalian expression vector encoding mHexa, AAVrh10 and pAdΔF6 plasmids to HEK293T cells. Images were taken at 20X magnification at 72 hours.

3.2. Transduction Test for AAVrh10-mHexa Virus Particles

The effectiveness of the AAVrh10-mHexa virus particles was evaluated through a transduction test on HEK293T cells and neuroglia cells isolated from the 20-weeks of age *Hexa-/-Neu3-/-* (DKO) mice. The multiplicity of infection (MOI) was set to 10,000 for HEK293T cells, and 500,000 for neuroglia due to the significantly higher transduction efficiency observed in HEK293T cells compared to neuroglia cells. The mCherry signal was captured at 7 days post-transduction (Figure 3.3). The mCherry signal intensity was much higher in HEK293T compared to neuroglia cells from the 20-weeks of age DKO mice (Figure 3.3). The presence of mCherry signal in both cell types confirms the successful transduction and effectiveness of produced AAVrh10-mHexa virus particles.

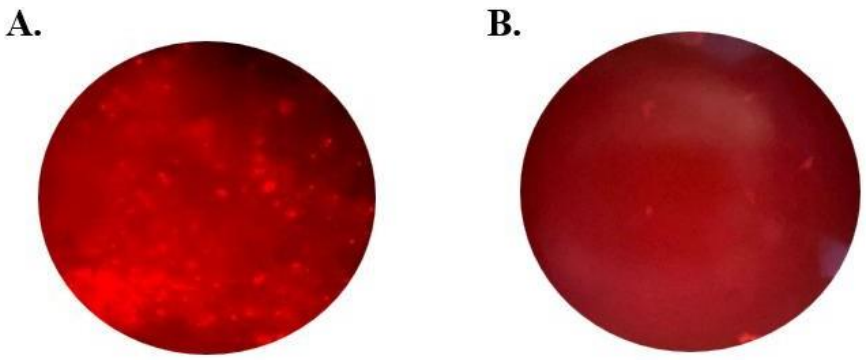

Figure 3.3. Transduction of AAVrh10-mHexa virions to HEK293T cells (A) and neuroglia cells (B) of 20-weeks of age *Hexa-/-Neu3-/-* (DKO) mice. Images were taken at 20X magnification at 7 days for HEK293T cells neuroglia cells of 20-weeks of age *Hexa-/-Neu3-/-* (DKO) mice .

3.3. anti-GM2 Staining for Transduced Neuroglia Cells

To evaluate the effect of AAVrh10-mHexa virus particles encoding mHexa on the GM2 ganglioside levels, anti-GM2 staining was performed on transduced neuroglia cells from 20-weeks of age DKO mice.

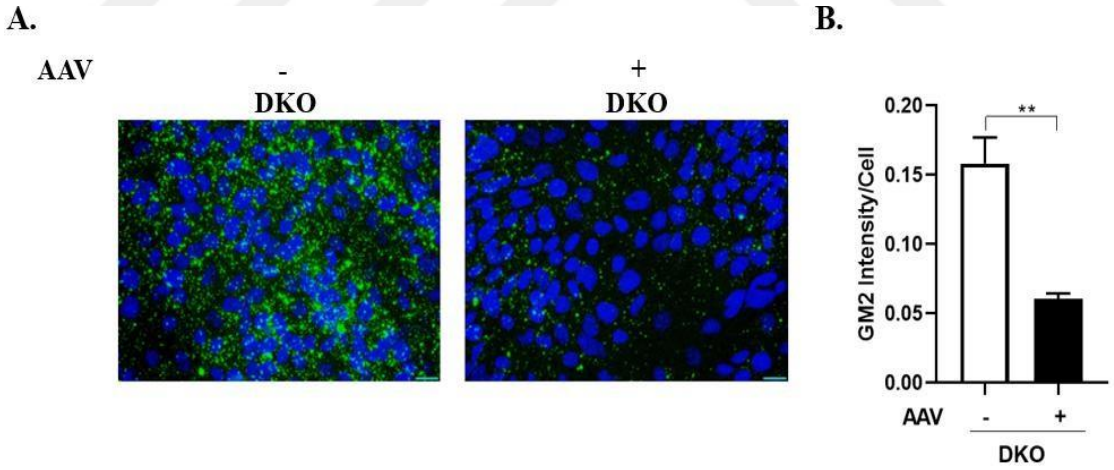

Figure 3.4. (A) Immunostaining of GM2 in AAV (AAVrh10-mHexa virus particle) transduced (+) and non-transduced (-) neuroglia cells of 20-weeks of age DKO mice (DKO; *Hexa-/-Neu3-/-*). Images were taken at 20X magnification under the same light intensity that differs filter types for DAPI and anti-KM966. Sections were stained with anti-KM966 antibody (green; GM2 marker) and DAPI (blue; nucleus). (B) Intensity of GM2 per cell was measured with ImageJ. One-way ANOVA analysis was used to determine *p*-values by using GraphPad. Data were reported as means ± SEM (n=3; $^{**}p < 0.025$).

The effect of AAV expressing mHexa on GM2 ganglioside was assessed *in vitro* using anti-GM2 staining. Non-transduced neuroglia cells from 20-weeks of age DKO mice exhibited the excessive accumulation levels of GM2 ganglioside due to the combined deficiency of *Hexa* and *Neu3* genes (Figure 3.4). In contrast, AAV-transduced neuroglia cells from DKO mice showed a reduction in the levels of GM2 ganglioside compared to non-transduced neuroglia cells (Figure 3.4). Anti-GM2 staining revealed the clearance of accumulated GM2 ganglioside with the AAV-transduced cells, and demonstrating the impact of AAV expressing mHexa in degrading GM2 ganglioside *in vitro*.

3.4. Genotyping of Mice for *Hexa* and *Neu3* Genes

The genotypes of mice for *Hexa* and *Neu3* genes were determined using PCR protocol. The specific primers that recognize the WT and KO (knock-out) alleles of *Hexa* and *Neu3* genes were used during the PCR protocols (Table 2.3).

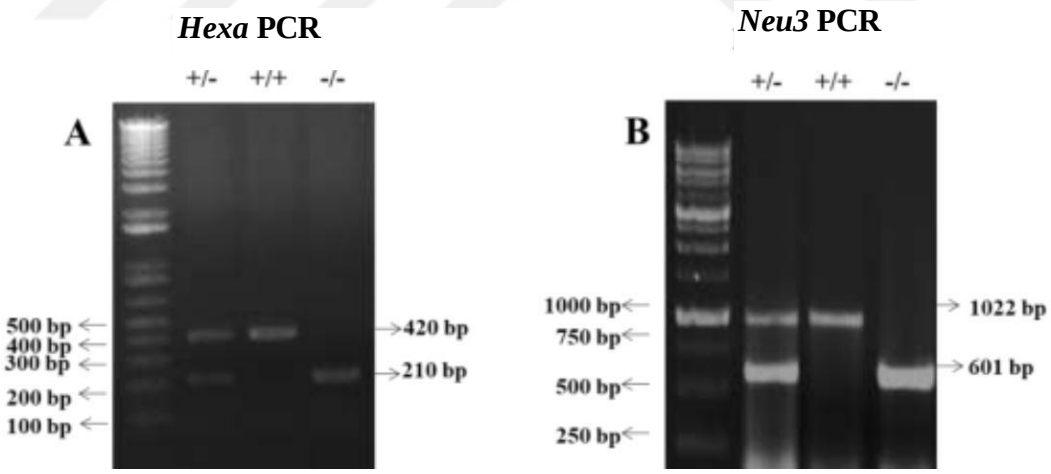

Figure 3.5. The agarose gel electrophoresis results of *Hexa* (A) and *Neu3* (B) PCR products.

HexaF, HexaR, and PGK primers were used for *Hexa* PCR. HexaF and HexaR recognize DNA segments with a size of 420 bp, while PGK and HexaR primers specifically bind to the KO allele with a size of 210 bp (Figure 3.5). In the same PRC

reaction, both WT and KO alleles were visualized using three primers designed for the *Hexa* gene.

Neu3 PCR reaction was performed using Neu3F, Neu3R, and NeoR primers. The WT allele of *Neu3* gene was recognized by Neu3F and Neu3R. Other primers including Neu3F and NeoR primers were also used to recognize and produce the KO allele of the *Neu3* gene (Figure 3.5). Both WT and KO alleles were produced in the same PCR reaction.

3.5. Body Weight Measurement

Body weight measurements were performed weekly to monitor the changes in the body weights of each mouse following AAVrh10-mHexa (AAV) and istradeylline administration. The intrathecal injection of AAVrh10-mHexa virus particles (AAV virions), which express mHexa, was administered to DKO mice at 8- weeks of age (Figure 3.6 A). In addition, intraperitoneal administration of istradefylline was performed at 10-weeks of age in DKO mice that had previously administered with AAV.

The body weight measurements indicated that DKO mice began to lose weight at 16 weeks, with a dramatic and rapid decline occurring thereafter (Figure 3.6 B). DKO mice also showed sudden death at 20-weeks of age. In contrast, DKO mice administered with AAV, or a combination of AAV and istradefylline, showed no significant changes in body weight compared to *WT* mice (Figure 3.6 B). To better visualize changes in the body weights, the body weights of each mouse were measured at 20 weeks, showing a significant reduction in the weight of DKO mice relative to *WT* controls (Figure 3.6 C). However, the administration of AVV, and AAV combined with istradefylline restored body weight in DKO mice compared to *WT* mice, with no notable differences between these groups. (Figure 3.6 C).

The Kaplan-Meier survival curve was used to assess lifespan across the different (Figure 3.6 D), there was sudden death at 20-weeks of age in DKO mice, whereas DKO mice administered with AAV, and AAV and istradefylline demonstrated an extended lifespan, surviving up to 30 weeks.

These findings revealed the effectiveness of AAV and AAV combined with istradefylline in both body weight and prolonging the lifespan of DKO mice.

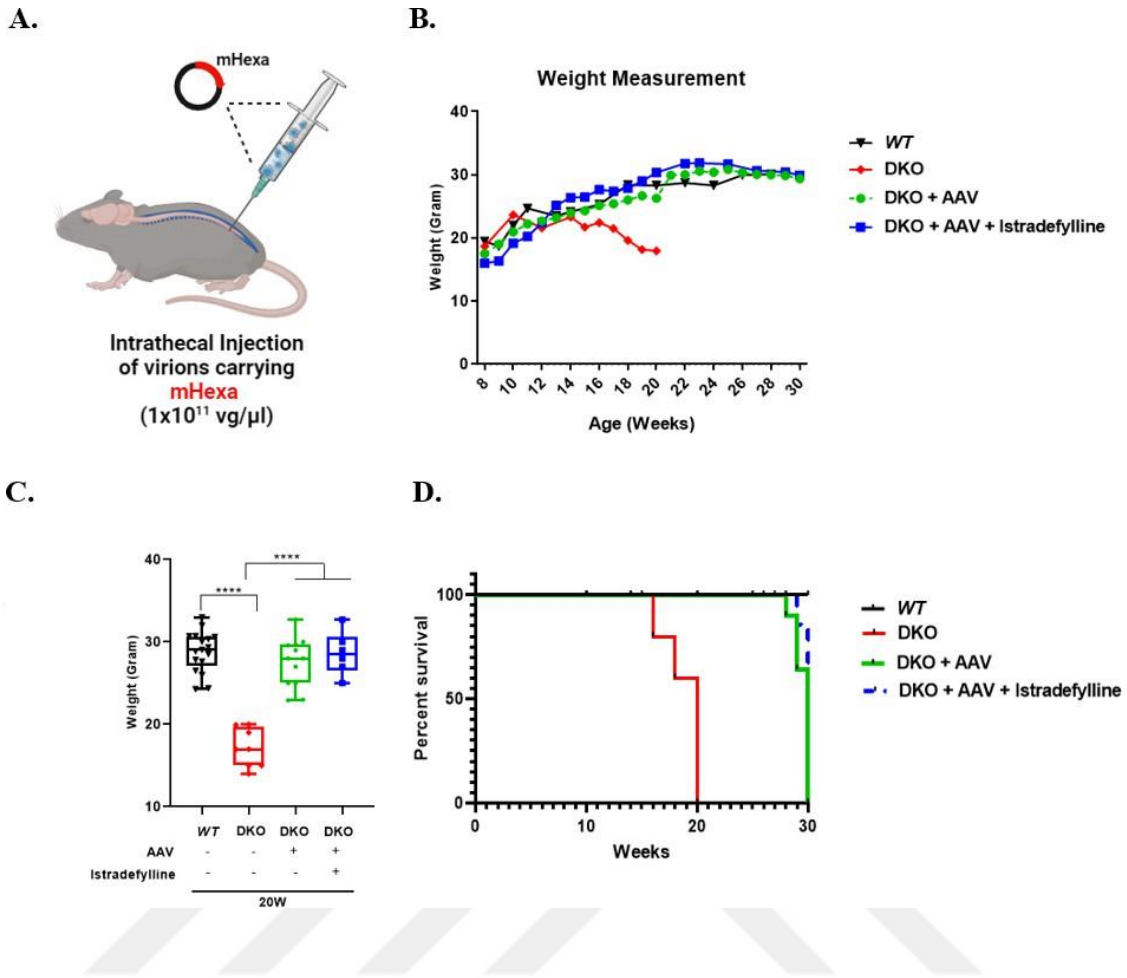

Figure 3.6. (A) Intrathecal injection of AAVrh10-mHexa virions to 8- weeks of age DKO mice. (B) Body weights of *WT* (n=8), DKO mice (n=8), DKO mice administered with AAV (n=6), DKO mice administered with AAV and istradefylline (n=6) (DKO; *Hexa-/-Neu3-/-*). Each point represents the average of representative mice of the corresponding genotype. (C) Body weights of 20- weeks of age *WT* (n=8), DKO mice (n=8), DKO mice administered with AAV (n=6), DKO mice administered with AAV and istradefylline (n=6). (D) Kaplan-Meier survival curve of *WT*, DKO mice, DKO mice administered with AAV, DKO mice administered with AAV and istradefylline.

3.6. Thin Layer Chromatography

Thin layer chromatography (TLC) analyses were performed to understand the effect of AAVrh10 expressing mHexa on the degradation of GM2 ganglioside in brain of DKO mice. GM2 ganglioside, an acidic ganglioside, was analyzed following the isolation of acidic gangliosides from the cortex of each mouse group.

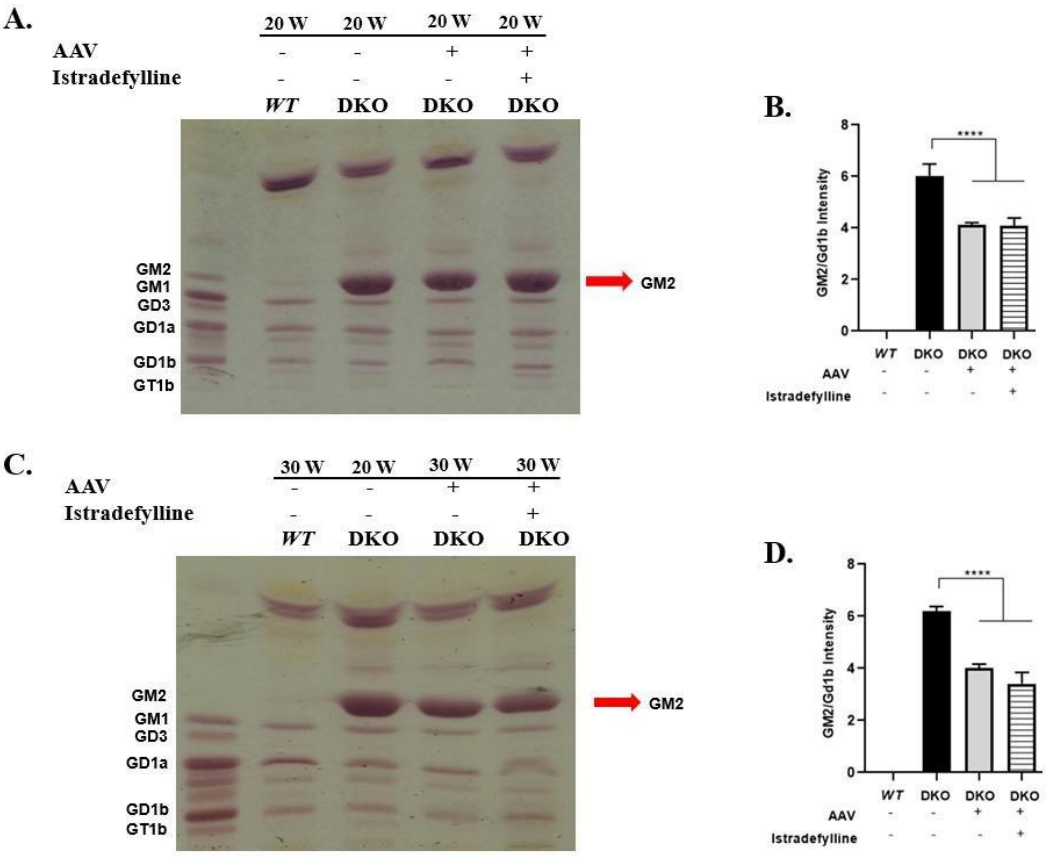

Figure 3.7. TLC analysis in the brain of 20- and 30- weeks of age *WT*, 20- weeks of age DKO mice, 20- and 30- weeks of age DKO mice administered with AAV, 20- and 30- weeks of age DKO mice administered with AAV and istradefylline (DKO; *Hexa-/-Neu3-/-*) (A, C). Intensity analyses for GM2 ganglioside was conducted using ImageJ program, and One-way ANOVA analysis was used to determine *p*-values by using GraphPad. Data were reported as means ± SEM (n=2; ****$p < 0.001$).

TLC analyses demonstrated excessive accumulation of GM2 ganglioside in the cortex of 20- weeks of age DKO mice, even though no accumulation of GM2 ganglioside was detected in *WT* mice at both 20 weeks and 30 weeks (Figure 3.7). The administration of either AAV alone, or combination with istradefylline resulted in significantly degradation of accumulating GM2 ganglioside in the cortex of DKO mice at both 20 (Figure 3.7 A and B) and 30 weeks of age (Figure 3.7 C and D), compared to non-treated DKO mice at 20 weeks, indicating the effectiveness of AAV-based gene therapy to degrade the GM2 ganglioside through expression of mHexa.

3.7. Hexa Expression Level and Enzyme Activity Assay

To assess the effects of AAV encoding mHexa, the expression level of mouse Hexa (mHexa) was analyzed using RT-PCR in the brain (cortex and cerebellum) and visceral organs (kidney, liver, spleen) of 20- and 30 weeks of age *WT* mice, 20- weeks of age DKO mice, 20- and 30- weeks of age DKO mice administered with AAV, 20- and 30- weeks of age DKO mice administered with AAV and istradefylline. Furthermore, the Hexa enzyme activity was measured using a Hexa-specific substrate in the brain (cortex and cerebellum), visceral organs (kidney, liver, spleen), and serum of these mice.

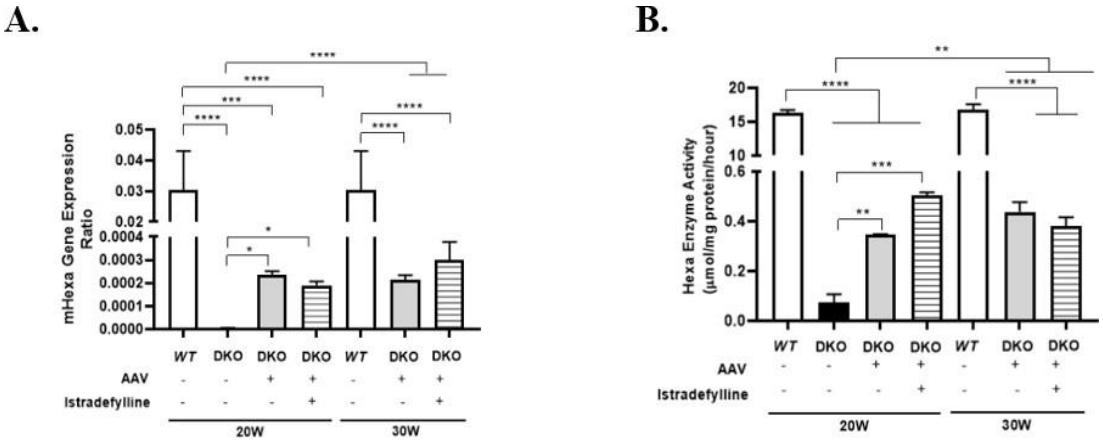

Figure 3.8. The expression ratio of mHexa (A) and Hexa Enzyme activity (B) in the cortex of 20- and 30- weeks of age *WT*, 20- weeks of age DKO mice, 20- and 30- weeks of age DKO mice administered with AAV, 20- and 30- weeks of age DKO mice administered with AAV and istradefylline (DKO; *Hexa-/-Neu3-/-*). Expression ratio was calculated with ΔCT method and One-way ANOVA analysis was used to determine *p*-values by using GraphPad. Data were reported as means ± SEM (n=3; **p* < 0.05, ***p* < 0.025, ****p* < 0.01, and *****p* < 0.001).

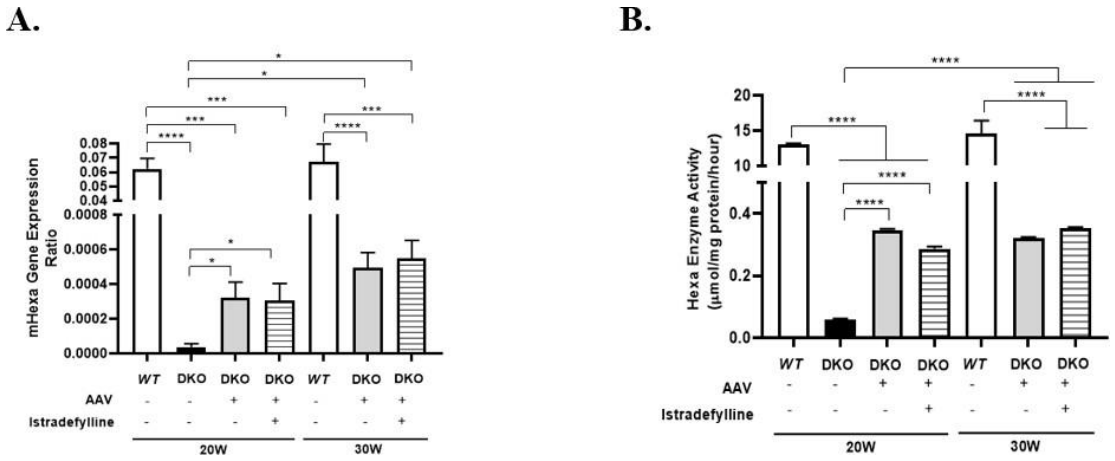

Figure 3.9. The expression ratio of mHexa (A) and Hexa Enzyme activity (B) in the cerebellum of 20- and 30- weeks of age *WT*, 20- weeks of age DKO mice, 20- and 30- weeks of age DKO mice administered with AAV, 20- and 30- weeks of age DKO mice administered with AAV and istradefylline (DKO; *Hexa-/-Neu3-/-*). Expression ratio was calculated with ΔCT method and One-way ANOVA analysis was used to determine *p*-values by using GraphPad. Data were reported as means ± SEM (n=3; **p* < 0.05, ***p* < 0.025, ****p* < 0.01, and *****p* < 0.001).

The analyses of mouse Hexa expression (mHexa) indicated that no expression of mHexa in the cortex and cerebellum of 20-weeks of age DKO mice, whereas the expression of mHexa was observed in the cortex and cerebellum of 20- and 30- weeks of aged *WT* mice. Although the expression levels of mHexa in the cortex and cerebellum of DKO mice administered with AAV, and AAV combined with istradefylline at 20 and 30 weeks were lower than in age-matched *WT* mice, there was a significant increase in mouse Hexa expression in the cortex and cerebellum of DKO mice administered with AAV, and AAV combined with istradefylline at 20 and 30 weeks compared to DKO mice at 20 weeks (Figure 3.8 A and Figure 3.9 A). These findings demonstrated the expression of mHexa in the cortex and cerebellum of DKO mice at both ages following successful administration of AAV encoding mHexa.

The Hexa enzyme activity level was determined in all groups of mice using enzyme activity assay. In the cortex and cerebellum of 20-weeks of age DKO mice, only residual Hexa activity was detected (Figure 3.8 B and Figure 3.9 B). In contrast, Hexa activity was present in 20- and 30- weeks of age *WT* mice. Furthermore, Hexa activity significantly increased in DKO mice administered with AAV, as well as in DKO mice administered with AVV and istradefylline, at 20 and 30 weeks compared to 20-weeks of

age DKO mice. However, this increase did not reach the levels observed in 20- and 30-weeks of age *WT* mice (Figure 3.8 B and Figure 3.9 B). These results showed that AAV administration enhances Hexa activity in the cortex and cerebellum of DKO mice, consistent with the analyses of mouse Hexa expression.

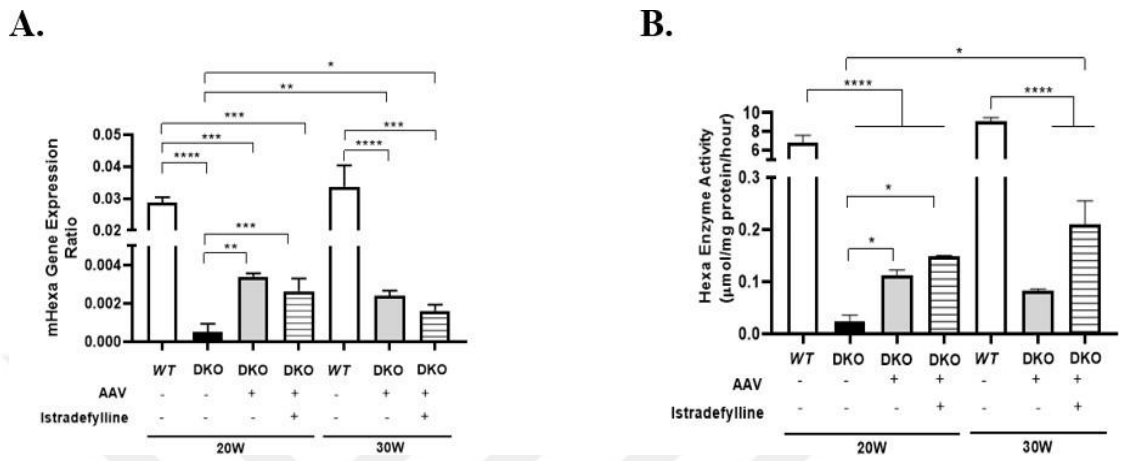

Figure 3.10. The expression ratio of mHexa (A) and Hexa Enzyme activity (B) in the kidney tissue of 20- and 30- weeks of age *WT*, 20- weeks of age DKO mice, 20- and 30- weeks of age DKO mice administered with AAV, 20- and 30-weeks of age DKO mice administered with AAV and istradefylline (DKO; *Hexa-/-Neu3-/-*). Expression ratio was calculated with ΔCT method and One-way ANOVA analysis was used to determine *p*-values by using GraphPad. Data were reported as means ± SEM (n=3; **p* < 0.05, ***p* < 0.025, ****p* < 0.01, and *****p* < 0.001).

In addition to the brain, visceral organs, including kidney, liver, and spleen, were analyzed using RT-PCR and enzyme activity assay to understand whether AAVdisplayed any tropism for these tissues.

In the kidney, both mouse Hexa expression and Hexa enzyme activity results showed consistent results. No mHexa expression and Hexa enzyme activity was observed in the kidneys of 20-weeks of age DKO mice (Figure 3.10 A and B). Both mouse Hexa expression and Hexa enzyme activity significantly increased in both 20- and 30- weeks of age DKO mice administered with AAV, and the combination of AAV and istradefylline (Figure 3.10 A and B). Despite this increase, mHexa expression and Hexa enzyme activity in these mice did not reach the levels seen in age-matched *WT* mice. These data exhibited the tropism of AAV for kidney tissue.

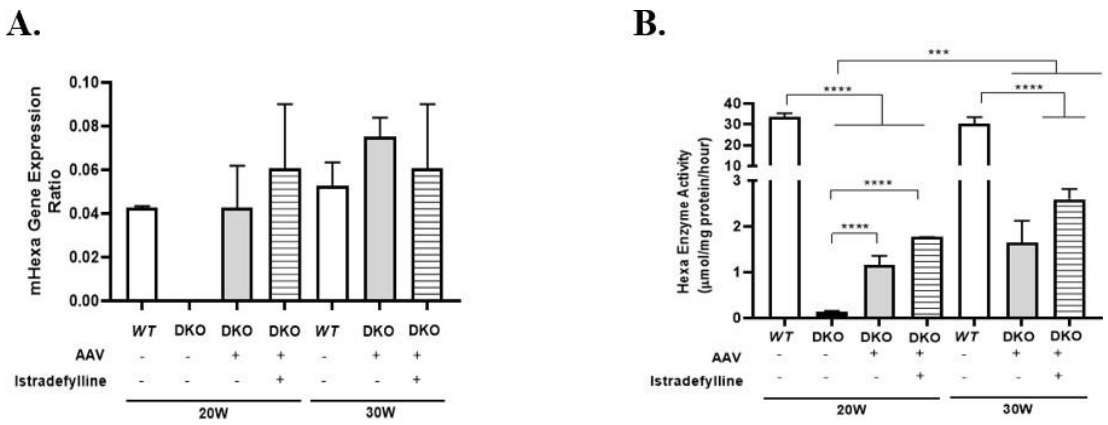

Figure 3.11. The expression ratio of mHexa (A) and Hexa Enzyme activity (B) in the liver tissue of 20- and 30- weeks of age *WT*, 20- weeks of age DKO mice, 20- and 30- weeks of age DKO mice administered with AAV, 20- and 30- weeks of age DKO mice administered with AAV and istradefylline (DKO; *Hexa-/-Neu3-/-*). Expression ratio was calculated with ΔCT method and One-way ANOVA analysis was used to determine *p*-values by using GraphPad. Data were reported as means ± SEM (n=3; **p* < 0.05, ***p* < 0.025, ****p* < 0.01, and *****p* < 0.001).

Mouse Hexa gene expression analyses in the liver revealed no detectable expression of mHexa in 20- weeks of age DKO mice (Figure 3.11 A). Although slight increased in mouse Hexa expression was measured in the livers of *WT* mice, as well as in DKO mice administered with AAV, and a combination of AAV and istradefylline at 20 and 30 weeks, this increase was not significant compared to 20- weeks of DKO mice (Figure 3.11 A). In the Hexa enzyme activity analysis, 20- and 30- weeks of age *WT* mice exhibited the expected levels of Hexa enzyme activity, however no Hexa activity was detected in 20- weeks of age DKO mice (Figure 3.11 B). The administration of AAV alone and in combination with istradefylline in DKO mice resulted in elevated Hexa enzyme activity at both 20 and 30 weeks compared to 20- weeks of age in DKO mice (Figure 3.11 B). This observation also showed the tropism of AAV in liver tissue.

As a visceral organ, the spleen was analyzed using RT-PCR and enzyme activity assay. The tropism of AAV for this tissue was confirmed by observing the elevated mHexa expression and Hexa enzyme activity in DKO mice following the administration of AAV alone, and combination of AAV with istradefylline at 20 weeks compared to 20- weeks of age DKO mice (Figure 3.12).

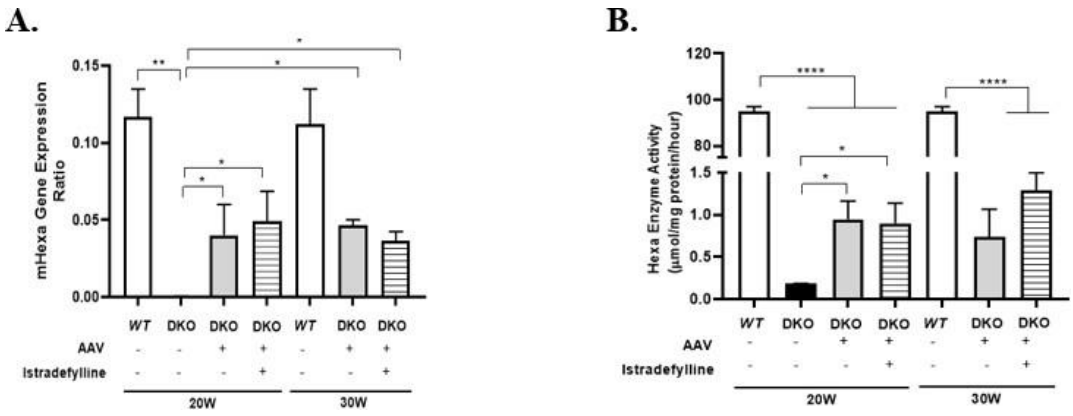

Figure 3.12. The expression ratio of mHexa (A) and Hexa Enzyme activity (B) in the spleen tissue of 20- and 30- weeks of age *WT*, 20- weeks of age DKO mice, 20- and 30- weeks of age DKO mice administered with AAV, 20- and 30- weeks of age DKO mice administered with AAV and istradefylline (DKO; *Hexa-/-Neu3-/-*). Expression ratio was calculated with ΔCT method and One-way ANOVA analysis was used to determine *p*-values by using GraphPad. Data were reported as means ± SEM (n=3; **p* < 0.05, ***p* < 0.025, ****p* < 0.01, and *****p* < 0.001).

Hexa enzyme activity was assessed in the serum of each mouse group to evaluate the circulation of AAV in the bloodstream. Residual Hexa enzyme activity was noted in 20- weeks of age DKO mice (Figure 3.13). Restored Hexa activity was shown in 20- weeks of age DKO mice administered with AAV and istradeylline, as well as in 30- weeks of age DKO mice administered with AAV alone, and combination of AVV with istradeylline, compared to 20- weeks of age DKO mice (Figure 3.X). Even though Hexa enzyme activity increased with the administration AAV, and combination of AAV and istradefylline in DKO mice, this elevation did not reach the Hexa activity levels of 20- and 30- weeks of age *WT* mice (Figure 3.13).

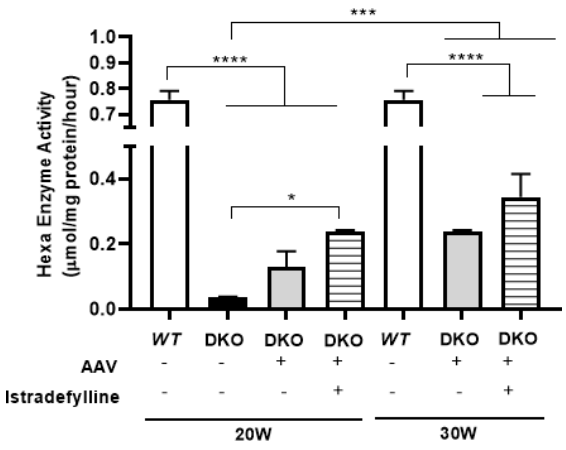

Figure 3.13. Hexa Enzyme activity in the serum of 20- and 30- weeks of age *WT*, 20-weeks of age DKO mice, 20- and 30- weeks of age DKO mice administered with AAV, 20- and 30- weeks of age DKO mice administered with AAV and istradefylline (DKO; *Hexa-/-Neu3-/-*). One-way ANOVA analysis was used to determine *p*-values by using GraphPad. Data were reported as means ± SEM (n=3; **p* < 0.05, ***p* < 0.025, ****p* < 0.01, and *****p* < 0.001).

3.8. Real-Time PCR (RT-PCR)

The gene expression levels of inflammation-related and lysosome-related markers were determined using RT-PCR analyses. In the brain sections (cortex and cerebellum) of each mice group, the gene expression ratios of neuroinflammatory-related markers such as CCL2, CCL3, CCL5, Cxcl10, IL1-β, Iba1, and GFAP were determined. The expression levels of inflammatory-related markers including CCL2, CCL3, CCL5, Cxcl10, and IL1-β were evaluated for visceral organs, kidney, liver, and spleen. Furthermore, the expression level of the lysosome-related marker, Lamp-1, was also analyzed for both the brain and visceral organs of each mouse group.

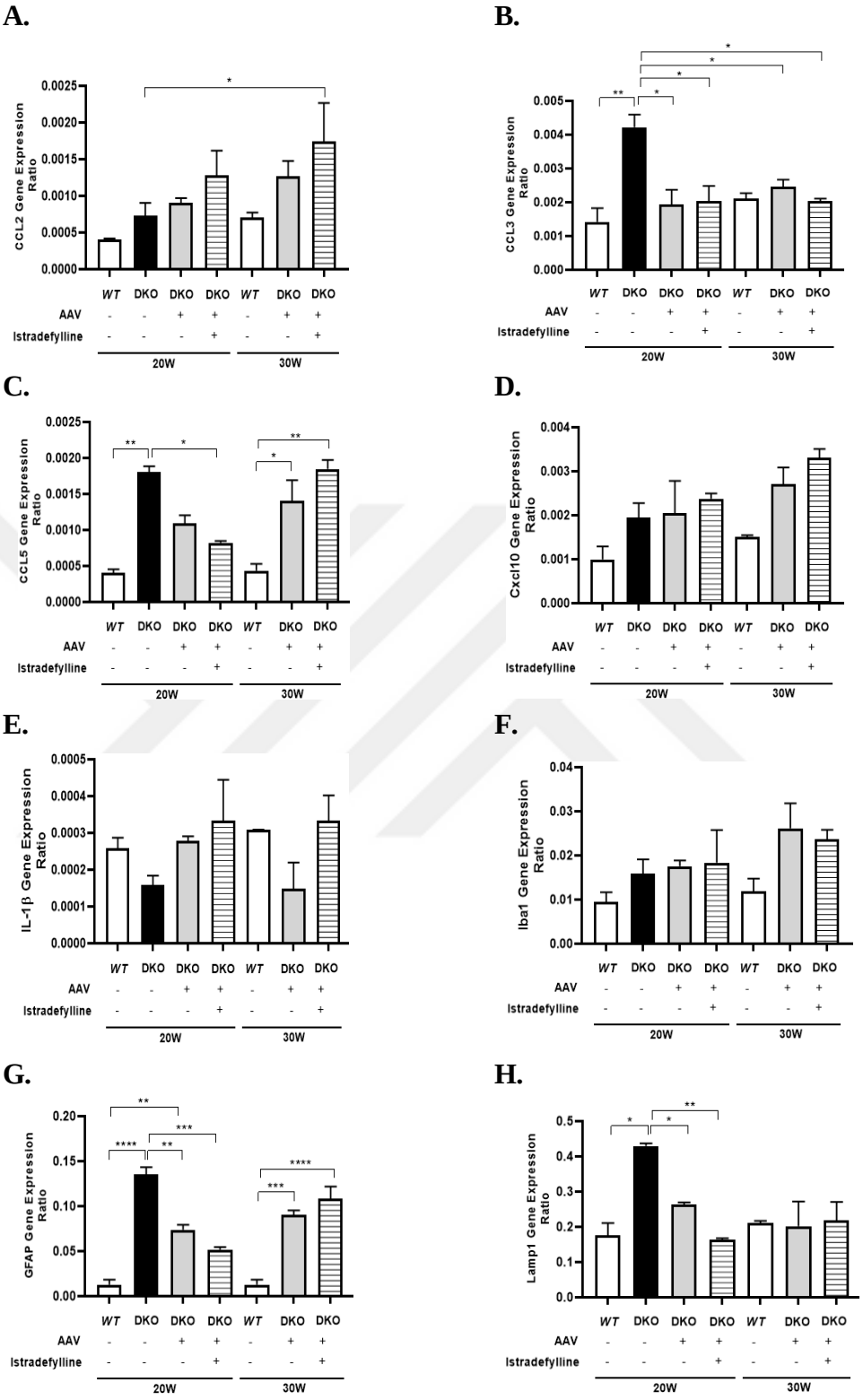

Figure 3.14. The expression ratios of neuroinflammation-related CCL2 (A), CCL3 (B), CCL5 (C), Cxcl10 (D), IL-1β (E), Iba1 (F), GFAP (G), and lysosome-related Lamp1 (H) in the cortex of 20- and 30- weeks of age *WT*, 20- weeks of age DKO mice, 20- and 30- weeks of age DKO mice administered with AAV, 20- and 30- weeks of age DKO mice administered with AAV and

istradefylline (DKO; *Hexa-/-Neu3-/-*). Expression ratios were calculated with ΔCT method and One-way ANOVA analysis was used to determine *p*-values by using GraphPad. Data were reported as means ± SEM (n=3; **p* < 0.05, ***p* < 0.025, ****p* < 0.01, and *****p* < 0.001).

In the neuroinflammatory-related markers analyzed in the cortex tissue, elevated expression levels of CCL3, CCL5 and GFAP were shown in the 20- weeks of age DKO mice compared to age-matched *WT* mice (Figure 3.14 B, Figure 3.14 C, and Figure 3.14 G). Although other neuroinflammatory markers, including CCL2, Cxcl10, and Iba1 showed a slight increase in 20- weeks of age DKO mice compared to 20- weeks of age *WT* mice, these increases were not statistically significant (Figure 3.14 A, Figure 3.14 D, and Figure 3.14 F). No significant changes were detected for these markers across the different mouse groups (Figure 3.14 A, Figure 3.14 D, and Figure 3.14 F). Besides, IL-1β did not show significant differences in expression levels among mouse groups (Figure 3.X F).

The expression ratio of CCL3 reduced in the cortex of 20- and 30- weeks of age DKO mice administered with AAV, and a combination of AAV and istradefylline compared to 20- weeks of age DKO mice (Figure 3.14 B). A reduced expression of CCL5 was also noted in the cortex of DKO mice administered with AAV and istradefylline compared to DKO mice at 20 weeks (Figure 3.14 C). Furthermore, a lower expression level of GFAP was observed in 20- weeks of age DKO mice administered with AAV alone, and in combination with istradefylline compared to 20- weeks of age DKO mice (Figure 3.14 G). However, this reduced level of GFAP was not detected in the cortex of 30- weeks of age DKO mice administered with AAV, and with a combination of AAV and istradefylline, compared to 20- weeks of age DKO mice (Figure 3.14 G).

Lamp1, a lysosome-marker, was analyzed in the cortex of the mouse groups. Higher levels of Lamp1, indicating an increase in lysosomes, were demonstrated in the cortex of DKO mice compared to *WT* mice at 20 weeks (Figure 3.14 H). The accumulated lysosomes were reduced in DKO mice after administration of AAV alone, and in combination with istradefylline, at 20 weeks compared to age-matched DKO mice.

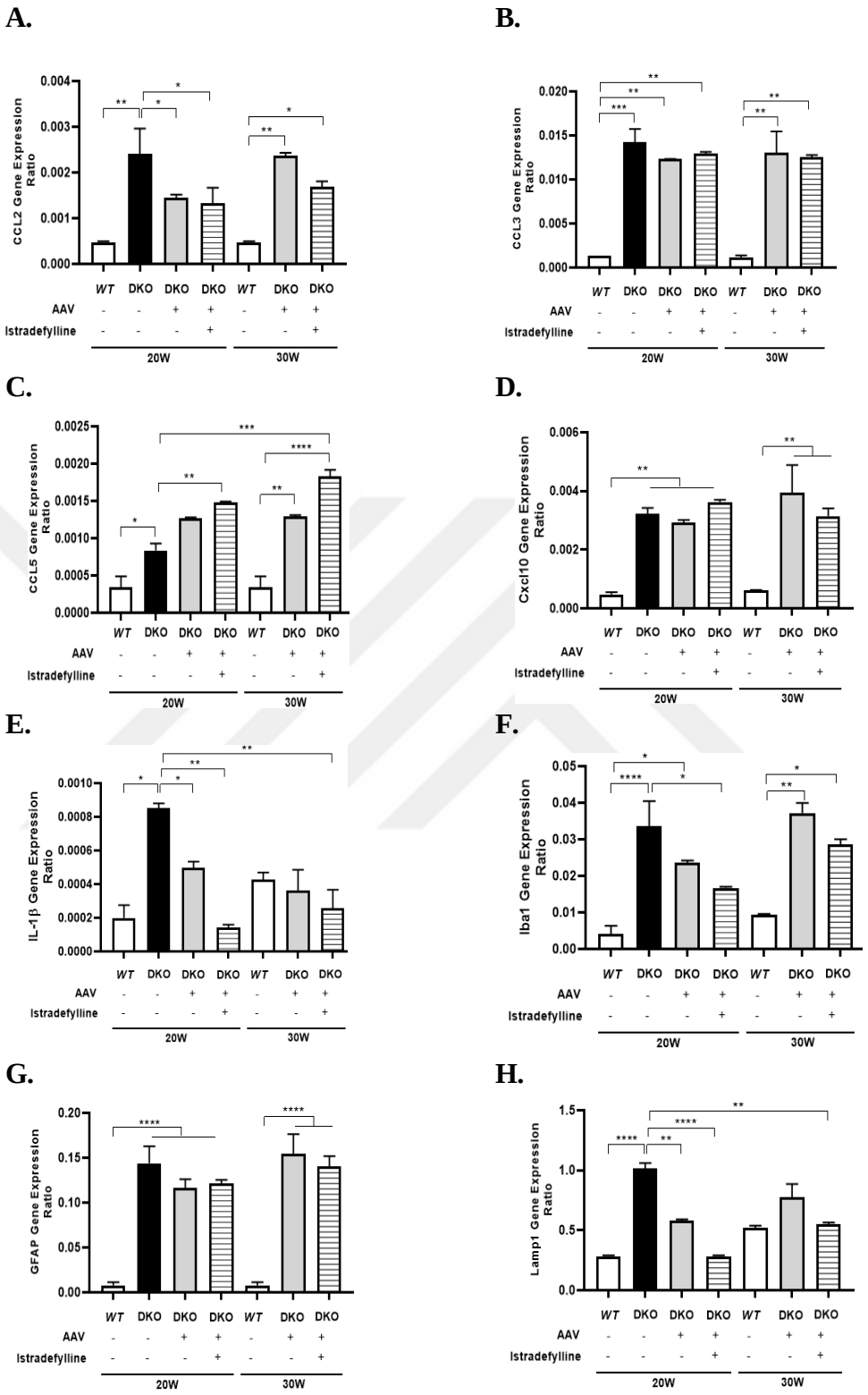

Figure 3.15. The expression ratios of neuroinflammation-related CCL2 (A), CCL3 (B), CCL5 (C), Cxcl10 (D), IL-1β (E), Iba1 (F), GFAP (G), and lysosome-related Lamp1 (H) in the cerebellum tissue of 20- and 30- weeks of age *WT*, 20-weeks of age DKO mice, 20- and 30- weeks of age DKO mice administered with AAV, 20- and 30- weeks of age DKO mice administered with AAV and istradefylline (DKO; *Hexa-/-Neu3-/-*). Expression ratios were calculated

with ΔCT method and One-way ANOVA analysis was used to determine *p*-values by using GraphPad. Data were reported as means ± SEM (n=3; **p* < 0.05, ***p* < 0.025, ****p* < 0.01, and *****p* < 0.001).

The expression of neuroinflammatory markers, including elevated levels of CCL2, CCL3, CCL5, Cxcl10, IL-1β, Iba1, and GFAP, was observed in the cerebellum of 20- weeks of age DKO mice compared to 20- weeks of age *WT* mice (Figure 3.15). Higher expression levels of CCL3, Cxcl10 and GFAP were also shown in the cerebellum of 20- and 30- weeks of age DKO mice administered with AAV, and a combination of AAV and istradefylline, compared to age-matched *WT* controls (Figure 3.15 B, Figure 3.15 D, and Figure 3.15 G). A significantly increased level of CCL5 was also observed in DKO mice administered with AAV, as well as in DKO mice administered with a combination of AAV and istradefylline, compared to *WT* mice at 30 weeks (Figure 3.15 C).

The expression levels of CCL5 and Iba1 were higher in the cerebellum of DKO mice after the administration of AAV alone and in a combination with istradefylline, compared to *WT* mice at 30 weeks (Figure 3.15 A and Figure 3.15 F). On the other hand, the expression levels of CCL2, IL-1β, and Iba1 significantly decreased in the cerebellum of DKO mice following the administration of AAV alone, and a combination of AAV with istradefylline, compared to 20- weeks of age DKO mice (Figure 3.15 A, Figure 3.15 E, and Figure 3.15 F).

The expression ratio of Lamp1 was also analyzed to evaluate changes in lysosomal accumulation in the cerebellum of DKO mice after the administration of AAV, and AAV with istradefylline. A significantly increased expression level of Lamp1 was observed in DKO mice compared to *WT* mice at 20 weeks (Figure 3.15 H). Administration of AAV alone and in combination with istradefylline, in DKO mice indicated the lysosomal degradation in the cerebellum at 20 and 30 weeks, compared to 20-weeks of age DKO mice (Figure 3.15 H).

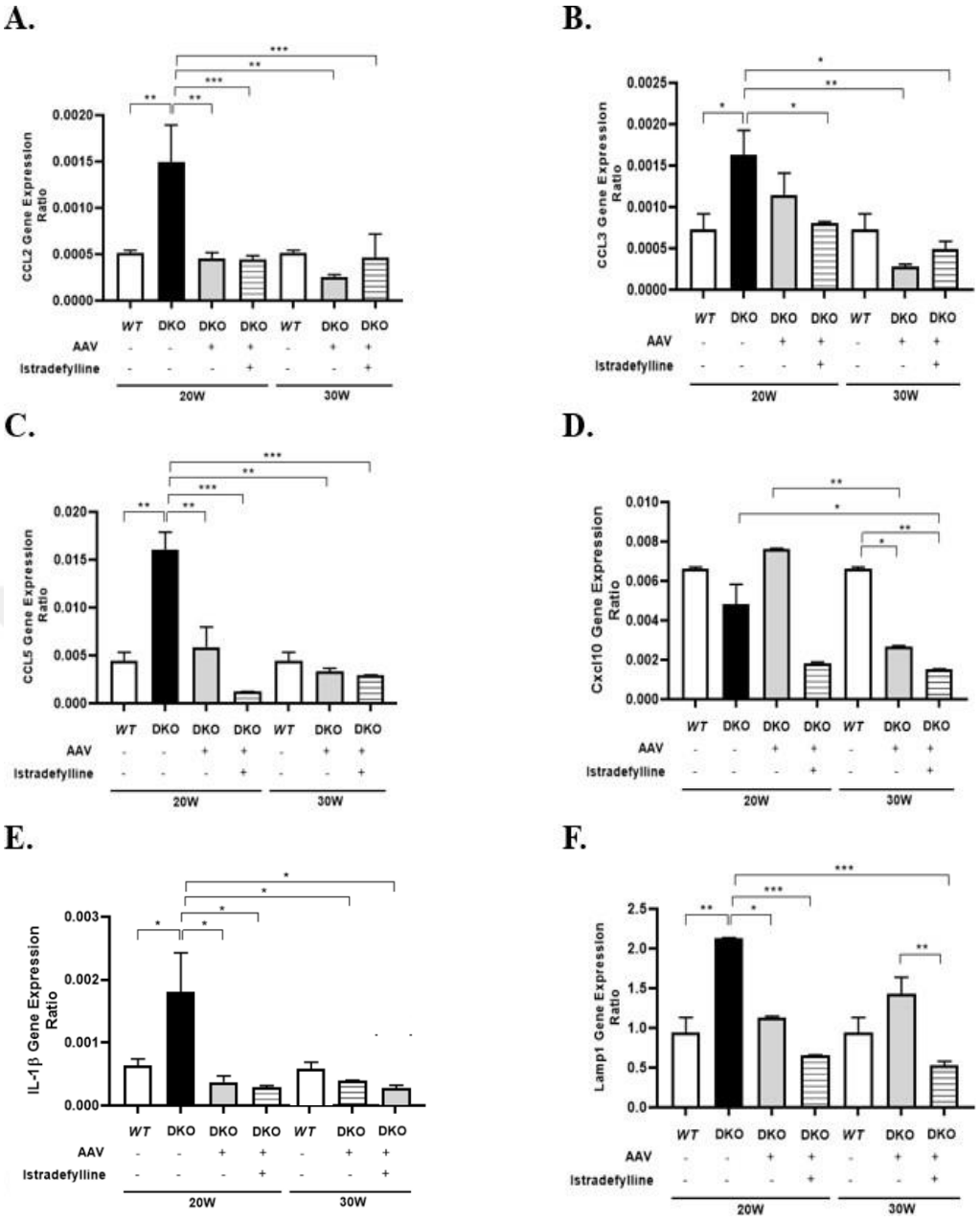

Figure 3.16. The expression ratios of inflammation-related CCL2 (A), CCL3 (B), CCL5 (C), Cxcl10 (D), IL-1β (E), and lysosome-related Lamp1 (F) in the kidney tissue of 20- and 30- weeks of age *WT*, 20- weeks of age DKO mice, 20- and 30- weeks of age DKO mice administered with AAV, 20- and 30- weeks of age DKO mice administered with AAV and istradefylline (DKO; *Hexa-/-Neu3-/-*). Expression ratios were calculated with ΔCT method and One-way ANOVA analysis was used to determine *p*-values by using GraphPad. Data were reported as means ± SEM (n=3; **p* < 0.05, ***p* < 0.025, ****p* < 0.01, and *****p* < 0.001).

In addition to the brain, other visceral organs were analyzed for inflammatory markers, including CCL2, CCL3, CCL5, Cxcl10, and IL-1β, using RT-PCR. In the kidneys of 20- weeks of age DKO mice, the expression levels of CCL2, CCL3, CCL5, and IL-1β were significantly increased compared to 20- weeks of age *WT* mice (Figure 3.16 A, Figure 3.16 B, Figure 3.16 C, and Figure 3.16 E). The expression levels of these inflammatory markers were reduced after the administration of AAV alone, and in combination with istradefylline, in DKO mice at 20 and 30 weeks, compared to 20- weeks of age DKO mice (Figure 3.16 A, Figure 3.16 B, Figure 3.16 C, and Figure 3.16 E).

Although the expression level of Cxcl10 did not show significant changes among mouse groups at 20 weeks, its expression ratio in kidneys was lower in DKO mice administered with AAV, and in combination with AAV and istradefylline, compared to *WT* mice at 30 weeks (Figure 3.16 D).

A higher expression level of Lamp1 was also shown in the kidneys of DKO mice compared to *WT* mice at 20 weeks (Figure 3.16 F). Additionally, lysosomal degradation was indicated in DKO mice after the combined administration of AAV and istradefylline at both 20 and 30 weeks, compared to 20- weeks of age DKO mice (Figure 3.16 F).

In the liver tissue, significantly increased expression levels of CCL2, CCL3, and CCL5 were observed in DKO mice compared to *WT* mice at 20 weeks (Figure 3.16 A, Figure 3.16 B, and Figure 3.16 C). In the livers of 20- weeks of age DKO mice administered with AAV, elevated expression levels of CCL2 were determined compared to 20- weeks of age *WT* mice (Figure 3.16 A). However, the combined administration of AAV and istradefylline in DKO mice showed a decreased expression level of CCL2 compared to DKO mice administered with AAV alone at 20 weeks (Figure 3.16 A).

Both CCL3 and CCL5 inflammatory markers significantly increased in the livers of DKO mice after administration of AAV alone, and in combination with AAV and istradefylline, at 20 and 30 weeks, compared to age-matched *WT* controls (Figure 3.16 B and Figure 3.16 C. Regarding CCL3 expression in the liver, reduced levels were detected in DKO mice administered with AAV, and in combination with AAV and istradefylline, at 20 and 30 weeks, compared to DKO mice at 20 weeks (Figure 3.16 B). The same pattern was observed for CCL5 gene expression in the liver of DKO mice administered with AAV, and in combination with AAV and istradefylline, compared to 20- weeks of age DKO mice (Figure 3.16 C).

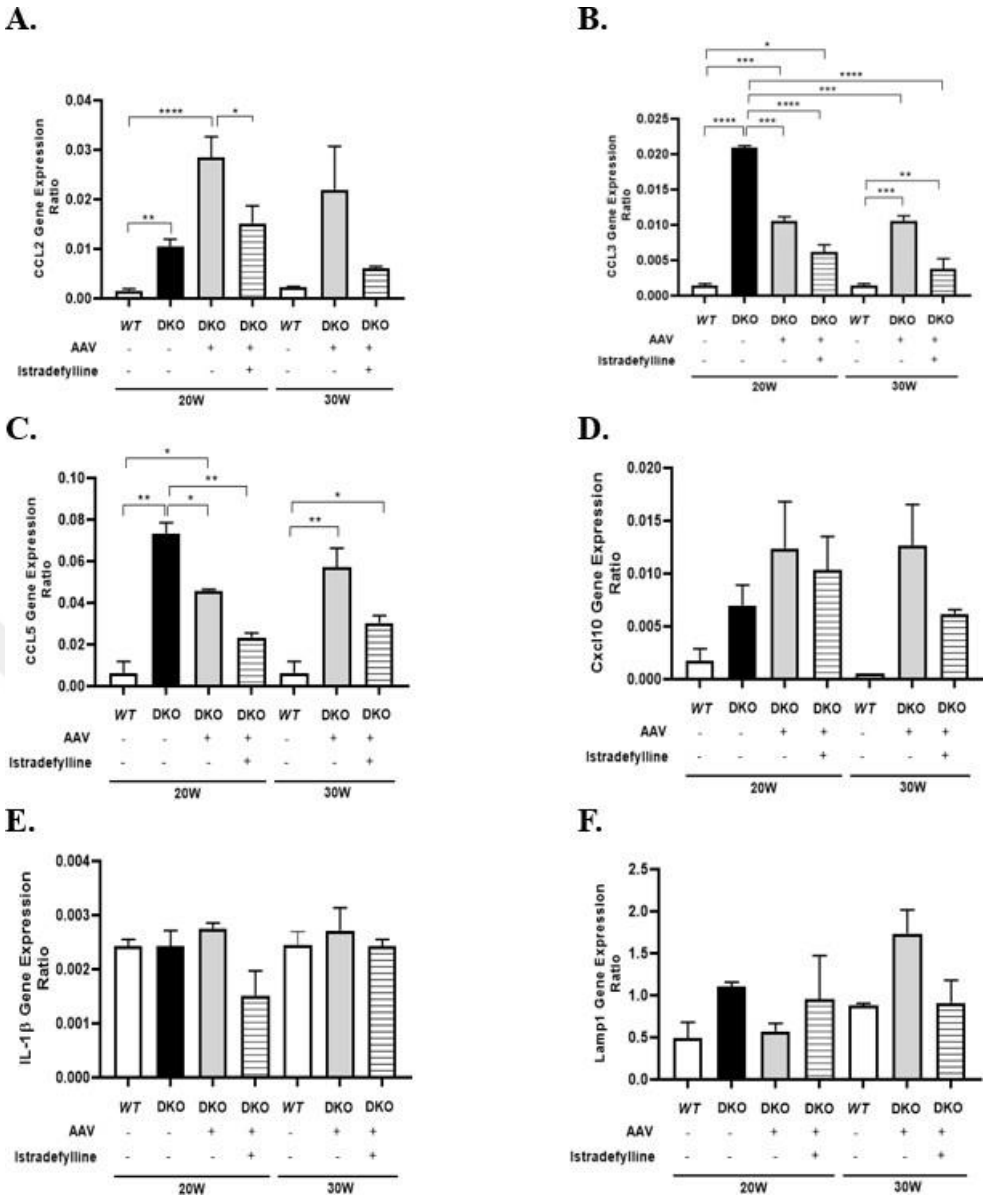

Figure 3.17. The expression ratios of inflammation-related CCL2 (A), CCL3 (B), CCL5 (C), Cxcl10 (D), IL-1β (E), and lysosome-related Lamp1 (F) in the liver tissue of 20- and 30- weeks of age *WT*, 20- weeks of age DKO mice, 20- and 30- weeks of age DKO mice administered with AAV, 20- and 30- weeks of age DKO mice administered with AAV and istradefylline (DKO; *Hexa-/-Neu3-/-*). Expression ratios were calculated with ΔCT method and One-way ANOVA analysis was used to determine *p*-values by using GraphPad. Data were reported as means ± SEM (n=3; **p* < 0.05, ***p* < 0.025, ****p* < 0.01, and *****p* < 0.001).

No significant changes were observed for inflammatory markers, including Cxcl10 and IL-1β, in the livers of distinct mouse groups (Figure 3.17 D and Figure 3.17 E). The lysosome marker Lamp1 was also analyzed in the livers of mouse groups.

Although slightly increased expression levels were detected in DKO mice compared to *WT* mice at 20 weeks, this increase was not significant (Figure 3.17 F). Additionally, no significant changes in Lamp1 expression levels were observed among DKO mice groups (Figure 3.17 F).

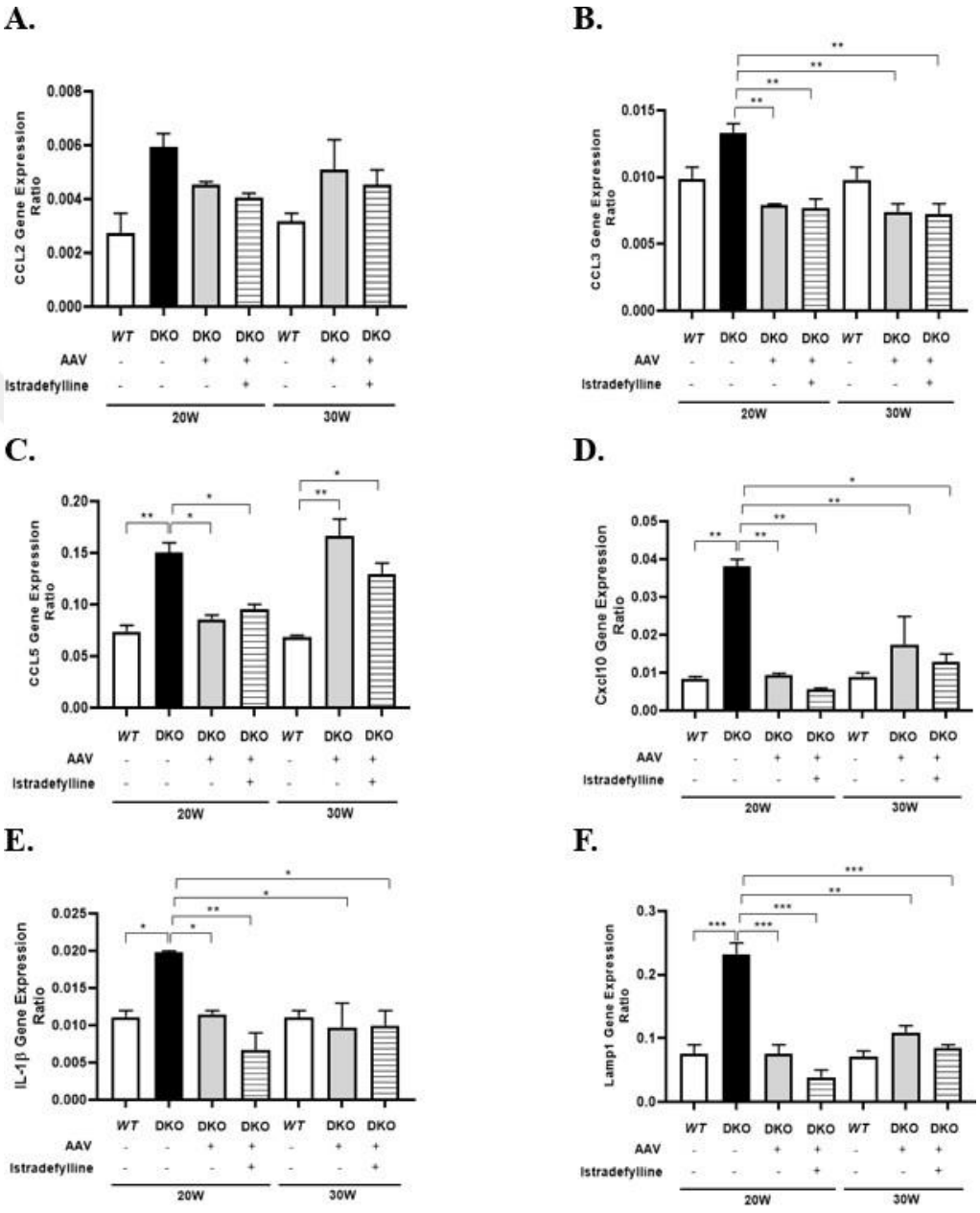

Figure 3.18. The expression ratios of inflammation-related CCL2 (A), CCL3 (B), CCL5 (C), Cxcl10 (D), IL-1β (E), and lysosome-related Lamp1 (F) in the spleen tissue of 20- and 30- weeks of age *WT*, 20- weeks of age DKO mice, 20- and 30- weeks of age DKO mice administered with AAV, 20- and 30- weeks of age DKO mice administered with AAV and istradefylline (DKO; *Hexa-/-Neu3-/-*). Expression ratios were calculated with ΔCT method and One-way ANOVA analysis was used to determine *p*-values by using GraphPad. Data were reported as means ± SEM (n=3; **p* < 0.05, ***p* < 0.025, ****p* < 0.01, and *****p* < 0.001).

In the spleen, no significant changes were observed in the expression levels of CCL2 and CCL3 in DKO mice relative to *WT* mice at 20 weeks, although there were slight increases in these markers in DKO mice (Figure 3.18 A and Figure 3.18 B). The expression levels of CCL5, Cxcl10, and GFAP were significantly higher in the spleen of 20- weeks of age DKO mice compared to age-matched *WT* mice (Figure 3.18 C, Figure 3.18 D, Figure 3.18 E).

The administration of AAV alone, and in combination with istradefylline, in the spleens of DKO mice resulted in lower expression of inflammatory-related genes, including CCL3, Cxcl10, and IL-1β, at 20 and 30 weeks compared to DKO mice (Figure 3.18 B, Figure 3.18 D , and Figure 3.18 E). Furthermore, another inflammatory-related marker, CCL5, also showed reduced expression levels in the spleens of DKO mice administered with AAV, and in a combination with AAV and istradefylline at 20 and 30 weeks, compared to DKO mice at 20 weeks (Figure 3.18 C).

The lysosome level was determined using specific primers that recognize Lamp1 in the spleens of the mouse groups. Elevated expression level of Lamp1 was noted in the spleens of 20- weeks of age DKO mice compared to age-matched *WT* mice (Figure 3.18 F). Additionally, the lower Lamp1 expression was observed in the spleens of DKO mice administered with AAV, and in combination with AAV and istradefylline, at 20 and 30 weeks compared to DKO mice at 20 weeks (Figure 3.18 F).

3.9. Western Blot

Western Blot analyses were performed to understand how the gene expression ratios of IL-1β, NF-κB, and IκB-α changes on the protein level depending on the AAV administration alone, and in combination with AAV and istradefylline. The brain (cortex and cerebellum) and visceral organs (kidney, liver, spleen) of 20- and 30 weeks of age *WT*, 20- weeks of age DKO mice, 20- and 30- weeks of age DKO mice administered with AAV, 20- and 30- weeks of age DKO mice administered with AAV and istradefylline were used in Western Blot analyses.

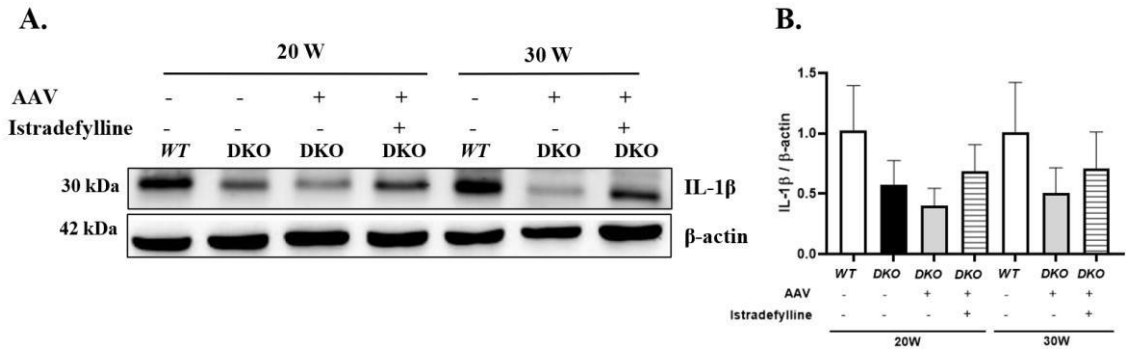

Figure 3.19. Immunoblot image (A) and densitometric analysis of IL-1β (B) in cortex tissue of 20- and 30- weeks of age *WT*, 20- weeks of age DKO mice, 20- and 30- weeks of age DKO mice administered with AAV, 20- and 30- weeks of age DKO mice administered with AAV and istradefylline (DKO; *Hexa-/-Neu3-/-*). β-actin was an internal control. Each band's intensity was detected using ImageJ and normalized to β-actin intensity. One-way ANOVA analysis was used to determine *p*-values by using GraphPad. Data were reported as means ± SEM (n=3).

IL-1β expression level did not differ significantly among the mouse groups based on genotype and age in the cortex (Figure 3.19).

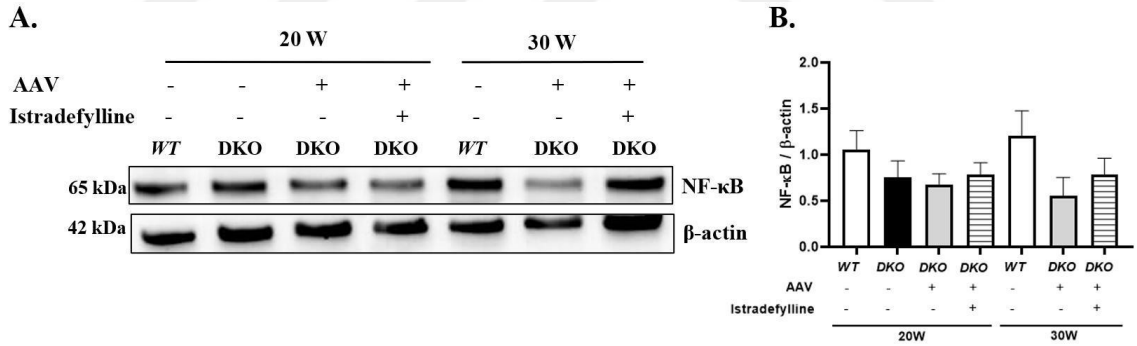

Figure 3.20. Immunoblot image (A) and densitometric analysis of NF-κB (B) in cortex tissue of 20- and 30- weeks of age *WT*, 20- weeks of age DKO mice, 20- and 30- weeks of age DKO mice administered with AAV, 20- and 30- weeks of age DKO mice administered with AAV and istradefylline (DKO; *Hexa-/-Neu3-/-*). β-actin was an internal control. Each band's intensity was detected using ImageJ and normalized to β-actin intensity. One-way ANOVA analysis was used to determine *p*-values by using GraphPad. Data were reported as means ± SEM (n=3).

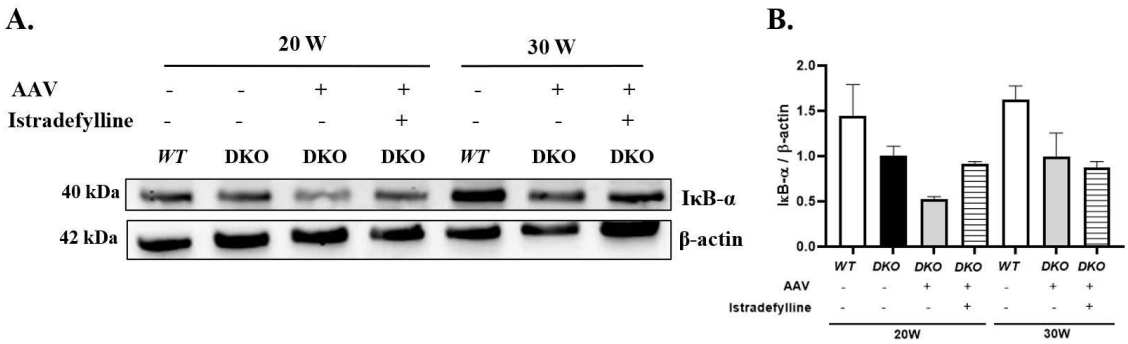

Figure 3.21. Immunoblot image (A) and densitometric analysis of IκB-α (B) in cortex tissue of 20- and 30- weeks of age *WT*, 20- weeks of age DKO mice, 20- and 30- weeks of age DKO mice administered with AAV, 20- and 30- weeks of age DKO mice administered with AAV and istradefylline (DKO; *Hexa-/-Neu3-/-*). β-actin was an internal control. Each band's intensity was detected using ImageJ and normalized to β-actin intensity. One-way ANOVA analysis was used to determine *p*-values by using GraphPad. Data were reported as means ± SEM (n=3).

In the cortex, the inflammation-related markers, including NF-κB and IκB-α, did not exhibit statistically significant changes among the mouse groups at both 20 weeks and 30 weeks (Figure 3.20 and Figure 3.21).

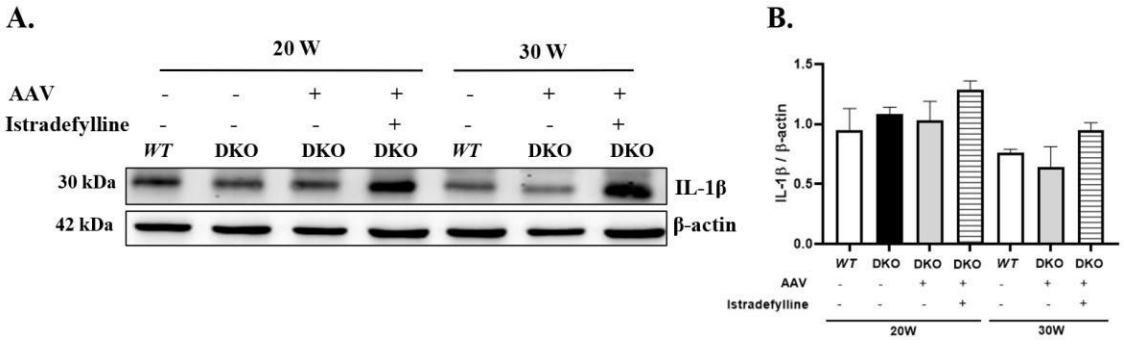

Figure 3.22. Immunoblot image (A) and densitometric analysis of IL-1β (B) in cerebellum tissue of 20- and 30- weeks of age *WT*, 20- weeks of age DKO mice, 20- and 30- weeks of age DKO mice administered with AAV, 20- and 30- weeks of age DKO mice administered with AAV and istradefylline (DKO; *Hexa-/-Neu3-/-*). β-actin was an internal control. Each band's intensity was detected using ImageJ and normalized to β-actin intensity. One-way ANOVA analysis was used to determine *p*-values by using GraphPad. Data were reported as means ± SEM (n=3).

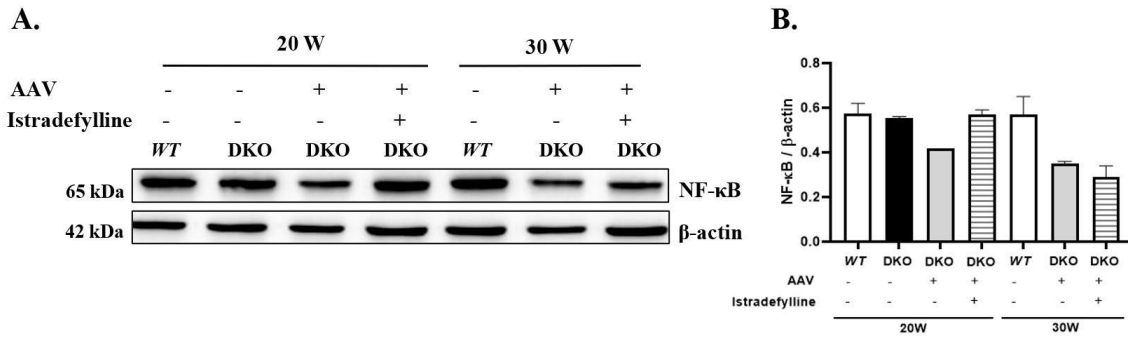

Figure 3.23. Immunoblot image (A) and densitometric analysis of NF-κB (B) in cerebellum tissue of 20- and 30- weeks of age *WT*, 20- weeks of age DKO mice, 20- and 30- weeks of age DKO mice administered with AAV, 20- and 30- weeks of age DKO mice administered with AAV and istradefylline (DKO; *Hexa-/-Neu3-/-*). β-actin was an internal control. Each band's intensity was detected using ImageJ and normalized to β-actin intensity. One-way ANOVA analysis was used to determine *p*-values by using GraphPad. Data were reported as means ± SEM (n=3).

In Figure 3.22 and Figure 3.23, no obvious changes were observed in the expression levels of IL-1β and NF-κB in the cerebellum tissue of 20 -weeks of age *WT*, 20 weeks of age DKO, and 20- and 30- weeks of age DKO mice after the administration of AAV alone, and in combination with AAV and istradefylline.

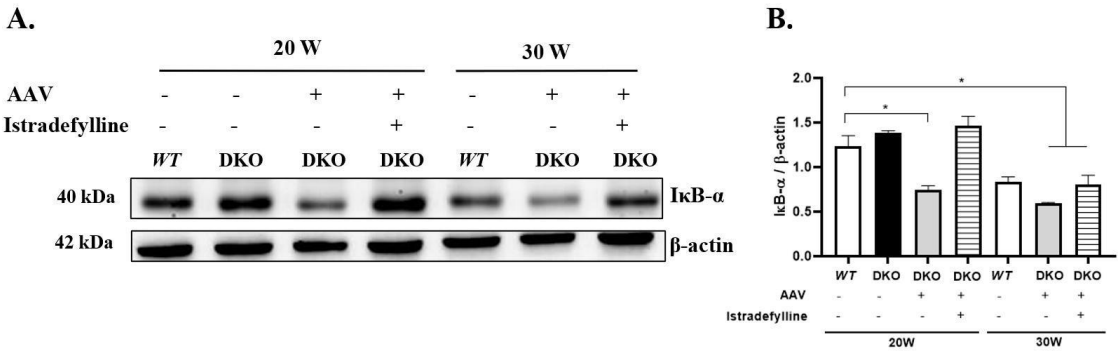

Figure 3.24. Immunoblot image (A) and densitometric analysis of IκB-α (B) in cerebellum tissue of 20- and 30- weeks of age *WT*, 20- weeks of age DKO mice, 20- and 30- weeks of age DKO mice administered with AAV, 20- and 30- weeks of age DKO mice administered with AAV and istradefylline (DKO; *Hexa-/-Neu3-/-*). β-actin was an internal control. Each band's intensity was detected using ImageJ and normalized to β-actin intensity. One-way ANOVA analysis was used to determine *p*-values by using GraphPad. Data were reported as means ± SEM (n=3; **p* < 0.05).

The expression level of IκB-α was reduced in the cerebellum of 20- weeks of age DKO mice after administering AAV compared to 20- weeks of age *WT* mice (Figure 3.24 A and Figure 3.24 B). Additionally, IκB-α levels demonstrated statistically significant lower in the cerebellum of 30- weeks of age DKO mice administered with AAV alone, and in a combination of AAV and istradefylline, relative to 20- weeks of age *WT* mice. (Figure 3.24 A and Figure 3.24 B).

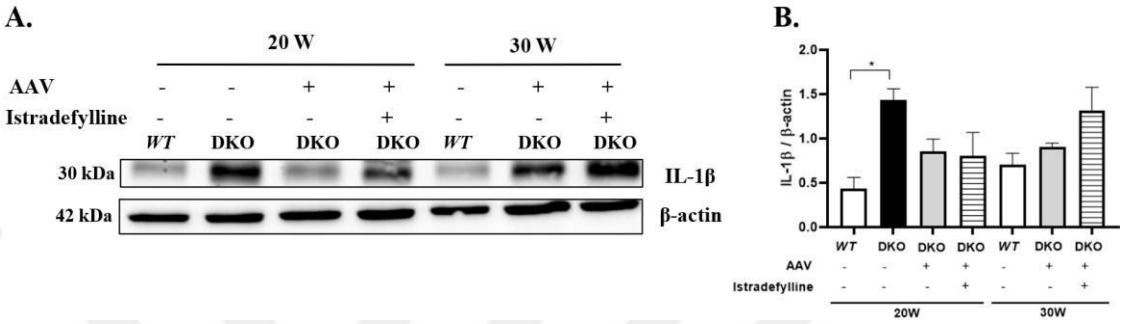

Figure 3.25. Immunoblot image (A) and densitometric analysis of IL-1β (B) in kidney tissue of 20- and 30- weeks of age *WT*, 20- weeks of age DKO mice, 20- and 30- weeks of age DKO mice administered with AAV, 20- and 30- weeks of age DKO mice administered with AAV and istradefylline (DKO; *Hexa-/-Neu3-/-*). β-actin was an internal control. Each band's intensity was detected using ImageJ and normalized to β-actin intensity. One-way ANOVA analysis was used to determine *p*-values by using GraphPad. Data were reported as means ± SEM (n=3; **p* < 0.05).

An elevated expression level of IL-1β was noted in kidneys of DKO mice compared to *WT* mice at 20 weeks (Figure 3.25 A and Figure 3.25 B). Although there was a slight reduction in IL-1β expression in the kidneys of DKO mice administered with AAV, and AAV combined with istradefylline, at both 20 and 30 weeks of age compared to 20- weeks of age DKO mice, this reduction was not statistically significant (Figure 3.25 A and Figure 3.25 B).

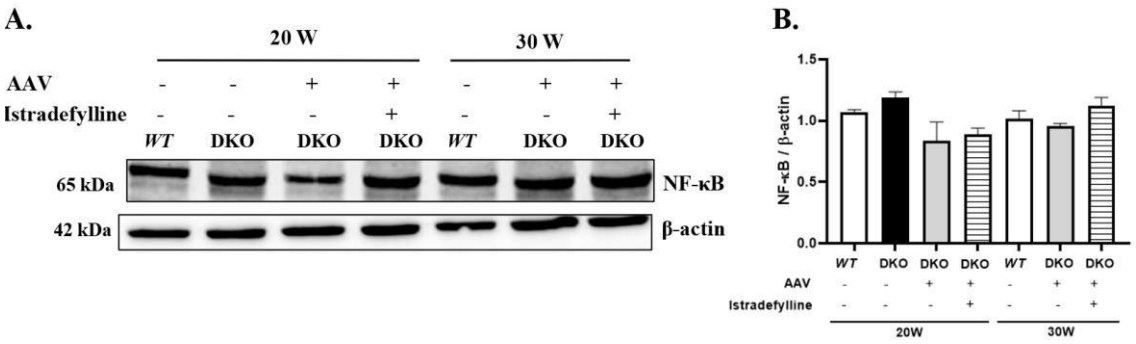

Figure 3.26. Immunoblot image (A) and densitometric analysis of NF-κB (B) in kidney tissue of 20- and 30- weeks of age *WT*, 20- weeks of age DKO mice, 20- and 30- weeks of age DKO mice administered with AAV, 20- and 30- weeks of age DKO mice administered with AAV and istradefylline (DKO; *Hexa-/-Neu3-/-*). β-actin was an internal control. Each band's intensity was detected using ImageJ and normalized to β-actin intensity. One-way ANOVA analysis was used to determine *p*-values by using GraphPad. Data were reported as means ± SEM (n=3).

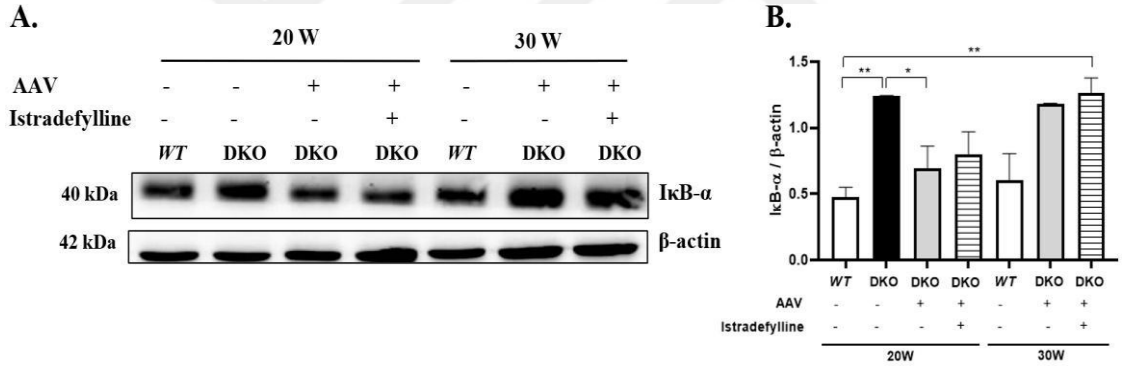

Figure 3.27. Immunoblot image (A) and densitometric analysis of IκB-α (B) in kidney tissue of 20- and 30- weeks of age *WT*, 20- weeks of age DKO mice, 20- and 30- weeks of age DKO mice administered with AAV, 20- and 30- weeks of age DKO mice administered with AAV and istradefylline (DKO; *Hexa-/-Neu3-/-*). β-actin was an internal control. Each band's intensity was detected using ImageJ and normalized to β-actin intensity. One-way ANOVA analysis was used to determine *p*-values by using GraphPad. Data were reported as means ± SEM (n=3; **p* < 0.05, ***p* < 0.025).

In the kidneys of mouse groups, no significant changes were observed in NF-κB expression across groups (Figure 3.26 A and Figure 3.26 B). However, elevated expression levels of IκB-α were noted in the 20- weeks of age DKO mice and 30- weeks of age DKO mice administered with AAV and istradefylline, compared to 20- weeks of age *WT* mice (Figure 3.27 A and Figure 3.27 B). A reduced expression level of IκB-α was

observed in 20- weeks of age DKO mice administered with AAV compared to 20- weeks of age DKO mice (Figure 3.27 A and Figure 3.27 B).

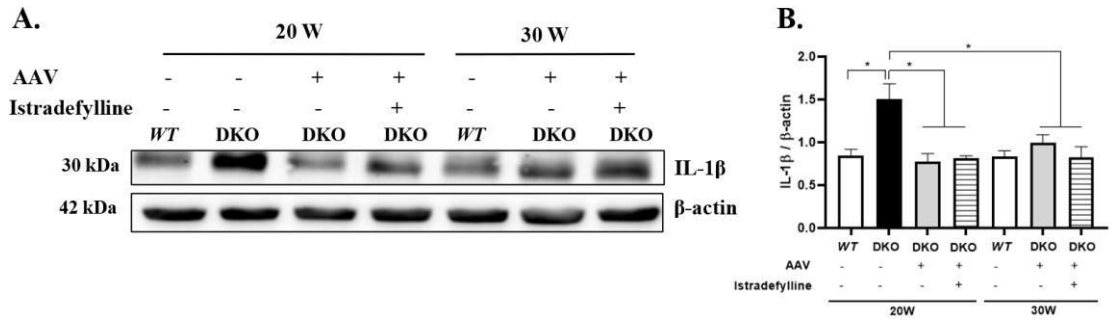

Figure 3.28. Immunoblot image (A) and densitometric analysis of IL-1β (B) in liver tissue of 20- and 30- weeks of age *WT*, 20- weeks of age DKO mice, 20- and 30- weeks of age DKO mice administered with AAV, 20- and 30- weeks of age DKO mice administered with AAV and istradefylline (DKO; *Hexa-/-Neu3-/-*). β-actin was an internal control. Each band's intensity was detected using ImageJ and normalized to β-actin intensity. One-way ANOVA analysis was used to determine *p*-values by using GraphPad. Data were reported as means ± SEM (n=3; $*p < 0.05$).

A statistically significant higher expression level of IL-1β was observed in livers of 20- weeks of age DKO mice compared to age-matched *WT* mice (Figure 3.28 A and Figure 3.28 B). After the administration of AAV alone, and in combination with istradefylline, a decrease in IL-1β expression levels was detected in livers of both 20- and 30-weeks of age DKO mice, compared to 20 -weeks of age DKO mice (Figure 3.28 A and Figure 3.28 B).

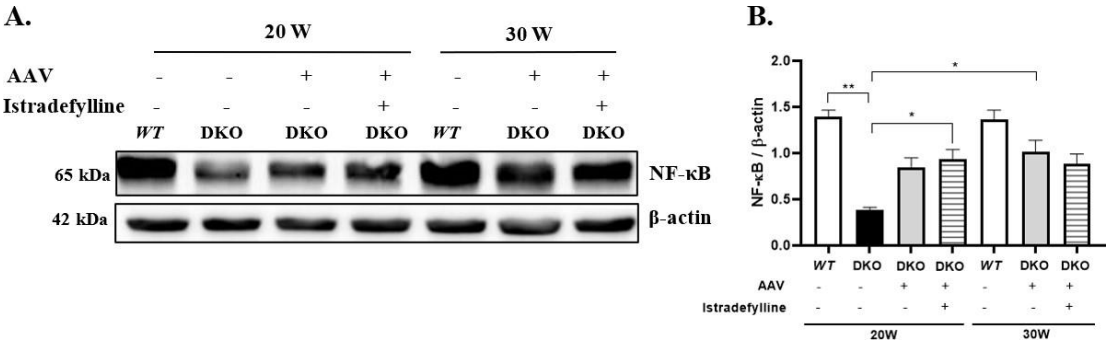

Figure 3.29. Immunoblot image (A) and densitometric analysis of NF-κB (B) in liver tissue of 20- and 30- weeks of age *WT*, 20- weeks of age DKO mice, 20- and 30- weeks of age DKO mice administered with AAV, 20- and 30- weeks of age DKO mice administered with AAV and istradefylline (DKO; *Hexa-/-Neu3-/-*). β-actin was an internal control. Each band's intensity was detected

using ImageJ and normalized to β-actin intensity. One-way ANOVA analysis was used to determine *p*-values by using GraphPad. Data were reported as means ± SEM (n=3; **p* < 0.05, ***p* < 0.025).

In the livers of mouse group, lower levels of NF-κB were observed in 20- weeks of age DKO mice compared to age-matched *WT* mice (Figure 3.29 A and Figure 3.29 B). However, NF-κB expression increased in 20- weeks of age DKO mice administered with AAV and istradefylline, as well as in 30- weeks of age DKO mice administered with AAV, in comparison to 20- weeks of age DKO mice (Figure 3.29 A and Figure 3.29 B).

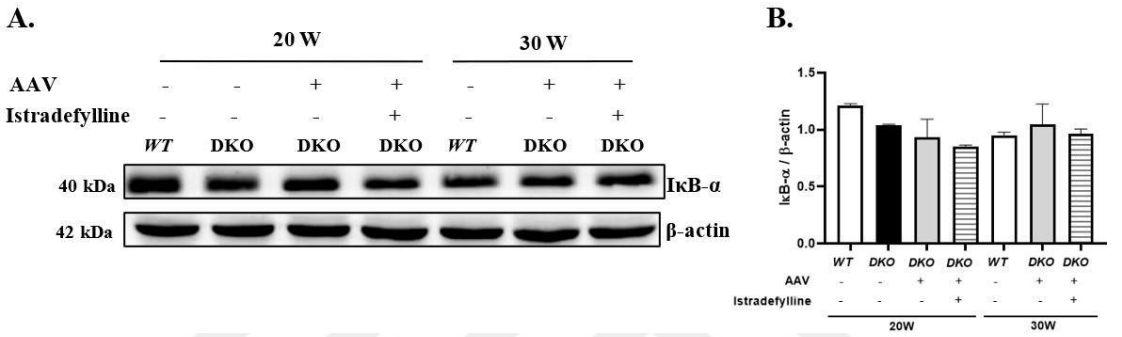

Figure 3.30. Immunoblot image (A) and densitometric analysis of IκB-α (B) in liver tissue of 20- and 30- weeks of age *WT*, 20- weeks of age DKO mice, 20- and 30- weeks of age DKO mice administered with AAV, 20- and 30- weeks of age DKO mice administered with AAV and istradefylline (DKO; *Hexa-/-Neu3-/-*). β-actin was an internal control. Each band's intensity was detected using ImageJ and normalized to β-actin intensity. One-way ANOVA analysis was used to determine *p*-values by using GraphPad. Data were reported as means ± SEM (n=3).

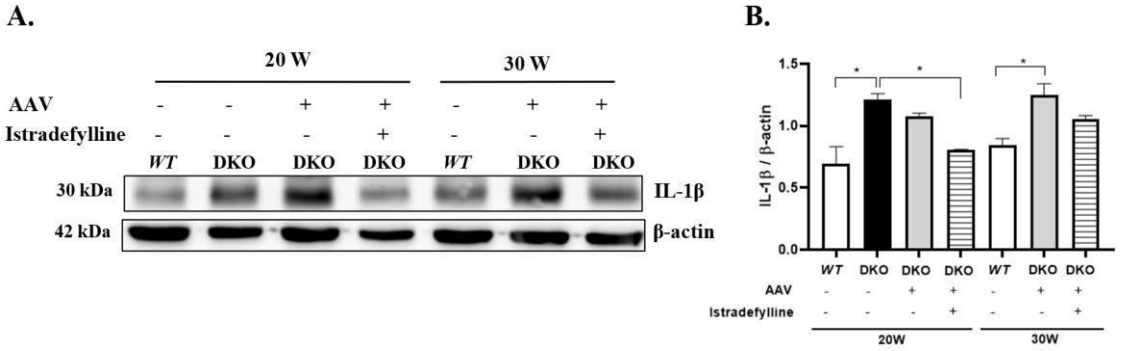

Figure 3.31. Immunoblot image (A) and densitometric analysis of IL-1β (B) in spleen tissue of 20- and 30- weeks of age *WT*, 20- weeks of age DKO mice, 20- and 30- weeks of age DKO mice administered with AAV, 20- and 30- weeks of age DKO mice administered with AAV and istradefylline (DKO; *Hexa-/-Neu3-/-*). β-actin was an internal control. Each band's intensity was detected using ImageJ and normalized to β-actin intensity. One-way ANOVA

analysis was used to determine *p*-values by using GraphPad. Data were reported as means ± SEM (n=3; **p* < 0.05).

No apparent changes in the expression of IκB-α were observed in the livers of the mouse groups (Figure 3.30 A and Figure 3.30 B).

IL-1β expression levels showed an elevation in DKO mice compared to *WT* mice at 20 weeks in the spleen. Moreover, an increased expression of IL-1β was observed in the spleens of 30- weeks of age DKO mice administered with AAV compared to 30-weeks of age *WT* mice (Figure 3.31 A and Figure 3.31 B). Besides, a reduced expression of IL-1β was detected in the spleens of 20- weeks of age of DKO mice after the administration of a combined AAV and istradefylline treatment compared to 20- weeks of age DKO mice (Figure 3.31 A and Figure 3.31 B).

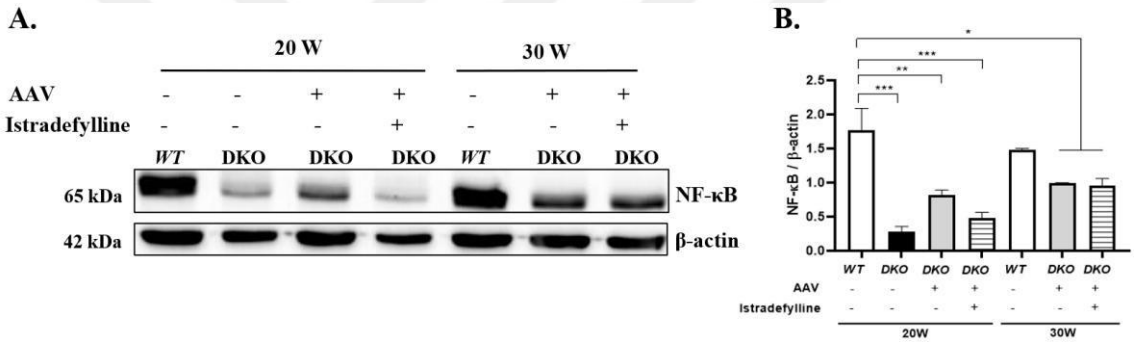

Figure 3.32. Immunoblot image (A) and densitometric analysis of NF-κB (B) in spleen tissue of 20- and 30- weeks of age *WT*, 20- weeks of age DKO mice, 20- and 30- weeks of age DKO mice administered with AAV, 20- and 30- weeks of age DKO mice administered with AAV and istradefylline (DKO; *Hexa-/-Neu3-/-*). β-actin was an internal control. Each band's intensity was detected using ImageJ and normalized to β-actin intensity. One-way ANOVA analysis was used to determine *p*-values by using GraphPad. Data were reported as means ± SEM (n=3; **p* < 0.05, ***p* < 0.025, ****p* < 0.01).

NF-κB expression levels were reduced in the spleens 20- weeks of age DKO mice, as well as in 20- and 30-weeks of age DKO mice after administration of AAV alone, and in combined with istradefylline, compared to 20- weeks of age *WT* mice (Figure 3.32 A and Figure 3.32 B).

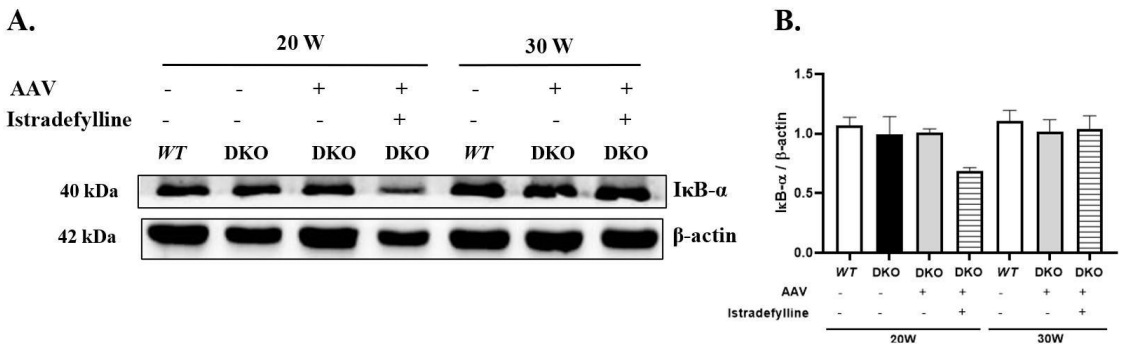

Figure 3.33. Immunoblot image (A) and densitometric analysis of IκB-α (B) in spleen tissue of 20- and 30- weeks of age *WT*, 20- weeks of age DKO mice, 20- and 30- weeks of age DKO mice administered with AAV, 20- and 30- weeks of age DKO mice administered with AAV and istradefylline (DKO; *Hexa-/-Neu3-/-*). β-actin was an internal control. Each band's intensity was detected using ImageJ and normalized to β-actin intensity. One-way ANOVA analysis was used to determine *p*-values by using GraphPad. Data were reported as means ± SEM (n=3).

There were no significant changes in the expression levels of IκB-α in the spleens across the different mouse groups (Figure 3.33 A and Figure 3.33 B).

3.10. Immunohistochemistry Analyses

The cortex, hippocampus, thalamus, and cerebellum of 20- and 30 weeks of age *WT*, 20- weeks of age DKO mice, 20- and 30- weeks of age DKO mice administered with AAV, 20- and 30- weeks of age DKO mice administered with AAV and istradefylline were analyzed in immunohistochemistry. GM2, Lamp1, NeuN, CNPase, and GFAP staining were performed for immunohistochemistry analyses.

3.10.1. Anti-GM2 Staining

Anti-GM2 staining was performed to evaluate the changes in accumulating GM2 ganglioside in DKO mice with the administration of AAV alone and with istradefylline.

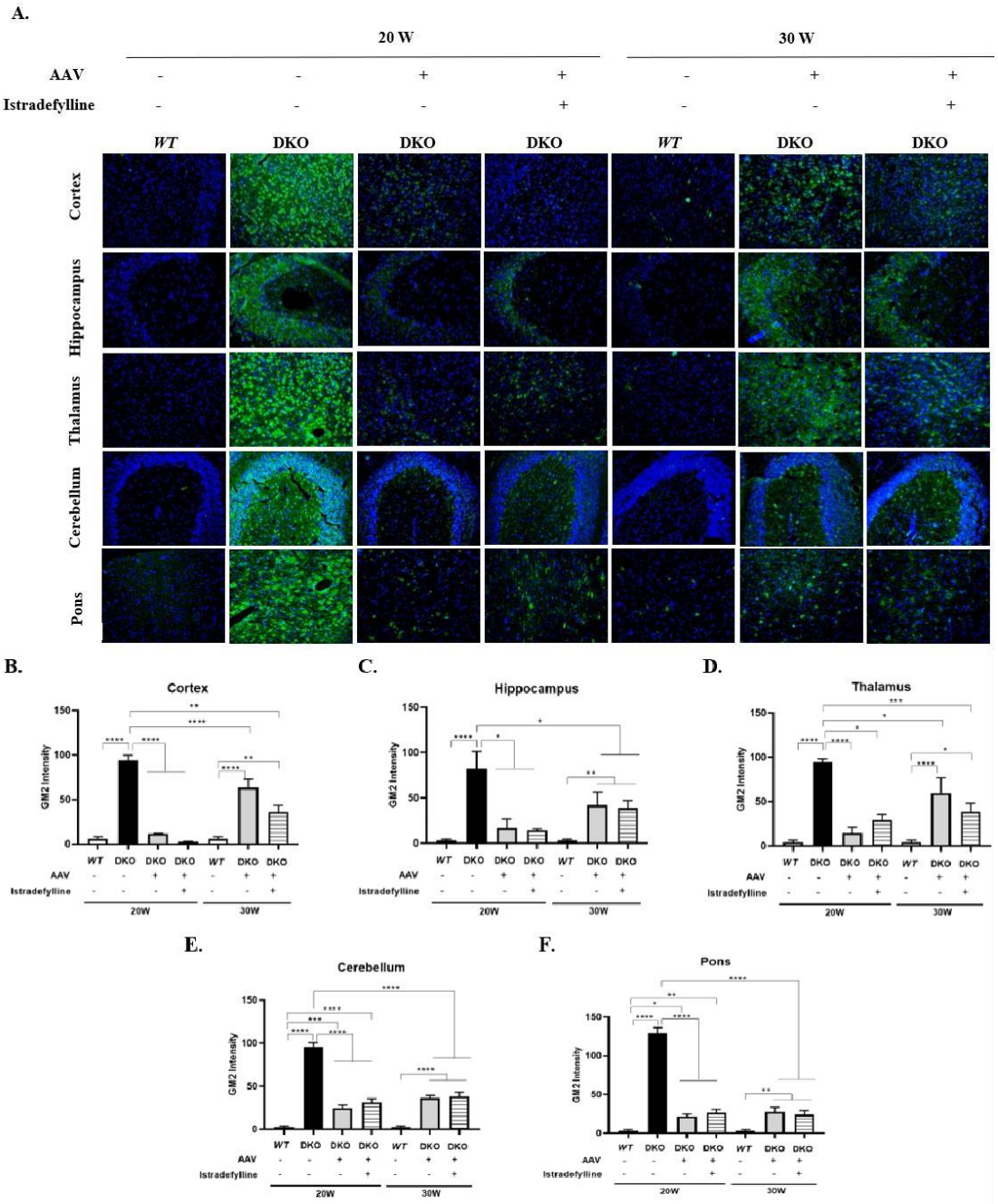

Figure 3.34. Immunostaining of GM2 in brain coronal sections (A), cortex, hippocampus, thalamus, cerebellum, and pons of 20- and 30- weeks of age *WT*, 20- weeks of age DKO mice, 20- and 30- weeks of age DKO mice administered with AAV, 20- and 30- weeks of age DKO mice administered with AAV and istradefylline (DKO; *Hexa-/-Neu3-/-*). Images were taken at 20X magnification under the same light intensity that differs filter types for DAPI and anti-KM966. Sections were stained with anti-KM966 antibody (green; GM2 marker) and DAPI (blue; nucleus). The intensity of GM2 was measured with ImageJ (B-F). One-way ANOVA analysis was used to determine *p*-values by using GraphPad. Data were reported as means ± SEM (n=3; **p* < 0.05, ***p* < 0.025, ****p* < 0.01, and *****p* < 0.001).

The combined gene deficiency of *Hexa* and *Neu3* genes resulted in the excessive accumulation of GM2 ganglioside in several brain regions, including the cortex (Figure 3.34 B), hippocampus (Figure 3.34 C), thalamus (Figure 3.34 D), cerebellum (Figure 3.34 E), and pons (Figure 3.34 F) of DKO mice at 20- weeks of age. As expected, no accumulation of GM2 ganglioside was observed in *WT* mice at both 20 and 30 weeks in all brain sections examined (Figure 3.34).

The accumulated GM2 ganglioside degraded in the cortex, hippocampus, thalamus, cerebellum, and pons of DKO mice upon the administration of AAV alone and in combination with istradefylline (Figure 3.34 B) at 20 weeks. However, while a significantly increased level of GM2 ganglioside was detected in all analyzed brain sections of 30- weeks of age DKO mice administered with AAV and in combination with istradefylline, compared to 30- weeks of age *WT* mice (Figure 3.34), there was a reduction in the level of GM2 ganglioside in 30- weeks of DKO mice after administration of AAV and combined AAV and istradefylline, compared to 20- weeks of age DKO mice. This data suggests that AAV-mediated gene therapy was effective in reducing GM2 ganglioside accumulation in DKO mice.

3.10.2. Anti-Lamp1 Staining

To understand the effect of AAV-mediated gene therapy and istradefylline as an anti-inflammatory agent, the level of lysosomes was detected using anti-Lamp1 staining for each mouse group.

Significantly increased levels of lysosomes were observed in the cortex (Figure 3.35 B), hippocampus (Figure 3.35 C), thalamus (Figure 3.35 D), cerebellum (Figure 3.35 E), and pons (Figure 3.35 F) of 20- weeks of age DKO mice compared to age-matched *WT* mice.

A slight degradation of accumulated lysosomes was observed in the cortex (Figure 3.35 B), hippocampus (Figure 3.35 C), and cerebellum (Figure 3.35 E) of DKO mice after the administration of AAV, and AAV with istradefylline at 20 weeks of age, compared to age-matched DKO mice. In the thalamus, there was a significant decrease in the levels of lysosomes in 20- weeks of age DKO mice administered with AAV, and AAV in combination with istradefylline, compared to age-matched DKO mice (Figure 3.35 D). Furthermore, a reduced level of lysosomes was detected in the pons of 20- and 30- weeks

of age DKO mice after administration of AAV, and AAV with istradefylline, compared to 20- weeks of age DKO mice (Figure 3.35 F).

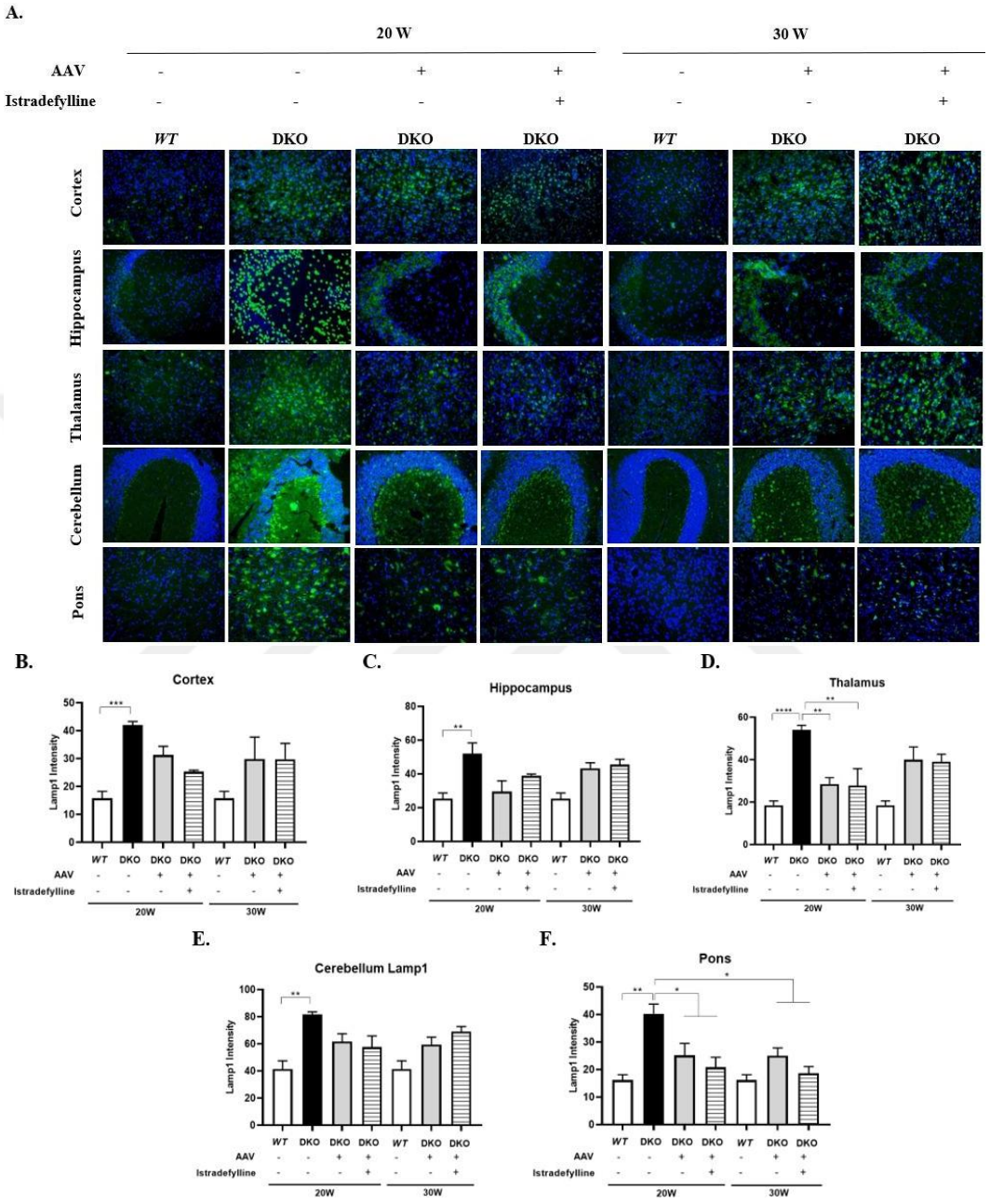

Figure 3.35. Immunostaining of Lamp1 (lysosome marker) in brain coronal sections (A), cortex, hippocampus, thalamus, cerebellum, and pons of 20- and 30- weeks of age *WT*, 20- weeks of age DKO mice, 20- and 30- weeks of age DKO mice administered with AAV, 20- and 30- weeks of age DKO mice administered with AAV and istradefylline (DKO; *Hexa-/-Neu3-/-*). Images were taken at 20X magnification under the same light intensity that differs filter types for DAPI and anti-Lamp-1. Sections were stained with anti-

Lamp1 antibody (green; lysosome marker) and DAPI (blue; nucleus). Intensity of Lamp1 was measured with ImageJ (B-F). One-way ANOVA analysis was used to determine *p*-values by using GraphPad. Data were reported as means ± SEM (n=3; *$p < 0.05$, **$p < 0.025$, ***$p < 0.01$, and ****$p < 0.001$).

3.10.3. Anti-NeuN Staining

Anti-NeuN staining was performed to determine the neuron intensity in the brain section of each mouse group. Brain sections from each mouse group were immunostained using a NeuN antibody, which specifically targets the neurons.

As shown in Figure 3.36, there was a loss of neurons, indicating neurodegeneration in the cortex (Figure 3.36 B), hippocampus (Figure 3.36 C), thalamus (Figure 3.36 D), and pons (Figure 3.36 F) of DKO mice at 20 weeks compared to age-matched control littermates. However, no statistically significant change was observed in the cerebellum of 20- weeks of age DKO mice compared to age-matched *WT* mice (Figure 3.36 E).

AAV-mediated gene therapy, as well as the combined treatment of AAV and istradefylline, restored the neuronal density, with an increased number of neurons in the cortex (Figure 3.36 B), hippocampus (Figure 3.36 C), thalamus (Figure 3.36 D), and pons (Figure 3.36 F) of DKO mice at 20 and 30 weeks, compared to DKO mice at 20 weeks. However, no significant change in neuron density was observed in the cerebellum across all mouse groups (Figure 3.36 E).

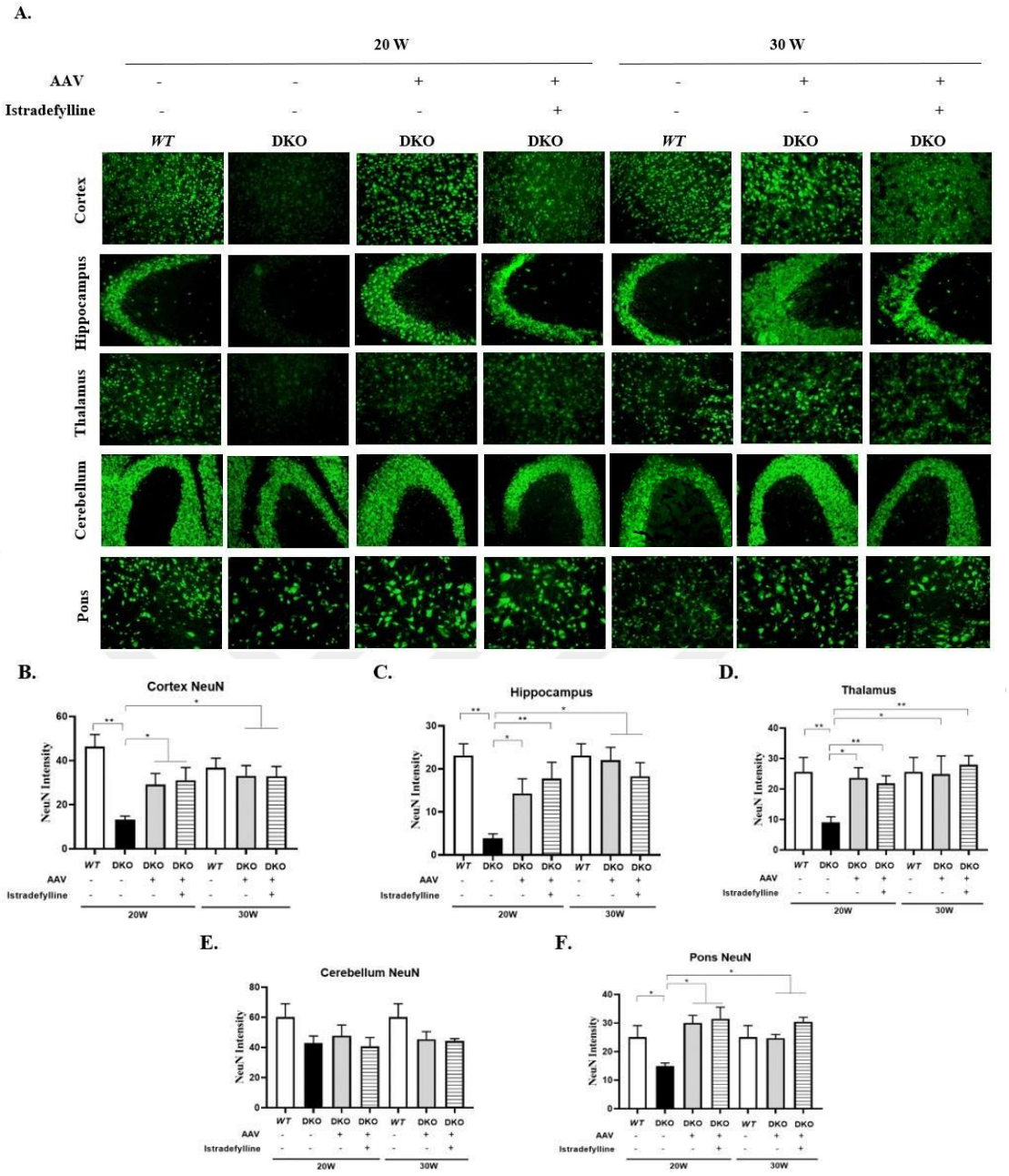

Figure 3.36. Immunostaining of NeuN (neuron marker) in brain coronal sections (A), cortex, hippocampus, thalamus, cerebellum, and pons of 20- and 30- weeks of age *WT*, 20- weeks of age DKO mice, 20- and 30- weeks of age DKO mice administered with AAV, 20- and 30- weeks of age DKO mice administered with AAV and istradefylline (DKO; *Hexa-/-Neu3-/-*). Images were taken at 20X magnification under the same light intensity. The intensity of NeuN was measured with ImageJ (B-F). One-way ANOVA analysis was used to determine *p*-values by using GraphPad. Data were reported as means ± SEM (n=3; $*p < 0.05$, $**p < 0.025$).

3.10.4. Anti- CNPase Staining

The oligodendrocyte density was determined using anti-CNPase staining for each mouse group. An anti-CNPase antibody, which specifically recognize oligodendrocytes, was used to analyze demyelination process based on the oligodendrocyte density.

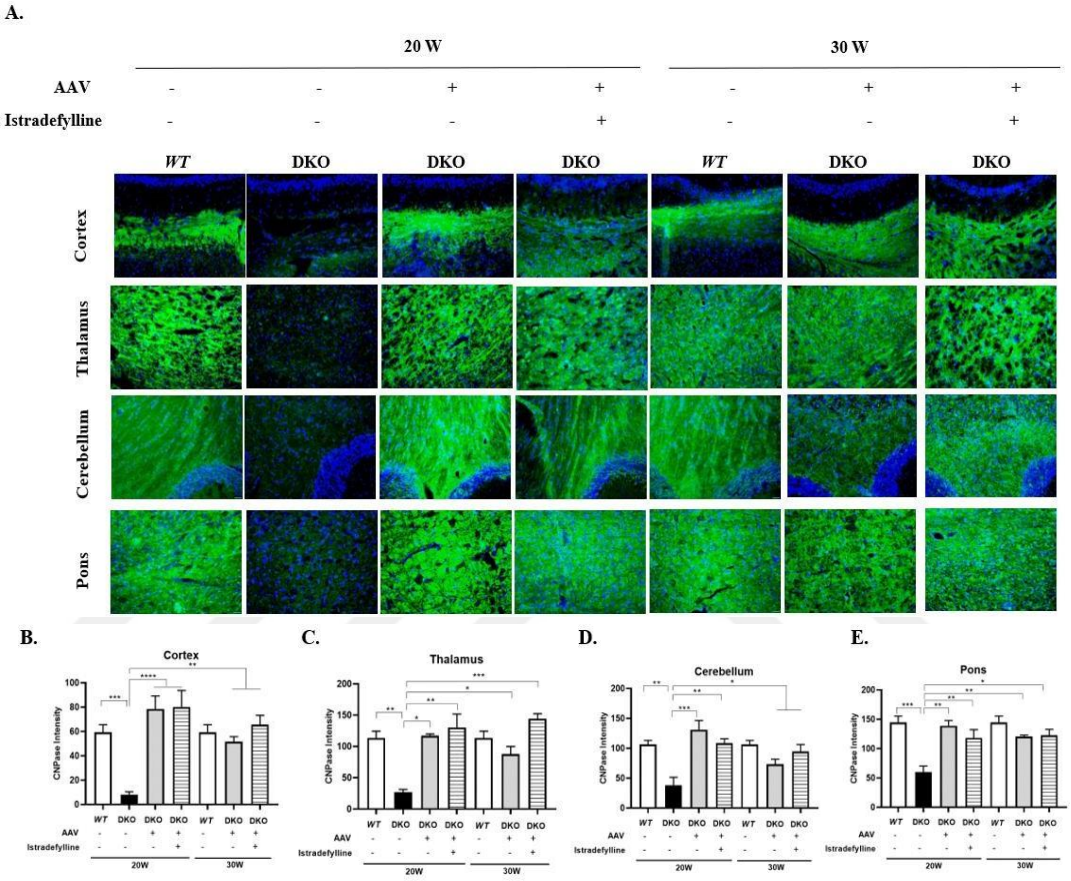

Figure 3.37. Immunostaining of CNPase (oligodendrocyte marker) in brain coronal sections (A), cortex, hippocampus, thalamus, cerebellum, and pons of 20- and 30- weeks of age *WT*, 20- weeks of age DKO mice, 20- and 30- weeks of age DKO mice administered with AAV, 20- and 30- weeks of age DKO mice administered with AAV and istradefylline (DKO; *Hexa-/-Neu3-/-*). Images were taken at 20X magnification under the same light intensity that differs filter types for DAPI and anti-CNPase. Sections were stained with anti-CNPase antibody (green; oligodendrocyte marker) and DAPI (blue; nucleus). Intensity of GM2 was measured with ImageJ (B-E). One-way ANOVA analysis was used to determine *p*-values by using GraphPad. Data were reported as means ± SEM (n=3; **p* < 0.05, ***p* < 0.025, ****p* < 0.01, and *****p* < 0.001).

Immunostaining with anti-CNPase revealed the loss of oligodendrocytes, demonstrating demyelination in the brains of DKO mice at 20 weeks, compared to age-matched *WT* mice (Figure 3.37). A significant loss of oligodendrocytes was observed in the cortex (Figure 3. 37 B), thalamus (Figure 3.37 C), cerebellum (Figure 3.37 D), and pons of these mice (Figure 3.37 E).

The elevated level of oligodendrocytes, based on the anti-CNPase intensity, was noted in both 20- and 30- weeks of age DKO mice administered AAV, and AAV with istradefylline, compared to 20- weeks of age DKO mice in all analyzed brain sections, including cortex, thalamus, cerebellum, and pons (Figure 3.37). No significant change in the anti-CNPase intensity was observed between the AAV-administered DKO mice and *WT* mice, indicating no demyelination in these DKO mice after AAV administration at both 20 and 30 weeks (Figure 3.37).

3.10.5. Anti-GFAP Staining

The presence of active astrocytes was determined using anti-GFAP staining for each mouse group. An anti-GFAP antibody was used to stain the astrocytes, and active astrocytes were determined based on their morphological changes.

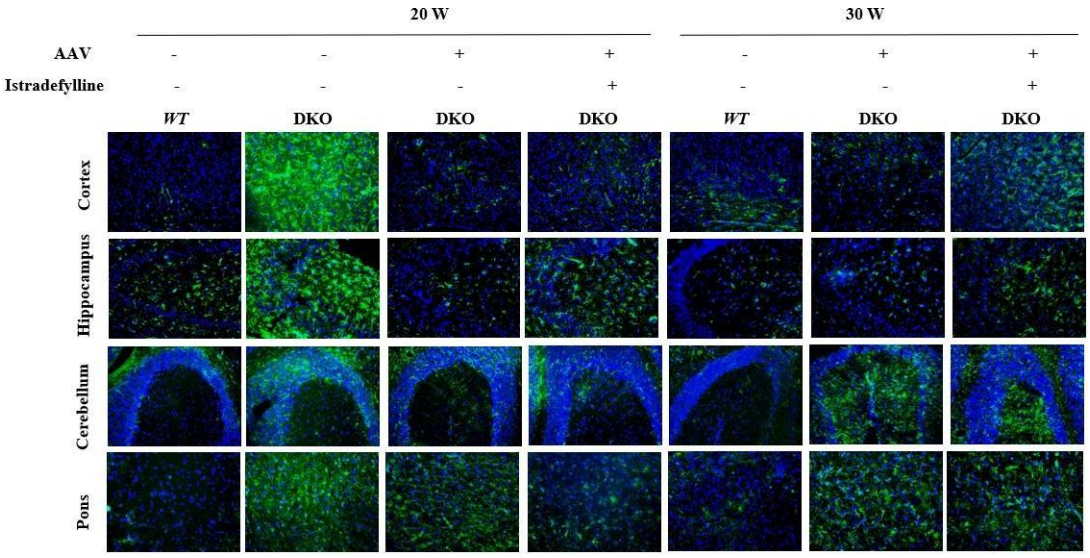

Figure 3.38. Immunostaining of GFAP (astrocyte marker) in brain coronal sections, cortex, hippocampus, thalamus, cerebellum, and pons of 20- and 30- weeks of age *WT*, 20- weeks of age DKO mice, 20- and 30- weeks of age DKO mice administered with AAV, 20- and 30- weeks of age DKO mice

administered with AAV and istradefylline (DKO; *Hexa-/-Neu3-/-*). Images were taken at 20X magnification under the same light intensity that differs filter types for DAPI and anti-GFAP. Sections were stained with anti-GFAP antibody (green; GM2 marker) and DAPI (blue; nucleus) (n=3).

According to anti-GFAP staining results, activated astrocytes, identified by their morphology, were detected in the cortex, hippocampus, and pons of 20- weeks of age DKO mice (Figure 3.38). In the cerebellum of 20- weeks of age DKO mice, the active astrocytes were present but were less numerous compared to other brain regions such as the cortex, hippocampus, and pons (Figure 3.38).

No active astrocytes were determined, particularly in cortex and cerebellum, of 20- weeks of age DKO mice administered AAV, and AAV with istradefylline (Figure 3.38). Activated astrocytes were detected in the pons and cerebellum of 30- weeks of age DKO mice administered AAV, and AAV with istradefylline, but the number of active astrocytes in these mice was lower than that observed 20- weeks of age DKO mice (Figure 3.38).

3.11. Behavioral Test

Rotarod and footprint tests were performed to evaluate the changes in the behaviors in mice groups.

3.11.1. Rotarod Test

The motor coordination and balance were assessed using the rotarod test (Nampoothiri et al., 2017). Changes in motor function and activity, which are controlled by the cerebellum, were evaluated in a genotype- and age-dependent manner (Lee et al., 2018).

In the rotarod test, it was observed that there was a reduction in latency time to fall, indicating impairments in the motor function and balance, in 20- weeks of age DKO mice, compared to age-matched *WT* mice (Figure 3.39).

AAV-mediated gene therapy, as well as the combined treatment of AAV and istradefylline, improved motor and locomotor function in 20- weeks of age DKO mice

compared to untreated, age-matched DKO mice (Figure 3.39), as evidenced by the elevated latency time in 20- weeks of age DKO mice administered with AAV, and AAV combined with istradefylline.

A significant decrease in latency time to fall was observed in the 30- weeks of age DKO mice administered with AAV, and AAV with istradefylline, compared to 30- weeks of age *WT* mice (Figure 3.39). However, motor activity and locomotor activity in these mice were better than 20- weeks of age DKO mice, as shown by the increased latency time to fall (Figure 3.39).

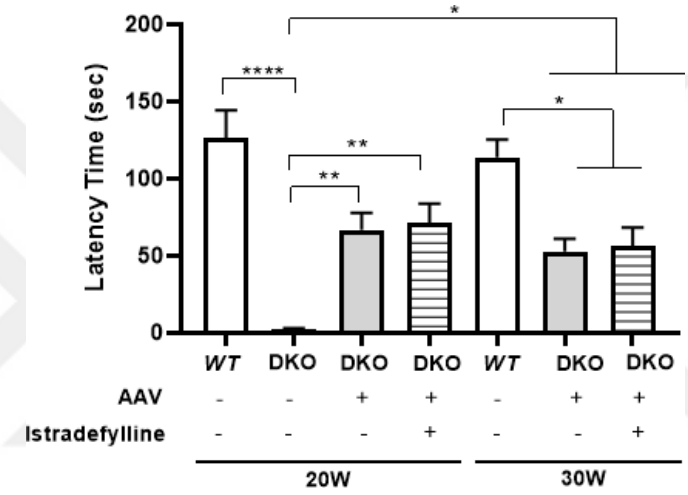

Figure 3.39. Running time on rotarod (sec) of 20- and 30- weeks of age *WT*, 20- weeks of age DKO mice, 20- and 30- weeks of age DKO mice administered with AAV, 20- and 30- weeks of age DKO mice administered with AAV and Istradefylline (DKO; *Hexa-/-Neu3-/-*). One-way ANOVA analysis was used to determine *p*-values by using GraphPad. Data were reported as means ± SEM (n=6 independent mice for each mice group; *$p < 0.05$, **$p < 0.025$, ****$p < 0.001$).

3.11.2. Footprint Test

The walking pattern of mice was determined using the Footprint test. The paw analyses show the presence of affected neurons which control the movement of the legs. Gait abnormalities were analyzed using this test in a genotype- and age-dependent manner.

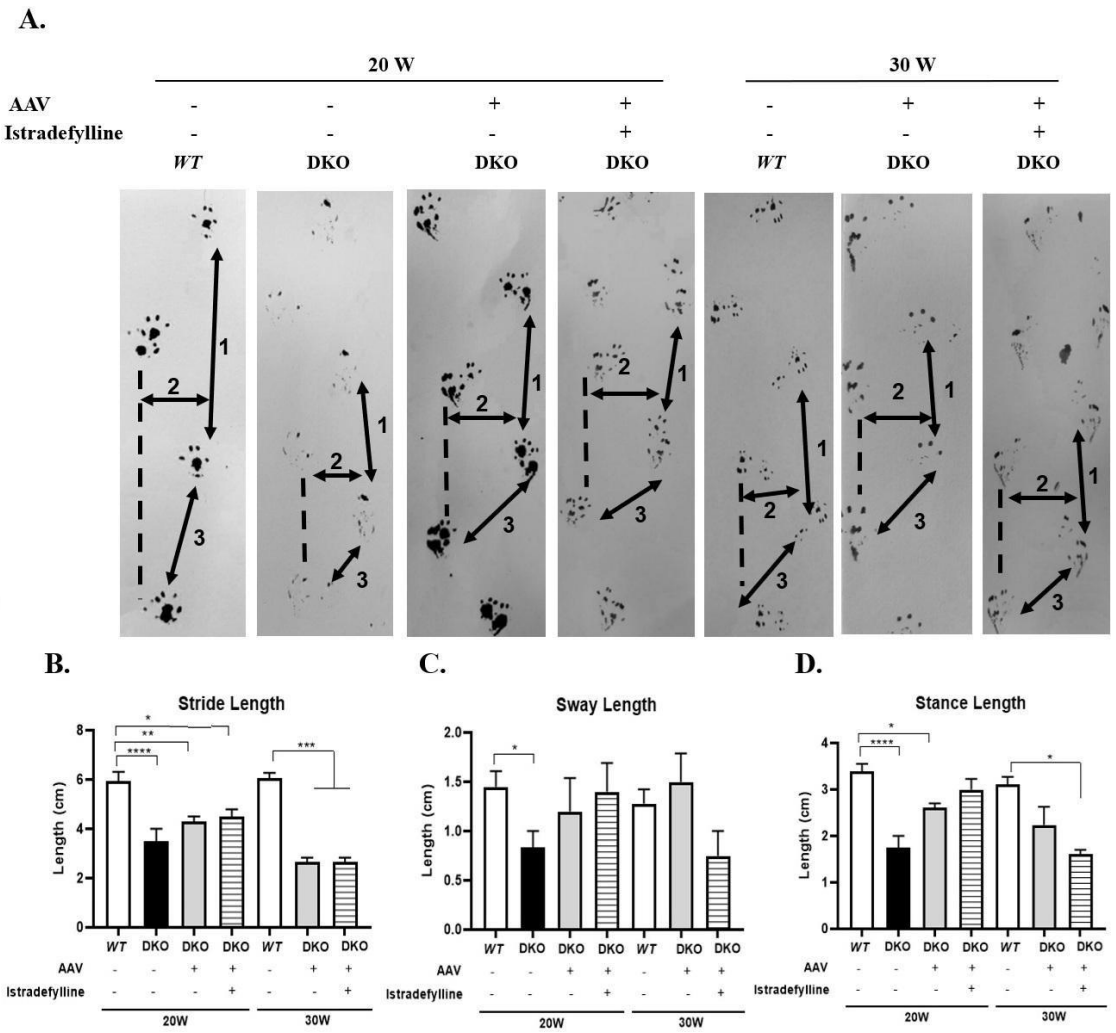

Figure 3.40. (A) Footprint analysis; stride length (1), sway length (2), and stance (3) length of *WT*, DKO mice, DKO mice administered with AAV, DKO mice administered with AAV and Istradefylline (DKO; *Hexa-/-Neu3-/-*). (B) Stride length, (C) sway length, and (D) stance length. One-way ANOVA analysis was used to determine *p*-values by using GraphPad. Data were reported as means ± SEM (n=6 independent mice for each mice group; *$p < 0.05$, **$p < 0.025$, ***$p < 0.01$, and ****$p < 0.001$).

The stride (Figure 3.40 B), sway (Figure 3.40 C), and stance (Figure 3.40 D). lengths were analyzed, and a statistically significant decrease in these lengths was observed in 20- weeks of age DKO mice compared to age-matched *WT* mice (Figure 3.40).

In terms of stride length, a reduction was observed in 20-weeks of age DKO mice administered with AAV, and in those mice administered with a combination of AAV and istradefylline, compared to 20- weeks of age *WT* mice (Figure 3.40 B). Additionally, a reduced stride length was noted in 30- weeks of age DKO mice administered with AAV,

and the combination of AAV and istradefylline, compared to age-matched *WT* mice (Figure 3.40 B).

In the stance length, there was reduced length in 20- weeks of age DKO mice administered with AAV, compared to 20- weeks of age *WT* mice (Figure 3.40 D). The reduced stance length was also observed in 30-weeks of age DKO mice administered with AAV and istradefylline, compared to age-matched *WT* mice (Figure 3.40 D).

CHAPTER 4

DISCUSSION

Tay-Sachs disease, a GM2 gangliosidosis and lysosomal storage disorder, is caused by the mutations in *HEXA* gene which encodes the α-subunit of enzyme β-hexosaminidase A (Yamanaka et al., 1994). The HEXA enzyme is a lysosomal enzyme that catalyzes the degradation of GM2 ganglioside into GM3 ganglioside. The deficiency in the HEXA enzyme leads to the accumulation of GM2 ganglioside in lysosomes, resulting in mental retardation, severe neurological problems, motor function impairments, muscle weakness, and eventually death, typically between the ages of 2 – 4 years (Bley et al., 2011). As a Tay-Sach disease mouse model, *Hexa-/-* mice have been generated. However, these mice did not show severe symptoms, and there is only limited accumulation of GM2 ganglioside in the central nervous system (Taniike et al., 1995). Recently, a new mouse model, *Hexa-/-Neu3-/-* (DKO), was created as an early-onset Tay-Sachs disease mouse model, with combined deficiencies in the *Hexa* and *Neu3* genes (Seyrantepe et al., 2018). In *Hexa-/-Neu3-/-* (DKO) mice, excessive accumulation of GM2 ganglioside, increased levels of lysosomes, and elevated neuroinflammation resulted in death at 20- weeks of age (Seyrantepe et al., 2018). Additionally, these mice displayed slow movement, tremors, and ataxia as neurological symptoms. In recent studies, our research group exhibited altered lipid metabolism (Can et al., 2022), including changes in phosphatidylethanolamine (PE), phosphatidylinositol (PI), phosphatidylcholine (PC), and sphingomyelin (SM), as well as impaired autophagic flux in the brains of *Hexa-/- Neu3-/-* (DKO) mice (Sengul et al., 2023). In a more recent study, it was indicated that lithium treatment regulates and rescues the impaired autophagic flux in the cell models of Tay-Sachs disease (Basirli et al., 2024).

Several therapeutic strategies have been developed for lysosomal storage disorders, including enzyme replacement therapy, substrate reduction therapy, pharmacological chaperone therapy, hematopoietic stem cell transplantation therapy, and gene therapy (Fernández-Pereira et al., 2021). Adeno-associated virus (AAV)-based gene therapy is a novel gene therapy strategy for treating lysosomal storage disorders due to several advantages, including low immunogenicity, non-pathogenicity, a wide range of

tissue targets, and long-term gene expression (Park et al., 2017). Additionally, compared to lentiviral-based vectors, AAV vectors used in gene therapy remain episomal instead of integrated into the host genome, for expression of the target of interest (Li and Samulski, 2020). AAV serotypes allow the transduction of distinct types of tissues, and the AAVrh10 (Rhesus Macaque) serotype is known to be neurotropic showing tropism for neurons, oligodendrocytes, and astrocytes (Park et al., 2017).

Although different therapeutic strategies have been evaluated for lysosomal storage disorders, such as Gaucher disease, Mucopolysaccharidoses, and Niemann Pick C disease, effective treatments for Tay-Sachs disease have yet to be developed. Due to the lack of a proper mouse model for Tay-Sachs disease, no treatments have been tested previously. Within the framework of this thesis study, the therapeutic efficacy of intrathecal administration of AAVrh10-mHexa, expressing mouse *HEXA*, was investigated in an early-onset Tay-Sachs disease mouse model, DKO mice. Additionally, we aimed to elucidate whether istradefylline treatment, in combination with AAVrh10 expressing mHexa, could mitigate neuroinflammation pathology in DKO mice. For this purpose, AAVrh10 expressing mHexa (AAV) was administered to 8- weeks of age DKO mice, and then intraperitoneal istradefylline injections were applied when DKO mice at 10- weeks of age. To assess the therapeutic efficacy of AAV-based gene therapy and istradefylline, *WT* and DKO mice, which did not receive any treatment, were used as control groups. Molecular biological, histochemistry analyses, and behavioral analyses were performed for each experimental and control group.

Before evaluating the *in vivo* efficacy of AAV-based gene therapy, the transduction efficacy of AAVrh10 expressing mHexa was first confirmed *in vitro* using a transduction test and anti-GM2 staining in the neuroglia cells from 20- weeks of age DKO mice. The observation of mCherry signal, an indicator of the reporter gene, confirmed the transduction efficacy of AAV in these cells (Figure 3.3 B). More importantly, anti-GM2 staining showed the degradation of GM2 ganglioside in AAV-transduced neuroglia cells from DKO mice compared to non-transduced neuroglia cells, demonstrating the ability of AAV to degrade the accumulated GM2 ganglioside through mHexa expression (Figure 3.4).

Intrathecal injection of AAV was administered to DKO mice at 8- weeks of age, and the effect of AAV-based gene therapy was evaluated *in vivo* (Figure 3.6 A). As previously reported (Seyrantepe et al., 2018), DKO mice exhibited smaller size, reduced body weight, and eventually sudden death by 20- weeks of age compared to age-matched

control littermates. Consistently, body weight measurements indicated a dramatic and rapid loss in body weight in DKO mice compared to *WT* mice after 16- weeks of age (Figure 3.6 B). AAV-based gene therapy alone, and in combination with istradefylline, restored the body weight of DKO mice (Figure 3.6 B and C). Although DKO mice could survive until 20– weeks of age, AAV administration, both alone and in combination with istradefylline, extended survival up to 30 weeks (Figure 3.6D), highlighting the effectiveness of AAV-based gene therapy expressing mHexa, combined with the anti-inflammatory agent istradefylline, in improving body weight and prolonging the lifespan of DKO mice.

In GM2 gangliosidoses, Tay-Sachs disease and Sandhoff disease, excessive accumulation of GM2 ganglioside has been shown previously in both patients and mouse models of these diseases (Solovyeva et al., 2018). In an early-onset Tay-Sachs disease mouse model, *Hexa-/-Neu3-/-*, progressive accumulation of GM2 ganglioside in the brain sections, cortex, and cerebellum, was indicated through thin layer chromatography analyses. The effectiveness of AAV was shown using thin layer chromatography analyses in the DKO mice following the administration of AAV alone, and in a combination with istradefylline. Consistent with the previous results, excessive accumulation of GM2 ganglioside was detected in the cortex of DKO mice (Figure 3.7). The administration of either AAV alone, or combination with istradefylline resulted in significantly degradation of accumulating GM2 ganglioside in the brain of DKO mice at both 20 (Figure 3.7 A and B) and 30 weeks of age (Figure 3.7 C and D), compared to non-treated DKO mice at 20 weeks, indicating the effectiveness of AAV-based gene therapy to degrade the GM2 ganglioside through expression of mHexa.

AAVrh10 has the potential to efficiently transduce the central nervous system, compared to other serotypes of AAV such as AAV2, AAV5, AAV6, and AAV8. The therapeutic efficacy of AAVrh10 through intracranial and intrathecal administration has been demonstrated in several lysosomal storage disorders, including Krabbe disease (Rafi et al., 2012), neuronal ceroid lipofuscinosis (Sondhi et al., 2007), metachromatic leukodystrophy (Piguet et al., 2012), diabetic neuropathy (Homs et al., 2014),and amyotrophic lateral sclerosis (H. Wang et al,. 2014), and mucopolysaccharidosis (MPS) type IIIA (Hocquemiller et al., 2020). The increased expression of the target gene resulted in elevated levels of their enzyme products in the brains of AAVrh10-treated mice groups. These studies demonstrated the effectiveness of AAVrh10 for targeting the central nervous system. In addition to the central nervous system, AAVrh10 shows also tropism

for other tissues, including the kidney, liver, spleen, lung, muscle, and eye (Hoshino et al., 2019). Hexa enzyme activity, using enzyme activity assay, and the mHexa expression, determined by RT-PCR, were evaluated in the brain and other visceral organs (kidney, liver, and spleen) after mice were treated with AVVrh10 expressing mHexa (AAV). In the brain, both cortex (Figure 3.8) and cerebellum (Figure 3.9) showed significantly increased levels of mHexa expression and Hexa enzyme activity in 20- and 30- weeks of age DKO mice administered with AAV alone or in combination with istradefylline, compared to 20-weeks of age DKO mice. These findings exhibited the activity of Hexa enzyme through the successful expression of mHexa in the brains of DKO mice using AAVrh10 virus particles. Moreover, the lack of observable age-dependent changes in DKO mice treated with AAV alone or combined with istradefylline suggests long-term gene expression of mHexa in DKO mice, facilitated by AAVrh10 (Figures 3.8 and 3.9).

In addition to the brain, to understand the effect of AAVrh10 on other tissues, the expression level of mHexa and Hexa enzyme activity was also determined in the kidney, liver, and spleen. Although no significant difference, only a slight increase, was detected in the expression level of mHexa in the liver of DKO mice administered with AAV alone (Figure 3.11 A), and in combination with istradefylline, the observation of higher levels of Hexa enzyme activity demonstrated the efficacy of AAVrh10 administration expressing mHexa (Figure 3.11 B). Other examined tissues, including the kidney (Figure 3.10) and spleen (Figure 3.12), showed similar results, with elevated expression levels of mHexa and Hexa enzyme activity when DKO mice were treated with AAV, and AAV with istradefylline in both 20 -and 30- weeks of age, compared to 20- weeks of age DKO mice. These findings confirm the tropism of AAVrh10 for visceral organs, including the kidney, liver, and spleen. Additionally, the increased activity of Hexa enzyme in the serum of DKO mice administered with AAV, and in combination with istradefylline, showed the circulation of AAVrh10 in the bloodstream after the intrathecal administration (Figure 3.13).

Increased levels of neuroinflammation have been shown in several lysosomal storage disorders, including Niemann Pick disease type C (Vruchte et al., 2004), sialidosis (D'Azzo et al., 2015), and GM1 gangliosidosis (Jeyakumar, 2003). In previous work, the elevated levels of neuroinflammation-related cytokines and chemokines, including Ccl2, Ccl3, Ccl4, and Cxcl10, along with the reduced expression levels of the anti-inflammatory markers, were detected in the brains of *Hexa-/-Neu3-/-* (DKO) mice (Demir et al., 2020). Additionally, istradefylline, an anti-inflammatory agent, was shown to reduce inflamatory

cytokines and chemokines, as well as microglia activation (Iba1), in the brains of *Hexb*-/- mice, a Sandhoff disease mice model (Ogawa et al., 2018). In this study, the aim was to understand the effect of AAVrh10 expressing mHexa on neuroinflammation. Moreover, in the combined treatment including both AAV and istradefylline administration, the impact of istradefylline as an anti-inflammatory was investigated in DKO mice. Consistent with previous findings, elevated expression level of neuroinflammatory markers, including CCL3, CCL5, GFAP in the cortex (Figure 3.14), as well as CCL2, CCL3, CCL5, Cxcl10, IL-1β, Iba1, and GFAP in the cerebellum (Figure 3.15), were observed in 20- weeks of age DKO mice compared to age-matched controls using RT-PCR. These results confirmed the elevated neuroinflammation in the brain of 20- weeks of age DKO mice. The reduced expression of CCL3, CCL5, and GFAP was demonstrated with the administration of AAV alone, or in combination with istradefylline in the cortex of DKO mice, particularly at 20- weeks of age, compared to age-matched DKO mice (Figure 3.14). In the cerebellum, CCL2 and IL-1β indicated lower expression in 20- weeks of age DKO mice treated with AAV alone, or in combination with istradefylline (Figure 3.15). These findings highlighted the alleviation effect of AAV-based gene therapy, with mHexa expression, on neuroinflammation pathology in DKO mice. The elevated expression level of Iba1, a marker for active microglia, significantly reduced in DKO mice treated with AAV and istradefylline at 20 weeks, compared to age-matched control groups, suggesting the anti-inflammatory effect of istradefylline.

The regulation of inflammatory markers was assessed in the kidney, liver and spleen of different mouse groups (Figure 3.16, Figure 3.17, and Figure 3.18). Previous studies reported the excessive production of inflammatory markers such as IL1β, TNFα, and IL6, in the brain, kidney liver, spleen, and lung of a mouse model of Gaucher disease (Pandey, 2023). Furthermore, elevated levels of inflammatory markers, including IFNγ, TNFα, IL1β, and IL6, were observed in the brain and other peripheral organs such as the spleen, kidney, liver, lung, and heart (Pandey, 2023). Pro-inflammatory markers, CCL2, CCL3, and CCL5, were significantly increased in the kidney (Figure 3.16) and liver (Figure 3.17) of 20- weeks of age DKO mice, while CCL5, Cxcl10, and IL-1β showed elevated levels in the spleen of 20- weeks of age DKO mice compared to age-matched *WT* mice (Figure 3.18). These results indicate elevated inflammation in the visceral organs of DKO mice at 20- weeks of age in addition to the brain. The decrease in CCL3 and CCL5 levels was observed in the kidney and liver, and the reduction in Cxxl10, and

IL-1β was seen in the spleen of DKO mice administered with AAV alone, or with a combination of AAV and istradefylline, compared to non- treated-20- weeks of age DKO mice. These findings suggest the potential anti- inflammatory effect of AAV through the expression of mHexa in these visceral organs. Moreover, AAV administration alone, via mHexa expression, appears sufficient to reduce inflammation in the tissues.

Tay-Sachs disease is a lysosomal storage disorder characterized by the accumulation of undegraded metabolites in lysosomes, leading to increased lysosomal expansion. Elevated lysosome levels were previously observed in the early-onset Tay-Sachs disease mouse model (Seyrantepe et al., 2018). To understand the effect of AAV and istradefylline treatment in DKO mice, the expression of lysosome-related marker, Lamp-1 was evaluated using RT-PCR analysis. As expected, lysosome accumulation was observed in the cortex and cerebellum of DKO mice at 20 weeks, compared to age-matched *WT* mice (Figure 3.14 H and Figure 3.15 H). Administration of AAV alone or in combination with istradefylline reduced lysosome accumulation in the cortex and cerebellum of 20-week-old DKO mice compared to non-injected age-matched DKO mice (Figure 3.14 H and Figure 3.15 H). Moreover, while slightly reduced lysosome levels were detected in the cortex of 30- weeks of age DKO mice treated with AAV or AAV and istradefylline, significantly lower Lamp-1 expression was noted in the cerebellum of these mice compared to 20- weeks of age DKO mice (Figure 3.14H and Figure 3.15H). The higher expression level of Lamp-1 was also investigated in other tissues of DKO, including the kidney, liver and spleen. Significantly elevated levels of lysosomes were detected in the kidney, and spleen of DKO mice compared to *WT* mice at 20- weeks of age. Moreover, higher expression level of Lamp-1 was also investigated in other tissues, kidney (Figure 3.16 F), liver (Figure 3.17 F) and spleen (Figure 3.18 F). The significantly elevated levels of lysosomes were also detected in kidney, and spleen in DKO mice compared to *WT* mice at 20 weeks (Figure 3.16 F and Figure 3.18. F). Moreover, single AAV, and combined AAV and istradefylline administration reduced the accumulating lysosomes in DKO mice at both 20 and 30 weeks, showing the effectiveness of mHexa expression in these tissues in addition to the brain using the AAVrh10 serotype.

The inflammation-related markers, IL-1β, NF-kB, and IkB-α were also assesed using Western Blot analysis in the brain and visceral organs of all mouse groups. Interleukin-1 beta (IL-1 β), a pro-inflammatory cytokine, promotes the production of pro-inflammatory mediators and induces inflammatory responses in astrocytes (Lopez-

Castejon and Brough, 2011). It plays a key role in initiating and amplifying immune responses, especially in reaction to infection, injury, and neurodegenerative diseases. IL-1β is produced as pro-IL-1β in response to pathogen-associated molecular patterns (PAMPs). Macrophage, which express pattern recognition receptors (PRR) induce the pro-IL-1β expression in a process known as priming (Takeuchi and Akira, 2010). The expressed pro-IL-1β is cleaved with the activation of caspase 1, leading to the production of mature IL-1β. The mature IL-1β is secreted from cells though the exact mechanism of its secretion is not fully understood (Lopez-Castejon and Brough, 2011). Elevated expression levels of IL-1β have been observed in brains of Niemann Pick type C mouse model (Vruchte et al., 2004), in mouse models and patients with GM2 gangliosidosis (Jeyakumar, 2003), and in Sandhoff disease (Wada et al., 2000). NF-kB and IkB-α are also regulators of immune responses, as well as other cellular processes such as cell proliferation, cell survival, and differentiation. NF-kB consists of five different proteins including p65 (RelA), c-Rel, p52, p50, and RelB. Two major pathways regulate NF-kB activation: the canonical and non-canonical pathways (T. Liu et al., 2017). In the common pathway, canonical pathway, NF-kB activation leads to the production and secretion of cytokines, chemokines, and many different mediators in the innate immune cell response. Activation of the canonical pathway typically occurs through cytokines such as TNF-α and IL-1β, which bind to their respective receptors, TNF-R1 and IL-1βR (Iacobazzi et al., 2023). Additionally, the pathogen-associated molecular patterns (PAMPS) activate toll-like receptors (TLR), triggering the formation of a complex including NEMO and IKK1/2. Autophosphorylation of IKK leads to phosphorylation of IkBs (IkBα/β/ε), which normally inhibit NF-by sequestering it in the cytoplasm. However, the phosphorylation of IkBs, IkBα/β/ε, releases NF-κB, allowing it to translocate to the nucleus and activate target genes, including those for inflammatory cytokines (H. Yu et al., 2020). In the non-canonical pathway (NEMO independent pathway), ligands such as B-cell activating factor (BAFF), CD40 ligand, and lymphotoxin cause the activation of this pathway. Furthermore, TNFR-related ligands are also recognized by TNF receptors in this pathway. This pathway leads to the activation of NIK, which phosphorylates IKKα (Iacobazzi et al., 2023). Phosphorylated IKKα then phosphorylates p100, resulting in its processing into p52 and subsequent dimerization with RelB. The p52-RelB complex translocate to the nucleus, where it activates the transcription of inflammatory genes (G. Xiao et al., 2001). Despite these known inflammatory roles, some studies have suggested that elevated NF-κB levels may reduce inflammation by inhibiting pro-inflammatory cytokine and other

chemokine expression, suggesting an anti-inflammatory role (Lawrence, 2009). In our data, no significant change in the expressions of IL-1β (Figure 3.19), NF-kB (Figure 3.20), and IkB-α (Figure 3.21) was detected in cortex of all mouse groups. In the cerebellum, although IL-1β (Figure 3.22) and NF-kB (Figure 3.23) showed no significant changes, the decreasing expression level of IkB-α was observed in 20- weeks of age DKO mice administered with AAV, and 30- weeks of age DKO mice administered with AAV alone or in combination with istradefylline, compared to 20-weeks of age *WT* mice (Figure 3.24). This reduced level of IkB-α may be associated with suppression of NF-kB in the case of treatments since NF-kB plays role in the production of IkB-α. Due to the activity of Hexa in other tissues following AAV-based gene therapy, inflammation-related markers were also evaluated at the protein level in the visceral organs of all mouse groups. The elevated expression level of IL-1β was observed in the kidneys of DKO mice at 20-weeks of age compared to age- matched control mice, indicating increased level of inflammation (Figure 3.25). Although an elevated level of IκB-α is usually associated with inhibition of NF-κB-mediated inflammation, NF-κB activation is not solely dependent on IκB-α inhibition. Therefore, an increased level of IkB-α may be an indicator of the anti-inflammation process, but more inflammation-related markers should be analyzed to understand the inflammatory process in cells. In the kidneys, no significant changes in NF-κB expression were observed among the mouse groups (Figure 3.26). However, an elevated level of IkB-α was observed in 20- weeks of age DKO mice, and 30- weeks of age DKO mice administered with AAV and istradefylline, compared to 20- weeks of age *WT* mice (Figure 3.27). Based on these findings, it is difficult to definitively conclude the presence or absence of inflammation in the kidneys of DKO mice. On the other hand, the increased level of IL-1β in liver (Figure 3.28) and spleen (Figure 3.31) of DKO mice at 20 weeks, compared to age-matched *WT* mice, showed inflammation in these tissues. Moreover, reduced IL-1β levels following AAV treatment, either alone or in combination with istradefylline, indicated the alleviation of inflammation in kidneys of DKO mice at both 20- and 30- weeks (Figure 3.28). Interestingly, unlike IL-1β, decreased levels of NF-κB in the liver (Figure 3.29) and spleen (Figure 3.32) of 20-week-old DKO mice compared to age-matched *WT* mice may suggest that inflammation in these tissues is activated via alternative pathways, independent of NF-κB.

Immunohistochemistry analyses were applied to assess the effects of AAV-based gene therapy alone and in combination with istradefylline on several conditions in mouse

groups, including GM2 level, lysosome level, neuronal density, demyelination process, and astrocyte activation. In GM2 gangliosidoses, Tay-Sachs disease and Sandhoff disease, excessive accumulation of GM2 ganglioside has been shown previously in both patients and mouse models of these diseases (Solovyeva et al., 2018). In an early-onset Tay-Sachs disease mouse model, *Hexa-/-Neu3-/-*, progressive accumulation of GM2 ganglioside in the brain sections, cortex, and cerebellum, was indicated through thin-layer chromatography analyses. On the other hand, the efficacy of scAAV9.47 expressing *HEXM* (which encodes α subunit site and stabilizes the β subunit interface) was shown in *Hexa-/-* mice, where intracranial administration of this vector led to degradation of GM2 ganglioside (Tropak et al., 2016). However, *Hexa-/-* mice, with limited GM2 accumulation, did not mimic symptoms seen in Tay-Sachs disease patients, so this mouse model was not an appropriate model for developing new therapy strategies. GM2 ganglioside levels were determined using anti-GM2 staining, in addition to thin-layer chromatography analyses. Consistent with prior studies, the excessive accumulation of GM2 ganglioside was shown in the cortex (Figure 3.34 B), hippocampus (Figure 3.34 C), thalamus (Figure 3.34 D), cerebellum (Figure 3.34 E), and pons (Figure 3.34 F) of DKO mice at 20- weeks of age, compared to the age-matched control mice. Following administration of AAV alone, and in combination with istradefylline, significant degradation of accumulated GM2 ganglioside was detected in all brain regions analyzed in DKO mice at 20 weeks (Figure 3.34). Even though the limited accumulation of GM2 ganglioside was detected in the cortex (Figure 3.34 B), hippocampus (Figure 3.34 C), thalamus (Figure 3.34 D), cerebellum (Figure 3.34 E), and pons (Figure 3.34 F) of treated DKO mice at 30- weeks of age, compared to age-matched *WT* mice, the treatments led to significant GM2 degradation compared to untreated DKO mice (Figure 3.34). This data indicates that AAV-based gene therapy was effective in reducing GM2 ganglioside accumulation in DKO mice via mHexa expression.

In addition to the GM2 ganglioside level, lysosome levels were assessed using Lamp1 staining to evaluate lysosomal accumulation in brain sections (Figure 3.35). As expected, increased lysosome levels were determined in the cortex (Figure 3.35 B), hippocampus (Figure 3.35 C), thalamus (Figure 3.35 D), cerebellum (Figure 3.35 E), and pons (Figure 3.35 F) of DKO mice at 20 weeks, compared to age-matched controls. Although slight reductions in lysosome levels were detected in the cortex, hippocampus, and cerebellum of AAV-treated, and AAV and istradefylline-treated DKO mice at both 20 and 30 weeks, significant reductions in lysosomes were seen in the thalamus (Figure 3.35

D), and pons (Figure 3.35 F) of these mice, compared to 20- weeks of age DKO mice. These findings confirm lysosome accumulation in the brain of DKO mice and demonstrate lysosomal degradation following AAV-based gene therapy and istradefylline administration.

Neuronal density was analyzed using anti-NeuN staining to investigate the impact of mHexa expression following AAV-based gene therapy on neurons. Neurodegeneration, neuronal death (apoptosis), and neuronal loss are common in several lysosomal storage disorders and neurodegenerative disorders. Reduced neuronal intensity and increased apoptosis have been observed in the cortex, pons, and thalamus of early-onset Tay-Sachs mice (Demir et al., 2020). In this study, neuronal loss, an indicator of neurodegeneration, was evident in the cortex (Figure 3.36 B), hippocampus (Figure 3.36 C), thalamus (Figure 3.36 D), and pons (Figure 3.36 F) of DKO mice at 20 weeks, compared to age-matched *WT* mice. Consistent with this research, no significant changes in neuronal density were observed between *WT* and DKO mice in the cerebellum (Figure 3.36 E). AAV-based gene therapy provided the restoration of neuronal density in the cortex (Figure 3.36 B), hippocampus (Figure 3.36 C), thalamus (Figure 3.36 D), and pons (Figure 3.36 F) of DKO mice at both 20 and 30 weeks. Moreover, combined AAV and istradefylline treatment further improved neuronal density in DKO mice at both ages compared to untreated DKO mice at 20 weeks (Figure 3.36). These findings, consistent with anti-GM2 staining, indicate that GM2 clearance in the brain prevented neurodegeneration and restored neuronal density in DKO mice treated with AAV alone or in combination with istradefylline.

Oligodendrocytes produce myelin sheath that coats the axons of neurons, facilitating signal transmission (Onyenwoke and Brenman, 2015). Some gangliosides including, GD1a and GT1b, are localized on the axons of neurons and promote the myelination process (Can et al., 2022). However, excessive lipid and ganglioside accumulation can disrupt these myelination processes. Previously, it has been clarified that Tay-Sachs and Sandhoff disease patients exhibit lower expression levels of myelin basic protein (MBP), a marker for myelination (Myerowitz, 2002). Additionally, elevated level of demyelination due to abnormal accumulation of GM2 ganglioside was also shown in the brains of *Hexa-/-Neu3-/-* mice using anti-myelin basic protein (MBP) staining and luxol-fast blue (LFB) staining (Can et al., 2022). Along with GM2 ganglioside accumulation, increased neuroinflammation further makes oligodendrocytes more susceptible, leading to demyelination (Peferoen et al., 2014). In this research, CNPase,

a marker for oligodendrocytes, staining was performed to determine whether there is a gain in oligodendrocytes following AAV-based gene therapy in DKO mice exhibiting demyelination. Our results demonstrated lower CNPase intensity, indicating a reduced number of oligodendrocytes in the cortex (Figure 3.37 B), thalamus (Figure 3.37 C), cerebellum (Figure 3.37 D), and pons of (Figure 3.37 E) of DKO mice at 20 weeks compared to age-matched *WT* mice. At both 20 and 30 weeks of age, all brain sections of DKO mice administered with AAV alone, and in combination with istradefylline showed increased intensity of oligodendrocytes compared to DKO mice at 20- weeks of age, suggesting an enhancement in the myelination process (Figure 3.37). The absence of a difference in the oligodendrocyte intensity between *WT* mice and DKO mice administered with AAV alone and in combination with istradefylline indicates the efficient oligodendrocyte activity in the myelination process following AAV-based gene therapy and anti-inflammation treatments.

Astrocytes are glia cells of the central nervous system that perform several functions, such as regulating microglial cells, maintaining blood-brain barrier (BBB) homeostasis, and supporting the energy metabolism of neurons (Valles et al., 2023). In cases of damage or injury, microglia cells are activated. Active microglia secrete cytokines and chemokines for damaged or injured parts, leading to the activation of astrocytes. Active astrocytes, a condition known as astrogliosis, have been observed in the cerebral part of Niemann-Pick A mouse model, the cortex of the Sandhoff mouse model (Sango et al., 1995), and the hippocampal and cerebellar of the Pompe mouse model (Clarke et al., 2021). Additionally, in the cortex, hippocampus, and cerebellum of the Tay-Sachs disease mouse model (*Hexa-/-Neu3-/-* mice), active astrocytes were visualized using anti-GFAP staining (Demir et al,. 2020). Active astrocytes were determined based on their morphologies in this study. It was demonstrated that active astrocytes were present in the cortex, hippocampus, and pons of 20- weeks of age DKO mice compared to 20- weeks of age *WT* mice (Figure 3.38). However, no active astrocytes were detected, particularly in cortex and cerebellum, of 20- weeks of age DKO mice administered AAV, and AAV combined with istradefylline (Figure 3.38). Activated astrocytes were detected in the pons and cerebellum of 30- weeks of age DKO mice administered AAV, and AAV with istradefylline, but the number of active astrocytes in these mice was lower than that in 20- weeks of age DKO mice (Figure 3.38). These findings demonstrate the efficacy of AAV-mediated mHexa expression in reducing astrogliosis in a region-specific manner.

Behavioral analyses were conducted for each mouse group to investigate how AAV-based gene therapy and anti-inflammatory treatments affect behavioral patterns. The rotarod test is a widely used method to evaluate motor functions and impairments (Lee et al., 2018). The cerebellum is a region of the brain that controls movement and locomotor activities (Lee et al., 2018). The higher latency time to fall is associated with the proper motor function, whereas less time spent on the rotating rod signifies impaired locomotor activities and motor function (Seyrantepe et al., 2018). In an early-onset Tay-Sachs disease mouse model, impaired locomotor activity and balance problems were observed compared to control groups (Seyrantepe et al., 2018). Moreover, reduced locomotor activity was also confirmed in these mice using an open-field test (Demir et al., 2020). In this study, as expected, DKO mice at 20- weeks of age were unable to stay on the rotating rod, indicating severe impairments in motor coordination and activity (Figure 3.39). Although 30- weeks of age DKO mice administered with AAV alone, and combined with istradefylline showed reduced motor activity compared to age-matched control groups, improvements in motor coordination and locomotor activity were noted in DKO mice following treatment with AAV and AAV combined with istradefylline, compared to non-treated-DKO-mice (Figure 3.39). These results showed the efficacy of AAV-mediated gene therapy in improving motor coordination and locomotor activity.

Gait abnormalities were assessed based on footprint patterns using footprint analyses. The stride (Figure 3.40 B), sway (Figure 3.40 C), and stance (Figure 3.40 D) lengths were evaluated for each mouse group. Previously, reduced stride, sway and stance lengths - indicating impairments in neurons controlling leg and paw movements - were observed in the early-onset Tay-Sachs disease mouse model (Seyrantepe et al., 2018). The gait impairments based on reduced stride, sway, and stance lengths were shown in DKO mice at 20 weeks, compared to 20- weeks of age *WT* mice (Figure 3.40). Additionally, reduced stride and stance lengths were detected in 20- weeks of age DKO mice treated with AAV, compared to the control group (Figure 3.40).

CHAPTER 5

CONCLUSION

Tay-Sachs disease, a lysosomal storage disorder, is caused by mutations in the *HEXA* gene. *HEXA* gene encodes for the α-subunit of the enzyme β-hexosaminidase A which degrades GM2 ganglioside in the brain and peripheral nervous system. The loss of the β-hexosaminidase A activity causes pathological accumulation of GM2 ganglioside in patients. Our group generated a mice model with a combined deficiency of *Hexa* and *Neu3* genes which showed abnormalities in size and numbers of lysosomes, abnormal GM2 ganglioside accumulation especially in the brain and severe neuropathological indications similar to Tay-Sachs patients. *Hexa-/-Neu3-/-* mice (DKO) undergo progressive neurodegeneration with neuronal loss and Purkinje cell depletion and survived up to 20-weeks of age. Recently, Adeno-associated virus (AAV)-based gene therapy has been shown as an efficient delivery system for human studies. AAVrh10 is especially used in AAV-based therapeutics to target the central nervous system.

Although various therapeutic strategies have been evaluated for lysosomal storage disorders, such as Gaucher disease, Mucopolysaccharidoses, and Niemann Pick C disease, effective treatments for Tay-Sachs disease have not yet been developed due to the lack of a proper mouse model. In this research, we aimed to investigate the therapeutic efficacy of the AAVrh10-mHexa (AAV) expressing mouse Hexa gene in the DKO mice. Additionally, the combined treatment of AAV-based gene therapy and istradefylline treatment, an anti-inflammatory agent, was assessed for its potential to degrade to GM2 ganglioside and reduce neuroinflammation, to develop new therapeutic strategies for Tay-Sachs disease.

We demonstrated that the life span of DKO mice extended up to 30 weeks after administration of AAV alone, and in combination with istradefylline. Thin Layer Chromatography analysis revealed degradation of accumulating GM2 ganglioside in the cortex of DKO mice at both 20- and 30- weeks of age, compared to 20- weeks of age DKO mice. Enzyme activity assay revealed elevated mouse Hexa activity in the cortex, cerebellum, and visceral organs (kidney, liver and spleen) of DKO mice following AAV treatment, either alone or in combination with istradefylline. In qRT-PCR analysis, we found reduced expression levels of lysosomal marker Lamp-1 and pro-inflammatory

cytokines, including Ccl2 and Ccl3, in the cortex and visceral organs of DKO mice administration of AAV alone and in combination with istradefylline. Immunohistochemistry data showed clearance of GM2 accumulation, reduced lysosome numbers, and lower levels of active astrocytes in the brain of DKO mice treated with either AAV alone or AAV combined with istradefylline at both 20 and 30 weeks. Moreover, immunostainings with NeuN and CNPase antibodies revealed an increased number of neurons and oligodendrocytes in these mice groups. Consistent with these results, motor activity also improved in DKO mice treated with AAV alone and in combination with istradefylline. Our data demonstrate that AAVrh10-based intrathecal administration, both alone and in combination with istradefylline, is a promising therapeutic strategy for treating Tay-Sachs disease.

REFERENCES

Ayuso, E.; Mingozzi, F.; Bosch, F. Production, Purification and Characterization of Adeno-Associated Vectors. *Curr. Gene Ther.* **2010**, *10* (6), 423–436.

Bartlett, J. S.; Wilcher, R.; Samulski, R. J. Infectious Entry Pathway of Adeno-Associated Virus and Adeno-Associated Virus Vectors. *J. Virol.* **2000**, *74* (6), 2777–2785.

Basirli, H.; Can, M.; Sengul, T.; Seyrantepe, V. Lithium Treatment Rescues Dysfunctional Autophagy in the Cell Models of Tay-Sachs Disease. *Mol. Genet. Metab.* **2024**, *141* (3), 108140.

Bley, A. E.; Giannikopoulos, O. A.; Hayden, D.; Kubilus, K.; Tifft, C. J.; Eichler, F. S. Natural History of Infantile GM2 Gangliosidosis. *Pediatrics* **2011**, *128* (5), e1233–e1241.

Borodzicz, S.; Czarzasta, K.; Kuch, M.; Cudnoch-Jedrzejewska, A. Sphingolipids in Cardiovascular Diseases and Metabolic Disorders. *Lipids Health Dis.* **2015**, *14* (1), 55.

Bosch, M. E.; Kielian, T. Neuroinflammatory Paradigms in Lysosomal Storage Diseases. *Front. Neurosci.* **2015**, *9*, 417.

Boustany, R.-M. N. Lysosomal Storage Diseases—The Horizon Expands. *Nat. Rev. Neurol.* **2013**, *9* (10), 583–598.

Cachón-González, M.-B.; Wang, S. Z.; Ziegler, R.; Cheng, S. H.; Cox, T. M. Reversibility of Neuropathology in Tay–Sachs-Related Diseases. *Hum. Mol. Genet.* **2014**, *23* (3), 730–748.

Can, M.; Sengül, T.; Demir, S. A.; İnci, O. K.; Basırlı, H.; Seyrantepe, V. Analysis of Brain Lipids in the Early-Onset Tay–Sachs Disease Mouse Model with the Combined Deficiency of β-Hexosaminidase A and Neuraminidase 3. *Front. Mol. Biosci.* **2022**, *9*, 831402.

Carter, H. E.; Haines, W. J. Biochemistry of the Sphingolipides; Preparation of Sphingolipides from Beef Brain and Spinal Cord. *J. Biol. Chem.* **1947**, *169* (1), 77–82.

Cesani, M.; Lorioli, L.; Grossi, S.; Amico, G.; Fumagalli, F.; Spiga, I.; Filocamo, M.; Biffi, A. Mutation Update of ARSA and PSAP Genes Causing Metachromatic Leukodystrophy. *Hum. Mutat.* **2016**, *37* (1), 16–27.

Chen, Y.; Qin, C.; Huang, J.; Tang, X.; Liu, C.; Huang, K.; Xu, J.; Guo, G.; Tong, A.; Zhou, L. The Role of Astrocytes in Oxidative Stress of Central Nervous System: A Mixed Blessing. *Cell Prolif.* **2020**, *53* (3), e12781.

Chiba, Y.; Akeboshi, H. Glycan Engineering and Production of "Humanized" Glycoprotein in Yeast Cells. *Biol. Pharm. Bull.* **2009**, *32* (5), 786–795.

Clark, I. A.; Vissel, B. Therapeutic Implications of How TNF Links Apolipoprotein E, Phosphorylated Tau, α-Synuclein, Amyloid-β and Insulin Resistance in Neurodegenerative Diseases. *Br. J. Pharmacol.* **2018**, *175* (20), 3859–3875.

Clarke, J.; Kayatekin, C.; Viel, C.; Shihabuddin, L.; Sardi, S. P. Murine Models of Lysosomal Storage Diseases Exhibit Differences in Brain Protein Aggregation and Neuroinflammation. *Biomedicines* **2021**, *9* (5), 446.

Coet, T.; Suzuki, K.; Popko, B. New Perspectives on the Function of Myelin Galactolipids. *Trends Neurosci.* **1998**, *21* (3), 126–130.

Connock, M.; Burls, A.; Frew, E.; Fry-Smith, A.; Juarez-Garcia, A.; McCabe, C.; Wailoo, A.; Abrams, K.; Cooper, N.; Sutton, A.; O'Hagan, A.; Moore, D. The Clinical Effectiveness and Cost-Effectiveness of Enzyme Replacement Therapy for Gaucher's Disease: A Systematic Review. *Health Technol. Assess.* **2006**, *10* (24), 1–113.

Coutinho, M. F.; Lacerda, L.; Alves, S. Glycosaminoglycan Storage Disorders: A Review. *Biochem. Res. Int.* **2012**, *2012*, 1–16.

D'Azzo, A.; Machado, E.; Annunziata, I. Pathogenesis, Emerging Therapeutic Targets and Treatment in Sialidosis. *Expert Opin. Orphan Drugs* **2015**, *3* (5), 491–504.

Demir, S. A.; Timur, Z. K.; Ateş, N.; Martínez, L. A.; Seyrantepe, V. GM2 Ganglioside Accumulation Causes Neuroinflammation and Behavioral Alterations in a Mouse Model of Early Onset Tay-Sachs Disease. *J. Neuroinflammation* **2020**, *17* (1), 277.

Ding, Z.-B.; Song, L.-J.; Wang, Q.; Kumar, G.; Yan, Y.-Q.; Ma, C.-G. Astrocytes: A Double-Edged Sword in Neurodegenerative Diseases. *Neural Regen. Res.* **2021**, *16* (9), 1702–1708.

Eng, C. M.; Guffon, N.; Wilcox, W. R.; Germain, D. P.; Lee, P.; Waldek, S.; Caplan, L.; Linthorst, G. E.; Desnick, R. J. Safety and Efficacy of Recombinant Human α-Galactosidase A Replacement Therapy in Fabry's Disease. *N. Engl. J. Med.* **2001**, *345* (1), 9–16.

Fan, J.-Q.; Ishii, S.; Asano, N.; Suzuki, Y. Accelerated Transport and Maturation of Lysosomal α–Galactosidase A in Fabry Lymphoblasts by an Enzyme Inhibitor. *Nat. Med.* **1999**, *5* (1), 112–115.

Farfel-Becker, T.; Vitner, E. B.; Kelly, S. L.; Bame, J. R.; Duan, J.; Shinder, V.; Merrill, A. H.; Dobrenis, K.; Futerman, A. H. Neuronal Accumulation of Glucosylceramide in a Mouse Model of Neuronopathic Gaucher Disease Leads to Neurodegeneration. *Hum. Mol. Genet.* **2014**, *23* (4), 843–854.

Fernández-Pereira, C.; San Millán-Tejado, B.; Gallardo-Gómez, M.; Pérez-Márquez, T.; Alves-Villar, M.; Melcón-Crespo, C.; Fernández-Martín, J.; Ortolano, S. Therapeutic Approaches in Lysosomal Storage Diseases. *Biomolecules* **2021**, *11* (12), 1775.

Ficicioglu, C. Review of Miglustat for Clinical Management in Gaucher Disease Type 1. *Ther. Clin. Risk Manag.* **2008**, *4*, 425–431.

Ficko-Blean, E.; Stubbs, K. A.; Nemirovsky, O.; Vocadlo, D. J.; Boraston, A. B. Structural and Mechanistic Insight into the Basis of Mucopolysaccharidosis IIIB. *Proc. Natl. Acad. Sci. U.S.A.* **2008**, *105* (18), 6560–6565.

Filocamo, M.; Morrone, A. Lysosomal Storage Disorders: Molecular Basis and Laboratory Testing. *Hum. Genomics* **2011**, *5* (3), 156.

Flotte, T. R.; Cataltepe, O.; Puri, A.; Batista, A. R.; Moser, R.; McKenna-Yasek, D.; Douthwright, C.; Gernoux, G.; Blackwood, M.; Mueller, C.; Tai, P. W. L.; Jiang, X.; Bateman, S.; Spanakis, S. G.; Parzych, J.; Keeler, A. M.; Abayazeed, A.; Rohatgi, S.; Gibson, L.; Finberg, R.; Barton, B. A.; Vardar, Z.; Shazeeb, M. S.; Gounis, M.; Tifft, C. J.; Eichler, F. S.; Brown, R. H.; Martin, D. R.; Gray-Edwards, H. L.; Sena-Esteves, M. AAV Gene Therapy for Tay-Sachs Disease. *Nat. Med.* **2022**, *28* (2), 251–259.

Fratantoni, J. C.; Hall, C. W.; Neufeld, E. F. Hurler and Hunter Syndromes: Mutual Correction of the Defect in Cultured Fibroblasts. *Science* **1968**, *162* (3853), 570–572.

Futerman, A. H.; van Meer, G. The Cell Biology of Lysosomal Storage Disorders. *Nat. Rev. Mol. Cell Biol.* **2004**, *5* (7), 554–565.

Guidotti, J. E.; Mignon, A.; Haase, G.; Caillaud, C.; McDonell, N.; Kahn, A.; Poenaru, L. Adenoviral Gene Therapy of the Tay-Sachs Disease in Hexosaminidase A-Deficient Knock-Out Mice. *Hum. Mol. Genet.* **1999**, *8* (5), 831–838.

Gutierrez, E. G.; Banks, W. A.; Kastin, A. J. Murine Tumor Necrosis Factor Alpha Is Transported from Blood to Brain in the Mouse. *J. Neuroimmunol.* **1993**, *47* (2), 169–176.

Ha, C. I.; DeArmey, S.; Cope, H.; Rairikar, M.; Kishnani, P. S. Treatment of Profound Thrombocytopenia in a Patient with Gaucher Disease Type 1: Is There a Role for Substrate Reduction Therapy? *Mol. Genet. Metab. Rep.* **2017**, *12*, 82–84.

Hammacher, A.; Ward, L. D.; Simpson, R. J.; Weinstock, J.; Treutlein, H.; Yasukawa, K. Structure-Function Analysis of Human IL-6: Identification of Two Distinct Regions That Are Important for Receptor Binding. *Protein Sci.* **1994**, *3* (12), 2280–2293.

Hatano, T.; Kano, O.; Sengoku, R.; Yanagisawa, N.; Nagayama, H. Impact of Istradefylline on Levodopa Dose Escalation in Parkinson's Disease: Results of the ISTRA ADJUST PD Randomized, Controlled Study (P13-11.015). *Neurology* **2023**, *100*.

Hocquemiller, M.; Hemsley, K. M.; Douglass, M. L.; Tamang, S. J.; Neumann, D.; King, B. M.; Beard, H.; Trim, P. J.; Winner, L. K.; Lau, A. A.; Snel, M. F.; Gomila, C.; Ausseil, J.; Mei, X.; Giersch, L.; Plavsic, M.; Laufer, R. AAVrh10 Vector Corrects Disease Pathology in MPS IIIA Mice and Achieves Widespread Distribution of SGSH in Large Animal Brains. *Mol. Ther. Methods Clin. Dev.* **2020**, *17*, 174–187.

Hocquemiller, M.; Giersch, L.; Mei, X.; Gross, A. L.; Randle, A. N.; Gray-Edwards, H. L.; Hudson, J. A.; Todeasa, S.; Stoica, L.; Martin, D. R.; Sena-Esteves, M.; Aiach, K.; Laufer, R. AAVrh10 Vector Corrects Pathology in Animal Models of GM1 Gangliosidosis and Achieves Widespread Distribution in the CNS of Nonhuman Primates. *Mol. Ther. Methods Clin. Dev.* **2022**, *27*, 281–292.

Homs, J.; Pagès, G.; Ariza, L.; Casas, C.; Chillón, M.; Navarro, X.; Bosch, A. Intrathecal Administration of IGF-I by AAVrh10 Improves Sensory and Motor Deficits in a Mouse Model of Diabetic Neuropathy. *Mol. Ther. Methods Clin. Dev.* **2014**, *1*, 7.

Hoshino, Y.; Nishide, K.; Nagoshi, N.; Shibata, S.; Moritoki, N.; Kojima, K.; Tsuji, O.; Matsumoto, M.; Kohyama, J.; Nakamura, M.; Okano, H. The Adeno-Associated Virus Rh10 Vector Is an Effective Gene Transfer System for Chronic Spinal Cord Injury. *Sci. Rep.* **2019**, *9* (1), 9844.

Hu, H.; Mosca, R.; Gomero, E.; van de Vlekkert, D.; Campos, Y.; Fremuth, L. E.; Brown, S. A.; Weesner, J. A.; Annunziata, I.; d'Azzo, A. AAV-Mediated Gene Therapy for Galactosialidosis: A Long-Term Safety and Efficacy Study. *Mol. Ther. Methods Clin. Dev.* **2021**, *23*, 644–658.

Hughes, D. A.; Patel, N.; Kinch, R.; Dronfield, L.; Short, G.; Sheridan, R.; Kia, A.; Jeyakumar, J.; Corbau, R.; Nathwani, A. First-in-Human Study of a Liver-Directed AAV Gene Therapy (FLT190) in Fabry Disease. *Mol. Genet. Metab.* **2020**, *129* (2), S77–S78.

Iacobazzi, D.; Convertini, P.; Todisco, S.; Santarsiero, A.; Iacobazzi, V.; Infantino, V. New Insights into NF-KB Signaling in Innate Immunity: Focus on Immunometabolic Crosstalks. *Biology (Basel)* **2023**, *12* (6), 776.

Iijima, M.; Orimo, S.; Terashi, H.; Suzuki, M.; Hayashi, A.; Shimura, H.; Mitoma, H.; Kitagawa, K.; Okuma, Y. Efficacy of Istradefylline for Gait Disorders with Freezing of Gait in Parkinson's Disease: A Single-Arm, Open-Label, Prospective, Multicenter Study. *Expert Opin. Pharmacother.* **2019**, *20* (11), 1405–1411.

Inci, O. K.; Basırlı, H.; Can, M.; Yanbul, S.; Seyrantepe, V. Gangliosides as Therapeutic Targets for Neurodegenerative Diseases. *J. Lipids* **2024**, *2024*, 1–10.

Issa, S. S.; Shaimardanova, A. A.; Solovyeva, V. V.; Rizvanov, A. A. Various AAV Serotypes and Their Applications in Gene Therapy: An Overview. *Cells* **2023**, *12* (5), 785.

Jakóbkiewicz-Banecka, J.; Węgrzyn, A.; Węgrzyn, G. Substrate Deprivation Therapy: A New Hope for Patients Suffering from Neuronopathic Forms of Inherited Lysosomal Storage Diseases. *J. Appl. Genet.* **2007**, *48* (4), 383–388.

Jarnes Utz, J. R.; Kim, S.; King, K.; Ziegler, R.; Schema, L.; Redtree, E. S.; Whitley, C. B. Infantile Gangliosidoses: Mapping a Timeline of Clinical Changes. *Mol. Genet. Metab.* **2017**, *121* (2), 170–179.

Jeyakumar, M. Central Nervous System Inflammation Is a Hallmark of Pathogenesis in Mouse Models of GM1 and GM2 Gangliosidosis. *Brain* **2003**, *126* (4), 974–987.

Kato, S.; Yabe, H.; Takakura, H.; Mugishima, H.; Ishige, M.; Tanaka, A.; Kato, K.; Yoshida, N.; Adachi, S.; Sakai, N.; Hashii, Y.; Ohashi, T.; Sasahara, Y.; Suzuki, Y.; Tabuchi, K. Hematopoietic Stem Cell Transplantation for Inborn Errors of Metabolism: A Report from the Research Committee on Transplantation for Inborn Errors of Metabolism of the Japanese Ministry of Health, Labour and Welfare and the Working Group of the Japan Society for Hematopoietic Cell Transplantation. *Pediatr. Transplant.* **2016**, *20* (2), 203–214.

Khodadadei, F.; Arshad, R.; Morales, D. M.; Gluski, J.; Marupudi, N. I.; McAllister, J. P.; Limbrick, D. D.; Harris, C. A. The Effect of A1 and A2 Reactive Astrocyte Expression on Hydrocephalus Shunt Failure. *Fluids Barriers CNS* **2022**, *19* (1), 78.

Kido, J.; Sugawara, K.; Nakamura, K. Gene Therapy for Lysosomal Storage Diseases: Current Clinical Trial Prospects. *Front. Genet.* **2023**, *14*.

Klinge, L.; Straub, V.; Neudorf, U.; Voit, T. Enzyme Replacement Therapy in Classical Infantile Pompe Disease: Results of a Ten-Month Follow-Up Study. *Neuropediatrics* **2005**, *36* (1), 6–11.

Kolter, T. Ganglioside Biochemistry. *ISRN Biochem.* **2012**, *2012*, 1–36.

Kurokawa, Y.; Osaka, H.; Kouga, T.; Jimbo, E.; Muramatsu, K.; Nakamura, S.; Takayanagi, Y.; Onaka, T.; Muramatsu, S.; Yamagata, T. Gene Therapy in a Mouse Model of Niemann–Pick Disease Type C1. *Hum. Gene Ther.* **2021**, *32* (11–12), 589–598.

Lawrence, T. The Nuclear Factor NF-κB Pathway in Inflammation. *Cold Spring Harb. Perspect. Biol.* **2009**, *1* (6), a001651.

Lawson, C.; Martin, D. Animal Models of GM2 Gangliosidosis: Utility and Limitations. *Appl. Clin. Genet.* **2016**, *9*, 111–120.

Lebkowski, J. S.; McNally, M. M.; Okarma, T. B.; Lerch, L. B. Adeno-Associated Virus: A Vector System for Efficient Introduction and Integration of DNA into a Variety of Mammalian Cell Types. *Mol. Cell. Biol.* **1988**, *8* (10), 3988–3996.

Lee, J.; Kim, C.; Park, J.; Song, M.; Kim, Y. Effect of Treadmill Exercise on Spatial Navigation Impairment Associated with Cerebellar Purkinje Cell Loss Following Chronic Cerebral Hypoperfusion. *Mol. Med. Rep.* **2018**, *17* (6), 8121–8128.

Li, C.; Samulski, R. J. Engineering Adeno-Associated Virus Vectors for Gene Therapy. *Nat. Rev. Genet.* **2020**, *21* (4), 255–272.

Liu, B.; Hong, J.-S. Role of Microglia in Inflammation-Mediated Neurodegenerative Diseases: Mechanisms and Strategies for Therapeutic Intervention. *J. Pharmacol. Exp. Ther.* **2003**, *304* (1), 1–7.

Liu, T.; Zhang, L.; Joo, D.; Sun, S.-C. NF-KB Signaling in Inflammation. *Signal Transduct. Target Ther.* **2017**, *2* (1), 17023.

Lopez-Castejon, G.; Brough, D. Understanding the Mechanism of IL-1β Secretion. *Cytokine Growth Factor Rev.* **2011**, *22* (4), 189–195.

Lyman, M.; Lloyd, D. G.; Ji, X.; Vizcaychipi, M. P.; Ma, D. Neuroinflammation: The Role and Consequences. *Neurosci. Res.* **2014**, *79*, 1–12.

Maegawa, G. H. B.; Tropak, M.; Buttner, J.; Stockley, T.; Kok, F.; Clarke, J. T. R.; Mahuran, D. J. Pyrimethamine as a Potential Pharmacological Chaperone for Late-Onset Forms of GM2 Gangliosidosis. *J. Biol. Chem.* **2007**, *282* (12), 9150–9161.

Maheshri, N.; Koerber, J. T.; Kaspar, B. K.; Schaffer, D. V. Directed Evolution of Adeno-Associated Virus Yields Enhanced Gene Delivery Vectors. *Nat. Biotechnol.* **2006**, *24* (2), 198–204.

Malhotra, R. Membrane Glycolipids: Functional Heterogeneity: A Review. *Biochemistry & Analytical Biochemistry* **2012**, *1* (2).

Matsuda, J.; Suzuki, O.; Oshima, A.; Yamamoto, Y.; Noguchi, A.; Takimoto, K.; Itoh, M.; Matsuzaki, Y.; Yasuda, Y.; Ogawa, S.; Sakata, Y.; Nanba, E.; Higaki, K.; Ogawa, Y.; Tominaga, L.; Ohno, K.; Iwasaki, H.; Watanabe, H.; Brady, R. O.; Suzuki, Y. Chemical Chaperone Therapy for Brain Pathology in GM1-Gangliosidosis. *Proc. Natl. Acad. Sci. U.S.A.* **2003**, *100* (26), 15912–15917.

Matsuoka, K.; Tamura, T.; Tsuji, D.; Dohzono, Y.; Kitakaze, K.; Ohno, K.; Saito, S.; Sakuraba, H.; Itoh, K. Therapeutic Potential of Intracerebroventricular Replacement of Modified Human β-Hexosaminidase B for GM2 Gangliosidosis. *Mol. Ther.* **2011**, *19* (6), 1017–1024.

Miyagi, T.; Yamaguchi, K. Mammalian Sialidases: Physiological and Pathological Roles in Cellular Functions. *Glycobiology* **2012**, *22* (7), 880–896.

Mokhtariye, A.; Hagh-Nazari, L.; Varasteh, A.-R.; Keyfi, F. Diagnostic Methods for Lysosomal Storage Disease. *Rep. Biochem. Mol. Biol.* **2019**, *7* (2), 119–128.

Muenzer, J.; Lamsa, J.; Garcia, A.; Dacosta, J.; Garcia, J.; Treco, D. Enzyme Replacement Therapy in Mucopolysaccharidosis Type II (Hunter Syndrome): A Preliminary Report. *Acta Paediatr.* **2002**, *91* (s439), 98–99.

Muenzer, J.; Wraith, J. E.; Clarke, L. A. Mucopolysaccharidosis I: Management and Treatment Guidelines. *Pediatrics* **2009**, *123* (1), 19–29.

Müller, T. The Role of Istradefylline in the Parkinson's Disease Armamentarium. *Expert Opin. Pharmacother.* **2023**, *24* (7), 863–871.

Myerowitz, R. Molecular Pathophysiology in Tay-Sachs and Sandhoff Diseases as Revealed by Gene Expression Profiling. *Hum. Mol. Genet.* **2002**, *11* (11), 1343–1351.

Nathwani, A. C.; Gray, J. T.; Ng, C. Y. C.; Zhou, J.; Spence, Y.; Waddington, S. N.; Tuddenham, E. G. D.; Kemball-Cook, G.; McIntosh, J.; Boon-Spijker, M.; Mertens, K.; Davidoff, A. M. Self-Complementary Adeno-Associated Virus Vectors Containing a Novel Liver-Specific Human Factor IX Expression Cassette Enable Highly Efficient Transduction of Murine and Nonhuman Primate Liver. *Blood* **2006**, *107* (7), 2653–2661.

Nestrasil, I.; Ahmed, A.; Utz, J. M.; Rudser, K.; Whitley, C. B.; Jarnes-Utz, J. R. Distinct Progression Patterns of Brain Disease in Infantile and Juvenile Gangliosidoses: Volumetric Quantitative MRI Study. *Mol. Genet. Metab.* **2018**, *123* (2), 97–104.

Ogawa, Y.; Furusawa, E.; Saitoh, T.; Sugimoto, H.; Omori, T.; Shimizu, S.; Kondo, H.; Yamazaki, M.; Sakuraba, H.; Oishi, K. Inhibition of Astrocytic Adenosine Receptor A2A Attenuates Microglial Activation in a Mouse Model of Sandhoff Disease. *Neurobiol. Dis.* **2018**, *118*, 142–154.

Okumiya, T.; Kroos, M. A.; Van Vliet, L.; Takeuchi, H.; Van der Ploeg, A. T.; Reuser, A. J. J. Chemical Chaperones Improve Transport and Enhance Stability of Mutant α-Glucosidases in Glycogen Storage Disease Type II. *Mol. Genet. Metab.* **2007**, *90* (1), 49–57.

Olsen, A. S. B.; Færgeman, N. J. Sphingolipids: Membrane Microdomains in Brain Development, Function and Neurological Diseases. *Open Biol.* **2017**, *7* (5), 170069.

Onyenwoke, R. U.; Brenman, J. E. Lysosomal Storage Diseases-Regulating Neurodegeneration. *J. Exp. Neurosci.* **2015**, *9* (s2).

Osmon, K. J. L.; Woodley, E.; Thompson, P.; Ong, K.; Karumuthil-Melethil, S.; Keimel, J. G.; Mark, B. L.; Mahuran, D.; Gray, S. J.; Walia, J. S. Systemic Gene Transfer of a Hexosaminidase Variant Using an ScAAV9.47 Vector Corrects GM2 Gangliosidosis in Sandhoff Mice. *Hum. Gene Ther.* **2016**, *27* (7), 497–508.

Palmano, K.; Rowan, A.; Guillermo, R.; Guan, J.; McJarrow, P. The Role of Gangliosides in Neurodevelopment. *Nutrients* **2015**, *7* (5), 3891–3913.

Pandey, M. K.; Burrow, T. A.; Rani, R.; Martin, L. J.; Witte, D.; Setchell, K. D.; McKay, M. A.; Magnusen, A. F.; Zhang, W.; Liou, B.; Köhl, J.; Grabowski, G. A. Complement Drives Glucosylceramide Accumulation and Tissue Inflammation in Gaucher Disease. *Nature* **2017**, *543* (7643), 108–112.

Pandey, M. K. Exploring Pro-Inflammatory Immunological Mediators: Unraveling the Mechanisms of Neuroinflammation in Lysosomal Storage Diseases. *Biomedicines* **2023**, *11* (4), 1067.

Parenti, G. Treating Lysosomal Storage Diseases with Pharmacological Chaperones: From Concept to Clinics. *EMBO Mol. Med.* **2009**, *1* (5), 268–279.

Park, S. H.; Eber, M. R.; Tsuzuki, S.; Booker, M. E.; Sunil, A. G.; Widner, D. B.; Parker, R. A.; Peters, C. M.; Shiozawa, Y. Adeno-Associated Virus Serotype Rh10 Is a Useful Gene Transfer Vector for Sensory Nerves That Innervate Bone in Immunodeficient Mice. *Sci. Rep.* **2017**, *7* (1), 17428.

Parks, W. P.; Boucher, D. W.; Melnick, J. L.; Taber, L. H.; Yow, M. D. Seroepidemiological and Ecological Studies of the Adenovirus-Associated Satellite Viruses. *Infect. Immun.* **1970**, *2* (6), 716–722.

Patterson, M. C.; Vecchio, D.; Prady, H.; Abel, L.; Wraith, J. E. Miglustat for Treatment of Niemann-Pick C Disease: A Randomised Controlled Study. *Lancet Neurol.* **2007**, *6* (9), 765–772.

Peferoen, L.; Kipp, M.; van der Valk, P.; van Noort, J. M.; Amor, S. Oligodendrocyte-Microglia Cross-Talk in the Central Nervous System. *Immunology* **2014**, *141* (3), 302–313.

Phaneuf, D.; Wakamatsu, N.; Huang, J.-Q.; Borowski, A.; Peterson, A. C.; Fortunato, S. R.; Ritter, G.; Igdoura, S. A.; Morales, C. R.; Benoit, G.; Akerman, B. R.; Leclerc, D.; Hanai, N.; Marth, J. D.; Trasler, J. M.; Gravel, R. A. Dramatically Different Phenotypes in Mouse Models of Human Tay-Sachs and Sandhoff Diseases. *Hum. Mol. Genet.* **1996**, *5* (1), 1–14.

Piguet, F.; Sondhi, D.; Piraud, M.; Fouquet, F.; Hackett, N. R.; Ahouansou, O.; Vanier, M.-T.; Bieche, I.; Aubourg, P.; Crystal, R. G.; Cartier, N.; Sevin, C. Correction of Brain Oligodendrocytes by AAVrh.10 Intracerebral Gene Therapy in Metachromatic Leukodystrophy Mice. *Hum. Gene Ther.* **2012**, *23* (8), 903–914.

Platt, F. M.; Neises, G. R.; Reinkensmeier, G.; Townsend, M. J.; Perry, V. H.; Proia, R. L.; Winchester, B.; Dwek, R. A.; Butters, T. D. Prevention of Lysosomal Storage in Tay-Sachs Mice Treated with N-Butyldeoxynojirimycin. *Science* **1997**, *276* (5311), 428–431.

Platt, F. M.; d'Azzo, A.; Davidson, B. L.; Neufeld, E. F.; Tifft, C. J. Lysosomal Storage Diseases. *Nat. Rev. Dis. Primers* **2018**, *4* (1), 27.

Rafi, M. A.; Rao, H. Z.; Luzi, P.; Curtis, M. T.; Wenger, D. A. Extended Normal Life After AAVrh10-Mediated Gene Therapy in the Mouse Model of Krabbe Disease. *Mol. Ther.* **2012**, *20* (11), 2031–2042.

Ramesh, G.; MacLean, A. G.; Philipp, M. T. Cytokines and Chemokines at the Crossroads of Neuroinflammation, Neurodegeneration, and Neuropathic Pain. *Mediators Inflamm.* **2013**, *2013*, 1–20.

Ransohoff, R. M.; Schafer, D.; Vincent, A.; Blachère, N. E.; Bar-Or, A. Neuroinflammation: Ways in Which the Immune System Affects the Brain. *Neurotherapeutics* **2015**, *12* (4), 896–909.

Rauf, A.; Badoni, H.; Abu-Izneid, T.; Olatunde, A.; Rahman, Md. M.; Painuli, S.; Semwal, P.; Wilairatana, P.; Mubarak, M. S. Neuroinflammatory Markers: Key Indicators in the Pathology of Neurodegenerative Diseases. *Molecules* **2022**, *27* (10), 3194.

Ribera, A.; Haurigot, V.; Garcia, M.; Marcó, S.; Motas, S.; Villacampa, P.; Maggioni, L.; León, X.; Molas, M.; Sánchez, V.; Muñoz, S.; Leborgne, C.; Moll, X.; Pumarola, M.; Mingozzi, F.; Ruberte, J.; Añor, S.; Bosch, F. Biochemical, Histological and Functional Correction of Mucopolysaccharidosis Type IIIB by Intra-Cerebrospinal Fluid Gene Therapy. *Hum. Mol. Genet.* **2015**, *24* (7), 2078–2095.

Roca, C.; Motas, S.; Marcó, S.; Ribera, A.; Sánchez, V.; Sánchez, X.; Bertolin, J.; León, X.; Pérez, J.; Garcia, M.; Villacampa, P.; Ruberte, J.; Pujol, A.; Haurigot, V.; Bosch, F. Disease Correction by AAV-Mediated Gene Therapy in a New Mouse Model of Mucopolysaccharidosis Type IIID. *Hum. Mol. Genet.* **2017**, *26* (8), 1535–1551.

Sandhoff, K.; Christomanou, H. Biochemistry and Genetics of Gangliosidoses. *Hum. Genet.* **1979**, *50* (2), 107–143.

Sandhoff, K.; Kolter, T. Processing of Sphingolipid Activator Proteins and the Topology of Lysosomal Digestion. *Acta Biochim. Pol.* **1998**, *45* (2), 373–384.

Sandhoff, R.; Hepbildikler, S. T.; Jennemann, R.; Geyer, R.; Gieselmann, V.; Proia, R. L.; Wiegandt, H.; Gröne, H.-J. Kidney Sulfatides in Mouse Models of Inherited Glycosphingolipid Disorders. *J. Biol. Chem.* **2002**, *277* (23), 20386–20398.

Sandhoff, K.; Harzer, K. Gangliosides and Gangliosidoses: Principles of Molecular and Metabolic Pathogenesis. *J. Neurosci.* **2013**, *33* (25), 10195–10208.
Sandhoff, K. Neuronal Sphingolipidoses: Membrane Lipids and Sphingolipid Activator Proteins Regulate Lysosomal Sphingolipid Catabolism. *Biochimie* **2016**, *130*, 146–151.
Sango, K.; Yamanaka, S.; Hoffmann, A.; Okuda, Y.; Grinberg, A.; Westphal, H.; McDonald, M. P.; Crawley, J. N.; Sandhoff, K.; Suzuki, K.; Proia, R. L. Mouse Models of Tay–Sachs and Sandhoff Diseases Differ in Neurologic Phenotype and Ganglioside Metabolism. *Nat. Genet.* **1995**, *11* (2), 170–176.
Sawamoto, K.; Karumuthil-Melethil, S.; Khan, S.; Stapleton, M.; Bruder, J. T.; Danos, O.; Tomatsu, S. Liver-Targeted AAV8 Gene Therapy Ameliorates Skeletal and Cardiovascular Pathology in a Mucopolysaccharidosis IVA Murine Model. *Mol. Ther. Methods Clin. Dev.* **2020**, *18*, 50–61.
Sengul, T.; Can, M.; Ateş, N.; Seyrantepe, V. Autophagic Flux Is Impaired in the Brain Tissue of Tay-Sachs Disease Mouse Model. *PLoS One* **2023**, *18* (3), e0280650.
Seyrantepe, V.; Demir, S. A.; Timur, Z. K.; Von Gerichten, J.; Marsching, C.; Erdemli, E.; Oztas, E.; Takahashi, K.; Yamaguchi, K.; Ates, N.; Dönmez Demir, B.; Dalkara, T.; Erich, K.; Hopf, C.; Sandhoff, R.; Miyagi, T. Murine Sialidase Neu3 Facilitates GM2 Degradation and Bypass in Mouse Model of Tay-Sachs Disease. *Exp. Neurol.* **2018**, *299*, 26–41.
Solovyeva, V. V.; Shaimardanova, A. A.; Chulpanova, D. S.; Kitaeva, K. V.; Chakrabarti, L.; Rizvanov, A. A. New Approaches to Tay-Sachs Disease Therapy. *Front. Physiol.* **2018**, *9*.
Sondhi, D.; Hackett, N. R.; Peterson, D. A.; Stratton, J.; Baad, M.; Travis, K. M.; Wilson, J. M.; Crystal, R. G. Enhanced Survival of the LINCL Mouse Following CLN2 Gene Transfer Using the Rh.10 Rhesus Macaque-Derived Adeno-Associated Virus Vector. *Mol. Ther.* **2007**, *15* (3), 481–491.
Sorrentino, N. C.; D'Orsi, L.; Sambri, I.; Nusco, E.; Monaco, C.; Spampanato, C.; Polishchuk, E.; Saccone, P.; De Leonibus, E.; Ballabio, A.; Fraldi, A. A Highly Secreted Sulphamidase Engineered to Cross the Blood-Brain Barrier Corrects Brain Lesions of Mice with Mucopolysaccharidoses Type IIIA. *EMBO Mol. Med.* **2013**, *5* (5), 675–690.
Stirnemann, J.; Belmatoug, N.; Camou, F.; Serratrice, C.; Froissart, R.; Caillaud, C.; Levade, T.; Astudillo, L.; Serratrice, J.; Brassier, A.; Rose, C.; Billette de Villemeur, T.; Berger, M. A Review of Gaucher Disease Pathophysiology, Clinical Presentation and Treatments. *Int. J. Mol. Sci.* **2017**, *18* (2), 441.
Sun, A. Lysosomal Storage Disease Overview. *Ann. Transl. Med.* **2018**, *6* (24), 476.
Sun, Y.; Koyama, Y.; Shimada, S. Inflammation From Peripheral Organs to the Brain: How Does Systemic Inflammation Cause Neuroinflammation? *Front. Aging Neurosci.* **2022**, *14*, 903455.
Takeuchi, O.; Akira, S. Pattern Recognition Receptors and Inflammation. *Cell* **2010**, *140* (6), 805–820.
Tan, E. Y.; Boelens, J. J.; Jones, S. A.; Wynn, R. F. Hematopoietic Stem Cell Transplantation in Inborn Errors of Metabolism. *Front. Pediatr.* **2019**, *7*, 433.
Taniike, M.; Yamanaka, S.; Proia, R. L.; Langaman, C.; Bone-Turrentine, T.; Suzuki, K. Neuropathology of Mice with Targeted Disruption of Hexa Gene, a Model of Tay-Sachs Disease. *Acta Neuropathol.* **1995**, *89* (4), 296–304.

Tardieu, M.; Zérah, M.; Gougeon, M.-L.; Ausseil, J.; de Bournonville, S.; Husson, B.; Zafeiriou, D.; Parenti, G.; Bourget, P.; Poirier, B.; Furlan, V.; Artaud, C.; Baugnon, T.; Roujeau, T.; Crystal, R. G.; Meyer, C.; Deiva, K.; Heard, J.-M. Intracerebral Gene Therapy in Children with Mucopolysaccharidosis Type IIIB Syndrome: An Uncontrolled Phase 1/2 Clinical Trial. *Lancet Neurol.* **2017**, *16* (9), 712–720.

Thornton, P.; Pinteaux, E.; Allan, S. M.; Rothwell, N. J. Matrix Metalloproteinase-9 and Urokinase Plasminogen Activator Mediate Interleukin-1-Induced Neurotoxicity. *Mol. Cell. Neurosci.* **2008**, *37* (1), 135–142.

Tian, W.; Ye, Z.; Wang, S.; Schulz, M. A.; Van Coillie, J.; Sun, L.; Chen, Y.-H.; Narimatsu, Y.; Hansen, L.; Kristensen, C.; Mandel, U.; Bennett, E. P.; Jabbarzadeh-Tabrizi, S.; Schiffmann, R.; Shen, J.-S.; Vakhrushev, S. Y.; Clausen, H.; Yang, Z. The Glycosylation Design Space for Recombinant Lysosomal Replacement Enzymes Produced in CHO Cells. *Nat. Commun.* **2019**, *10* (1), 1785.

Tropak, M. B.; Yonekawa, S.; Karumuthil-Melethil, S.; Thompson, P.; Wakarchuk, W.; Gray, S. J.; Walia, J. S.; Mark, B. L.; Mahuran, D. Construction of a Hybrid β-Hexosaminidase Subunit Capable of Forming Stable Homodimers That Hydrolyze GM2 Ganglioside in Vivo. *Mol. Ther. Methods Clin. Dev.* **2016**, *3*, 15057.

Tsuji, D.; Akeboshi, H.; Matsuoka, K.; Yasuoka, H.; Miyasaki, E.; Kasahara, Y.; Kawashima, I.; Chiba, Y.; Jigami, Y.; Taki, T.; Sakuraba, H.; Itoh, K. Highly Phosphomannosylated Enzyme Replacement Therapy for GM2 Gangliosidosis. *Ann. Neurol.* **2011**, *69* (4), 691–701.

Uchida, S.; Tashiro, T.; Kawai-Uchida, M.; Mori, A.; Jenner, P.; Kanda, T. The Adenosine A2A-Receptor Antagonist Istradefylline Enhances the Motor Response of L-DOPA Without Worsening Dyskinesia in MPTP-Treated Common Marmosets. *J. Pharmacol. Sci.* **2014**, *124* (4), 480–485.

Valles, S. L.; Singh, S. K.; Campos-Campos, J.; Colmena, C.; Campo-Palacio, I.; Alvarez-Gamez, K.; Caballero, O.; Jorda, A. Functions of Astrocytes under Normal Conditions and after a Brain Disease. *Int. J. Mol. Sci.* **2023**, *24* (9), 8434.

Vruchte, D. te; Lloyd-Evans, E.; Veldman, R. J.; Neville, D. C. A.; Dwek, R. A.; Platt, F. M.; van Blitterswijk, W. J.; Sillence, D. J. Accumulation of Glycosphingolipids in Niemann-Pick C Disease Disrupts Endosomal Transport. *J. Biol. Chem.* **2004**, *279* (25), 26167–26175.

Wada, R.; Tifft, C. J.; Proia, R. L. Microglial Activation Precedes Acute Neurodegeneration in Sandhoff Disease and Is Suppressed by Bone Marrow Transplantation. *Proc. Natl. Acad. Sci. U. S. A.* **2000**, *97* (20), 10954–10959.

Walz, A.; Peveri, P.; Aschauer, H.; Baggiolini, M. Purification and Amino Acid Sequencing of NAF, a Novel Neutrophil-Activating Factor Produced by Monocytes. *Biochem. Biophys. Res. Commun.* **1987**, *149* (2), 755–761.

Wang, D.; Tai, P. W. L.; Gao, G. Adeno-Associated Virus Vector as a Platform for Gene Therapy Delivery. *Nat. Rev. Drug Discov.* **2019**, *18* (5), 358–378.

Wang, H.; Yang, B.; Qiu, L.; Yang, C.; Kramer, J.; Su, Q.; Guo, Y.; Brown, R. H.; Gao, G.; Xu, Z. Widespread Spinal Cord Transduction by Intrathecal Injection of rAAV Delivers Efficacious RNAi Therapy for Amyotrophic Lateral Sclerosis. *Hum. Mol. Genet.* **2014**, *23* (3), 668–681.

Wong, K.; Sidransky, E.; Verma, A.; Mixon, T.; Sandberg, G. D.; Wakefield, L. K.; Morrison, A.; Lwin, A.; Colegial, C.; Allman, J. M.; Schiffmann, R. Neuropathology Provides Clues to the Pathophysiology of Gaucher Disease. *Mol. Genet. Metab.* **2004**, *82* (3), 192–207.

Woods, A. S.; Colsch, B.; Jackson, S. N.; Post, J.; Baldwin, K.; Roux, A.; Hoffer, B.; Cox, B. M.; Hoffer, M.; Rubovitch, V.; Pick, C. G.; Schultz, J. A.; Balaban, C. Gangliosides and Ceramides Change in a Mouse Model of Blast Induced Traumatic Brain Injury. *ACS Chem. Neurosci.* **2013**, *4* (4), 594–600.

Wu, Z.; Yang, H.; Colosi, P. Effect of Genome Size on AAV Vector Packaging. *Mol. Ther.* **2010**, *18* (1), 80–86.

Xiao, G.; Harhaj, E. W.; Sun, S.-C. NF-κB-Inducing Kinase Regulates the Processing of NF-κB2 p100. *Mol. Cell* **2001**, *7* (2), 401–409.

Xiao, W.; Warrington, K. H.; Hearing, P.; Hughes, J.; Muzyczka, N. Adenovirus-Facilitated Nuclear Translocation of Adeno-Associated Virus Type 2. *J. Virol.* **2002**, *76* (22), 11505–11517.

Xu, Y.-H.; Barnes, S.; Sun, Y.; Grabowski, G. A. Multi-System Disorders of Glycosphingolipid and Ganglioside Metabolism. *J. Lipid Res.* **2010**, *51* (7), 1643–1675.

Yamanaka, S.; Johnson, M. D.; Grinberg, A.; Westphal, H.; Crawley, J. N.; Taniike, M.; Suzuki, K.; Proia, R. L. Targeted Disruption of the Hexa Gene Results in Mice with Biochemical and Pathologic Features of Tay-Sachs Disease. *Proc. Natl. Acad. Sci. U. S. A.* **1994**, *91* (21), 9975–9979.

Yao, D.; McGonigal, R.; Barrie, J. A.; Cappell, J.; Cunningham, M. E.; Meehan, G. R.; Fewou, S. N.; Edgar, J. M.; Rowan, E.; Ohmi, Y.; Furukawa, K.; Furukawa, K.; Brophy, P. J.; Willison, H. J. Neuronal Expression of GalNAc Transferase Is Sufficient to Prevent the Age-Related Neurodegenerative Phenotype of Complex Ganglioside-Deficient Mice. *J. Neurosci.* **2014**, *34* (3), 880–891.

Ysselstein, D.; Shulman, J. M.; Krainc, D. Emerging Links between Pediatric Lysosomal Storage Diseases and Adult Parkinsonism. *Mov. Disord.* **2019**, *34* (5), 614–624.

Yu, H.; Lin, L.; Zhang, Z.; Zhang, H.; Hu, H. Targeting NF-κB Pathway for the Therapy of Diseases: Mechanism and Clinical Study. *Signal Transduct. Target Ther.* **2020**, *5* (1), 209.

Yu, Z.; Sawkar, A. R.; Kelly, J. W. Pharmacologic Chaperoning as a Strategy to Treat Gaucher Disease. *FEBS J.* **2007**, *274* (19), 4944–4950.

VITA

EDUCATION

PhD. in Molecular Biology and Genetics, September 2020 – May 2025, Izmir Institute of Technology, Molecular Biology and Genetics Department, Izmir, Türkiye

MSc. in Molecular Biology and Genetics, September 2017 – July 2020, Izmir Institute of Technology, Molecular Biology and Genetics Department, Izmir, Türkiye

BSc. in Molecular Biology and Genetics, September 2013 – June 2017, Izmir Institute of Technology, Molecular Biology and Genetics Department, Izmir, Türkiye

TEACHING AND PROFESSIONAL EXPERIENCE

Research Assistant, May 2018 – Present, Izmir Institute of Technology, Molecular Biology and Genetics Department, Izmir, Türkiye

PUBLICATIONS

Inci, O. K., Basırlı, H., Can, M., Yanbul, S., & Seyrantepe, V. (2024). Gangliosides As Therapeutic Targets For Neurodegenerative Diseases. Journal Of Lipids, 2024(1), 4530255.2024

Basirli, H., Can, M., Sengul, T., & Seyrantepe, V. (2024). Lithium Treatment Rescues Dysfunctional Autophagy In The Cell Models Of Tay-Sachs Disease. Molecular Genetics And Metabolism, 141(3), 108140.2024

Sengul, T., Can, M., Ateş, N., & Seyrantepe, V. (2023). Autophagic Flux Is Impaired In The Brain Tissue Of Tay-Sachs Disease Mouse Model. Plos One, 18(3), E0280650.2023

Can, M., Sengül, T., Demir, S. A., İnci, O. K., Basırlı, H., & Seyrantepe, V. (2022). Analysis Of Brain Lipids In The Early-Onset Tay–Sachs Disease Mouse Model With The Combined Deficiency Of B-Hexosaminidase A And Neuraminidase 3. Frontiers In Molecular Biosciences, 9, 892248.

SCHOLARSHIPS

TUBITAK 1002 PROJECT (224Z077) - Tay-Sachs Fare Modelinde İntratekal AAVrh10-fare Hexa vektör Enjeksiyonunun Otofaji Yolağı Üzerindeki Etkisinin Araştırılması, Principal Investigator

TUBITAK-FRANCE BOSPHORUS PROJECT (120N552) - Therapeutic efficacy of intrathecal administration of AAVrh10-HexA vector for correction of Tay-Sachs disease in a mouse model

TUBITAK PROJECT (117Z259) - Investigation of the biological role of lysosomal Neu1 sialidase enzyme in glycosphingolipid metabolism

TUBITAK PROJECT (215Z083) - Investigation of cellular pathology in early-onset Tay-Sachs disease mice model

AWARDS

Izmir Institute of Technology, Molecular Biology and Genetics Department, BSc, Ranked 2nd (2017)

Fellowship for European Human Genetics Conference (ESHG) (2024)

Fellowship for Young Scientists's Forum (YSF) and 49th Federation of European Biochemical Societies (FEBS) Congress (2025)